Forschungszentrum Karlsruhe
in der Helmholtz-Gemeinschaft
Wissenschaftliche Berichte
FZKA 7394

Overview of Thermohydraulic Simulations for the Development of a Helium-cooled Divertor

R. Krüßmann, G. Messemer, K. Zinn

Institut für Materialforschung
Institut für Reaktorsicherheit
Programm Kernfusion

Dezember 2008

Forschungszentrum Karlsruhe
in der Helmholtz-Gemeinschaft

Wissenschaftliche Berichte

FZKA 7394

Overview of Thermohydraulic Simulations for the Development of a Helium-cooled Divertor

Regina Krüßmann
Günter Messemer
Kevin Zinn

Institut für Materialforschung

Institut für Reaktorsicherheit

Programm Kernfusion

Forschungszentrum Karlsruhe GmbH, Karlsruhe

2008

Forschungszentrum Karlsruhe GmbH
Postfach 3640, 76021 Karlsruhe

Mitglied der Hermann von Helmholtz-Gemeinschaft
Deutscher Forschungszentren (HGF)

ISSN 0947-8620

urn:nbn:de:0005-073947

REPORT for TASK of the EFDA Technology Programme

Reference:	Field: System Studies (TR) Area: DEMO Conceptual Study (TRP) Task: He-cooled Divertor Concepts FZKA 7394		
Document:	Overview of Thermohydraulic Simulations for the Development of a Helium-cooled Divertor. FZKA 7394, October 2008.		
Level of confidentiality	Free distribution ☒ Confidential ☐ Restricted distribution ☐		
Author(s):	R. Krüßmann, G. Messemer, K. Zinn Forschungszentrum Karlsruhe		
Date:	October, 2008		
Distribution list:	D. Maissionnier (Field Coordinator), IMF3, IRS, PL Fusion		
Abstract:	At the Forschungszentrum Karlsruhe, a divertor is developed for fusion reactors of the generation after ITER. The design goal is to remove heat loads of up to 10 MW/m² at least at an acceptable pressure loss. A **he**lium-cooled **m**odular divertor concept with multiple **j**et cooling (HEMJ) was suggested. The development process is accompanied by computational fluid dynamics (CFD) simulations. This summary report gives an overview of the CFD simulations and the validation of their results. Possible error sources like modelling errors or numerical errors were investigated systematically. A mesh study was conducted to obtain a mesh-independent solution. Then, the simulated results were compared with experimental ones obtained by using the helium loop HEBLO. Agreement between measured and simulated temperature results was good. In most cases, pressure loss was overestimated by about 30%. For the 1:1 mock-up, it was underestimated by 20%. This discrepancy has not been explained so far. The overall results provide confidence in the results of the numerical model and its applicability to the design of the HEMJ divertor as well as of other gas-cooled high-heat-flux components under fusion reactor operating conditions.		
Revision No: 0	Changes: 0		
	Written by:	Reviewed by:	Approved by:
	R. Krüßmann, G. Messemer, K. Zinn	P. Norajitra	

Abstract

At the Forschungszentrum Karlsruhe, a divertor is developed for fusion reactors of the generation after ITER. The design goal is to remove heat loads of up to 10 MW/m² at least at an acceptable pressure loss. A **he**lium-cooled **m**odular divertor concept with multiple **j**et cooling (HEMJ) was suggested. The development process is accompanied by computational fluid dynamics (CFD) simulations.

This summary report gives an overview of the CFD simulations and the validation of their results. Possible error sources like modelling errors or numerical errors were investigated systematically. A mesh study was conducted to obtain a mesh-independent solution. Then, the simulated results were compared with experimental ones obtained by using the helium loop HEBLO. Agreement between measured and simulated temperature results was good. In most cases, pressure loss was overestimated by about 30%. For the 1:1 mock-up, it was underestimated by 20%. This discrepancy has not been explained so far.

The overall results provide confidence in the results of the numerical model and its applicability to the design of the HEMJ divertor as well as of other gas-cooled high-heat-flux components under fusion reactor operating conditions.

Überblick über die thermohydraulischen Simulationsrechnungen zur Entwicklung eines heliumgekühlten Divertors

Zusammenfassung

Am Forschungszentrum Karlsruhe wird ein Divertor für Fusionskraftwerke der Generation nach ITER entwickelt. Ziel ist es, Wärmelasten von mindestens 10 MW/m² bei akzeptablem Druckverlust abzuführen. Ein heliumgekühltes, modulares Konzept mit Prallstrahlkühlung wird vorgeschlagen. Der Entwicklungsprozess wird von strömungsmechanischen Simulationsrechnungen begleitet.

Dieser zusammenfassende Bericht gibt einen Überblick über die Simulationsrechnungen und die Validierung der Ergebnisse. Mögliche Fehlerquellen wie z. B. Modellfehler oder numerische Fehler wurden systematisch eliminiert. Eine Netzstudie wurde durchgeführt, um vernetzungsunabhängige Ergebnisse zu erhalten. Schließlich wurden die simulierten Ergebnisse mit experimentellen aus der HEBLO–Anlage verglichen. Die Übereinstimmung, besonders bei den Temperaturwerten war gut. Der Druckverlust wird von den CFD-Programmen um ca. 30 % überschätzt, im Falle des 1:1 Modells um 20 % unterschätzt. Diese Diskrepanz konnte bisher nicht geklärt werden.

Global betrachtet zeigen die Ergebnisse die Anwendbarkeit des numerischen Models für Design und Auslegung des HEMJ Divertor-Konzepts, wie auch für andere gasgekühlte Komponenten des Fusionsreaktors.

Table of contents

1 Introduction

At the Forschungszentrum Karlsruhe, a divertor is developed for fusion reactors of the generation after ITER. The design goal is to withstand heat loads of up to 10 MW/m² at least at an acceptable pressure loss. More details about the project can be found in [1].

A **he**lium-cooled **m**odular divertor concept with multiple **j**et cooling (HEMJ) was suggested to remove the divertor heat load. To investigate the thermohydraulic performance of the design and to optimise it, simulations were run with commercial computational fluid dynamics (CFD) programs. Special attention was paid to the engineering limits, i.e. the maximum temperature of the tile and the thimble and the pressure loss. The temperatures are limited by the choice of the material (maximum temperature tile: 2500 °C, thimble 1300 °C [2]). Pumping power is limited to 10 % of the heat to be removed by the divertor.

Considerable efforts were undertaken to validate the results of the simulations. Possible error sources were identified and investigated. The objective is to optimise the simulations to obtain a tool yielding reliable results. This can only be accomplished by a “kaizen” approach, a continuous improvement in small steps [3].

In this summary report, an overview of fundamentals of flow simulation and its principles will be given first. A focus will lie on the possible error sources. Then, the HEMJ test case shall be described. Modelling and the set-up used for the simulations will be discussed in detail. A study of the meshing density will show the way to a mesh-independent solution.

In the subsequent section, numerical errors will be investigated by means of a best-practice approach [4]. Then, the simulated results will be compared with experimental ones obtained by using the helium loop HEBLO [5], [6], [7]. On this basis, a parameter study to optimise the HEMJ design was conducted [8]. The report will be completed by an overall conclusion regarding the use of commercial CFD programs in the design of a helium-cooled divertor.

2 Computational fluid dynamics (CFD)

CFD is a computational method to study the flow of fluids (liquids and gases). Problems encountered in the real world are described by physical models. Often, they contain some simplifications. The models are translated into equations to be solved by mathematical methods, implemented in a computer, and simulated. By this means, flow behaviour under various circumstances can be predicted, e.g. in a parametric study. Issues related to fluid dynamics like heat transfer, mass transfer, phase change, chemical reactions, etc. can also be investigated. The applications are highly variable: From transport (car engines, aeronautics) to chemical processing industries, energy, biology, etc., simulations are used to save time and money in development processes.

With the development of modern computers after World War II, the science of numerical mathematics also boomed. During the 60s, it became possible to solve problems by simulation, which could not be solved analytically before. During the 70s and 80s, the modern CFD solvers existing today were developed. Since then, their role especially in industrial development processes has become constantly gained importance. CFD provides insights into otherwise hidden processes and allows to predict the behaviour of the process under different boundary conditions. By this means, a high number of prototypes can be tested rapidly without spending any money for experimental investigations, which usually are more costly. Furthermore, CFD is especially favourable in cases, where experiments are dangerous (explosives, nuclear safety analyses) or impossible (geology, meteorology).

2.1 Finite-difference method, finite-element method, and finite-volume method

The governing equations for mass, momentum, and energy are partial differential equations. In the finite-difference method [9], the space where they are to be solved is divided into a finite number of grid points. At these points, the partial derivatives are approximated numerically and solved by algorithms.

In the finite–element method [9], the space is divided into a number of finite elements. For each element, a basis function is defined, weighted, and then inserted into the partial differential equation which is solved by the algorithm. This method is usually used for codes that investigate stress and strain in a material (ANSYS®, ABAQUS®).

In the finite-volume method [9], the space is divided into a number of volumes (cells). “Volume integrals in a partial differential equation that contain a divergence term are converted to surface integrals, using the divergence theorem. These terms are then evaluated as fluxes at the surfaces of each finite volume. Because the flux entering a given volume is identical to that leaving the adjacent volume, these methods are conservative. Another advantage of the finite volume method is that it is easily formulated to allow for unstructured meshes. The method is used in many computational fluid dynamics packages.” [9]

2.2 Pre-conditions for CFD and processing

- The problem is a fluid dynamics problem. It is identified and analysed, the objective of the investigation is clear. Then, it is abstracted, sometimes simplified.
- The problem can be described by a numerical model: the governing differential equations for mass, momentum, and energy conservation are known. Problems like two-phase flow, chemical reaction kinetics, etc. need additional models.
- A control space is defined, where the equations are to be solved: A geometrical model is built which can be done by CAD products (computer-aided design programs like AutoCAD®, ProEngineer®, CATIA®) or by the pre-processors that are delivered with the CFD software.

- The space is split up into a number of cells (control volumes around a grid point): meshing. The mesh does not necessarily have to have the same density in all places. To solve the equations, they are discretised in the centre of the computational cells (e.g. in a Taylor series). This means that the partial differentials are translated into a (linear) equation with coefficients that form a matrix. The algorithm in the solver will solve this matrix.
- Boundary conditions are set. These are known values of e.g. velocity, mass flow, heat load, etc. at the inlet, outlet, and on walls.
- After this pre-processing, the model is introduced into the solver. To start, each grid point is given an initial value chosen by the user. The better this “guessed” starting point is, the faster a solution is reached.
- The calculations are done and result data are generated. In each cell of the mesh the governing equations of mass, impulse, and energy are solved together with the model-related equations (for chemical reactions, for example), before the simulation moves on to the next cell.
- When the calculation has finished for all cells, one iteration step is finished. The results are compared to the solution of the previous step. If the difference between the two solutions (the maximum residual) is too large, calculation for all cells is repeated, starting from the last solution as start condition.
- When the maximum residual is smaller as 10^{-3} at least, better 10^{-4}, the simulation can be stopped. Other values, e.g. the outlet pressure or some monitoring points (e.g. temperature in one part), should be observed as well. In addition, all balances should be checked.
- Then, the results can be organised, displayed, and analysed by post-processing tools. Nowadays, most of them work with graphical user interfaces.
- Sometimes, a change in the model is necessary, if some problems occur or if more than one case of boundary conditions are to be tested. Usually, the preparation or change of the model is the most labour-intensive step. Sometimes, only a parameter is changed to simulate the model under different boundary conditions and perform a parametric study.

The accuracy of CFD generally is about 5% [10], but strongly depends on the individual problem. Comparison and code validation with experimental investigations is strongly advised, sometimes indispensable. But CFD will save time and resources. Simulations are run faster and cheaper as experiments and they reveal the complete information on the problem (not just a measurement of a thermocouple in one specific place). On the other hand, both the experiment and the numerical model only *model* the reality. Both make reliable predictions, if some standards are kept, but they can never predict anything that might happen in the real world. Some uncertainty always remains.

3 Code verification and validation

Simulations with computational fluid dynamics (CFD) programs are a powerful tool to predict the flow behaviour and heat transfer in a process. But any simulation can only be a model of reality. Therefore, it is necessary to minimise errors, with the aim of approaching the real solution as closely as possible. Only a reliable and accurate solution will provide the information needed and generate confidence in the results.

Comparison of simulations with experimental results is often difficult. Experiments described in papers often lack the necessary information or are not accurate enough. Like simulations, experiments also are only models of reality. Possible errors of experiments lie in the geometrical definition, data production procedures, dominant physics, or in calibration, data acquisition, and data treatment, etc.

Two tasks have to be fulfilled for simulations: verification and validation [11]. While code verification comprises the mathematics (solving the equations right), code validation means modelling of the physics of the problem (solving the right equations). Naturally, verification comes before validation.

Using a commercial code, verification is essentially done by the code developers. Usually, the source codes are not accessible for the users. Errors that can be controlled by the user are more on the side of physical modelling and numerical errors.

The term ‘validation’ given as it is used in the context of this report shall be defined as follows [12]:

“Validation is defined as the process of assessing the credibility of the simulation model, within its domain of applicability, by determining whether the right simulation model is developed and by estimating the degree to which this model is an accurate representation of reality from the perspective of its intended uses. “

Four main sources of errors exist for simulations [13]:

1) Inadequate modelling of physics of the flow, such as turbulence, multi-phase flow, heat transfer, and combustion.
2) The boundary conditions do not reflect the physics of the problem (inflow, outflow, heat transfer).
3) Non-physical effects, such as numerical diffusion, dispersion, and other numerical errors that result when the governing partial differential equations (PDEs) are discretised into algebraic equations in a discrete domain by finite-difference, finite-volume or finite-element methods.
4) Simplified geometry and mesh: they do not represent the real geometry adequately and allow for the PDEs to be solved while the density of the mesh is often restricted by computer or economic limits.

Numerical errors comprise:

- Spatial discretisation (mesh density): critical regions must be meshed with an adequate number of mesh cells. A study with different mesh densities is necessary to obtain a grid-independent solution.
- Time discretisation: the time step must be adequate, such that instationarities are detected or solved.
- Round-off errors of the computer: very difficult to control, because they depend on the processor used, but often, it is possible to run the simulations in the double-precision mode[1].

---

[1] We tried double precision in two examplary cases: The temperature results changed by 0.01 K, the pressure by 2 Pa of 16000 Pa. Therefore, it will not be discussed in detail in this report.

- Mathematical discretisation: partial differential equations are solved in the form of Taylor series. The number of higher-order terms involved influences the solution.
- Iteration errors: simulation is stopped before the results are reached. To avoid this, the residuals and a few monitoring points have to be observed.

The possible errors will be investigated in this report:

1) + 2) Inadequate modelling, inappropriate boundary conditions: all cases were discussed extensively with the support teams of the codes, at national and international conferences, etc. Helpful suggestions were accounted for.
3) Numerical errors will be investigated in chapter 6.
4) Simplified geometry and mesh: the geometry closely reflects the design. A mesh density study was run for both codes; results will be given in chapter 5.

4 Description of the test case for code validation

At the Forschungszentrum Karlsruhe, a concept for a helium-cooled divertor is developed [1]. The divertor is an essential part of a fusion reactor: its main purpose is to remove impurities (helium ash, particles from wall erosion) from the plasma. A clean plasma can be kept at higher temperatures. Hence, so the divertor supports the fusion reaction.

Fig. 1 shows a view into the reactor. The impurities are transported along the separatrix (one of the outermost magnetic field lines) and hit the divertor target plates. Finally, they are pumped through an opening below the dome.

The divertor is highly loaded with particles and heat; it has to be cooled extensively. The mean heat load will be around 6 MW/m², peak values of 10 – 20 MW/m² are to be expected at the strike point of the separatrix [14]. Therefore, a completely new cooling system had to be developed to remove at least 10 MW/m² at an acceptable pumping power (about 10% of the energy gained by integrating divertor cooling in the overall turbine cycle).

For this purpose, the whole divertor is split up into 48 cassettes (according to the latest DEMO design [14]) to ease maintenance and handling. The target plates are split up into a number of small hexagonal tiles made of tungsten (diameter 17 mm). Below each tile, a thimble-like cap of the tungsten alloy WL10 (W-1%La_2O_3) is placed. Inside the cap, a steel cartridge with holes is fixed. Helium as a coolant enters the cartridge, is accelerated through the holes, and impinges on the inner surface of the thimble (Fig. 2). This jet impingement cooling method is widely used in turbine cooling in aeronautics industry and was adapted to the needs of the helium-cooled divertor.

The cooling fingers will be divided into groups of 9 fingers which are cooled in parallel. In addition, they are divided again into stripe units which are cooled in series. Fig. 3 shows the assembly of a target plate.

4.1 Mechanism of heat transfer

Jet impingement cooling is widely used in industry to cool long, plane products like metal or glass sheets, or for turbine cooling. Turbulent jets leave round or slot nozzles and impinge on a flat surface at a stagnation point. Here, vertical velocity is reduced to zero, while horizontal velocity increases from zero to a maximum. Fig. 4 shows the different zones of such a jet.

An array of jets is used to distribute the coolant more homogeneously. Then, the single jets influence each other.

A correlation for the mean heat transfer coefficient htc of an array of nozzles in a triangular arrangement with a round diameter is given in [15],

$$\mathrm{htc} = \frac{\mathrm{Nu} \cdot \lambda}{\mathrm{D}} \tag*{(1),}$$

where λ is the heat conductivity of the coolant and D is the jet hole diameter.

The Nusselt number Nu can be calculated as

$$\mathrm{Nu} = \mathrm{G} \cdot \mathrm{Re}^{2/3} \cdot \mathrm{Pr}^{0.42} \tag*{(2).}$$

Pr is the Prandtl number, Re is the jet Reynolds number, and G is a geometry function. The Prandtl number is defined as:

$$\mathrm{Pr} = \frac{c_p}{\lambda} \eta \tag*{(3),}$$

the jet Reynolds number can be calculated as follows:

$$\mathrm{Re} = \frac{w D_h}{\nu}, \quad \nu = \frac{\eta}{\rho} \tag*{(4), (5).}$$

Here, c_p is the heat capacity, ν kinematic viscosity, η dynamic viscosity, and ρ the density of the coolant. D_h is the hydraulic diameter of the jet. In case of a round nozzle, it is the nozzle diameter. The averaged jet velocity w can be calculated when the jet mass flow is known:

$$w = \frac{\dot{m}_j}{A_h} \tag*{(6).}$$

A_h is the total surface area of all nozzles.

The geometry parameter G is defined as:

$$G = \frac{d^* \cdot (1 - 2.2 \cdot d^*)}{1 + 0.2(h^* - 6) \cdot d^*} \cdot \left[1 + \left(\frac{10 \cdot h^* \cdot d^*}{6}\right)^6\right]^{-0.05} \qquad (7);$$

$$f = \frac{\pi}{2 \cdot \sqrt{3}} \cdot \frac{{D_h}^2}{L_T^2}, \; d^* = \sqrt{f}, \; h^* = \frac{H}{D} \text{ (see Fig. 5)} \qquad (8), (9), (10).$$

These equations are only valid for the following ranges:

$$\begin{aligned} &0.004 \le (d^{*2} = f) \le 0.04 \\ &2 \le (h^* = H/D) \le 12 \\ &2000 \le Re \le 100000 \end{aligned} \qquad (11).$$

The following parameters might be optimised:

- diameter of the nozzles
- arrangement of the nozzles (in line or staggered)
- shape of the nozzles (round, slit, etc.)
- distance between the nozzles
- distance between the nozzles and the cooled surface
- the cooled surface is plane / concave / convex / has a surface structure
- the cooled surface is hit orthogonally / under inclination
- stationary or pulsed flow
- cross flow effects

Some of these have already been investigated in literature and in a parametric study to optimise the divertor cooling design (see chapter 10).

4.2 Material properties

All material properties can be found in Tab. 1 [16]. They were taken to be temperature-dependent.

Helium was chosen as a coolant, because it is chemically and neutronically inert. Together with the use of beryllium as a first wall material, it has a safety advantage over water and it can be operated at higher temperatures than water.

Tungsten has a high melting point, a high thermal conductivity, and good sputtering properties. On the other hand, it is very brittle. A large investigation program to develop it as a structural material and to develop other alloys with a better ductility and a better ductile-to-brittle transition temperature (DBTT) and recrystallisation temperature (RCT) is under way [17].

WL10 is doped tungsten with 1% lanthanum oxide to enhance its ductility. In the future, it will be replaced by another tungsten alloy, because it is still not ductile enough.

For the cartridge, refractory steel (i.e. ODS Eurofer) will be used. Since it is not exposed to high temperatures, no special requirements have to be fulfilled.

All problems related to materials and manufacturing are being studied within the framework of a research program [18].

4.3 Boundary conditions

The boundary conditions of the reference test case were developed in an analytical study [2] and are summarised in Tab. 2. A surface heat power of 248 MW (alpha and heating power) has to be removed from the divertor target. A power distribution between inboard and outboard targets of 1:4 is assumed, thus leading to a surface heat power of 198.4 MW for the outboard target (in a worst-case scenario, only the higher loaded outboard target plate is considered). For a 7.5° divertor cassette, the size of an outboard target plate is about 810 x 1000 mm (toroidal x poloidal), leading to an overall average surface heat load of about 5.1 MW/m² for the outboard target plates.

In addition, 78.8 MW of neutron-generated heat power have to be handled, of these 44.1 MW on the outboard target plate. In total, a mean head load of 6.2 MW/m² has to be removed without taking into account the peak heat load of the separatrix strike point.

The inlet temperature of the coolant into the target plate was fixed to 600 °C to keep the refractory materials above their ductile-to-brittle transition temperature (DBTT). The outlet temperature was set to about 700 °C. The inlet pressure of the helium was set to 100 bar. A preliminary CFD study showed that the heat can be removed with a mass flow of 6.8 g/s per finger [2].

The divertor target plate (poloidal height 1000 mm) is divided into two zones that are connected in series. Due to the 9-finger design, all finger units in three parallel rows in one zone are connected in parallel, because the total mass flow of the divertor would be too high, if all finger units were connected in parallel. One poloidal row contains 30 parallel fingers in one zone. For one outboard divertor target plate, 51 parallel rows are arranged in toroidal direction. This results in a total mass flow of 9.6 kg/s for one divertor outboard target plate.

In the worst-case scenario, the peak heat load also has to be taken into account. It was assumed that the strike point lies on the first finger of zone 2, when the helium has already reached an elevated inlet temperature. Then, a mass flow of 6.8 g/s helium at an inlet pressure of 100 bar and an inlet temperature of 634 °C was defined as the reference layout condition. The heat load for the design layout calculations was fixed to 10 MW/m² [14].

Results of a parametric study considering variable reference case boundary conditions can be found below in chapter 10.

4.4 CFD programs

Two commercial programs were used to run the thermohydraulic simulations:

- ANSYS FLUENT 6.2 and 6.3 [19] and its pre-processor for meshing, GAMBIT 2.2 and 2.3 [20]
- ANSYS CFX 10 and 11 [21], mostly with meshes generated in GAMBIT, some meshes were also generated by ANSYS ICEM 10 and 11 [22].

Both solvers form control volumes to ensure the conservation of flow quantities, but they differ in the way they integrate the flow equations and in their equation solution strategies. CFX uses finite elements to discretize the domain, FLUENT uses finite volumes. CFX solves the governing equations for motion (pressure-based coupled solver), while FLUENT offers several solution approaches (density-, segregated- and coupled pressue-based methods). [23]

The performances of the two codes were compared. In some of the chapters, it will be referred to this comparison.

4.5 Set-up of the simulations

Only the top part of the cooling finger, as shown in Fig. 6, was simulated. For symmetry reasons, only 1/6 or even 1/12 of the geometry was used. The cut surfaces were defined as symmetry walls. All external surfaces except for the plasma-facing top surface were assumed to be adiabatic (the finger will be placed in a vacuum). Radiation from the finger into the plasma was not considered, because the heat load values were taken as the net impact on the cooling finger.

The heat load was defined to be a constant surface heat flux on top of the tile. Neutronic heating was defined as a source term in all materials, assuming 17 MW/m³ [2]. All thermohydraulic boundary conditions were discussed above (chapter 4.3). At the inlet and outlet, a turbulent production rate of 5 – 10% and the hydraulic diameter were chosen as settings.

4.6 Turbulence models

4.6.1 General remarks

Flow can either be laminar (all flow paths are parallel to each other) or turbulent or in a transition state. Turbulent flow is highly instationary, three-dimensional, dissipative, and irregular. It leads to an enhanced mass and heat transport and an enhanced pressure loss.

Turbulent flow cannot be calculated analytically. It has to be modelled by turbulence models. The most popular ones are the Reynolds-averaged Navier-Stokes (RANS) equations, a statistic approach. The transport terms in the PDEs are replaced by mean values and additional turbulent terms. These reflect the additional transport of energy, impulse, and mass due to the turbulent behaviour of the flow. This leads to open systems of equations and requires the definition of additional equations for the turbulent terms (like the turbulent kinetic energy k and either the turbulent dissipation rate ε or the specific dissipation rate ω). Empirical models are used to define k and ε or ω, which contain one to three additional equations.

Numerous models exist to close the system of equations. Only the models used in this report will be mentioned below [24]. The definition equations can be found in text books on turbulence modelling:

- k- ε model: in its standard form, the k - ε model is the most popular turbulence model for practical (industrial) applications. It is robust, economically efficient, and reasonably accurate for all industrial flow problems and heat transfer simulations. Its constants have been widely tested. It is a high-Reynolds number model, i.e. it cannot be integrated to the wall. For modelling near-wall flow, dampening functions are necessary.
- RNG k- ε model: it was derived by a rigorous statistical technique (called **ren**ormalisation **g**roup theory) to overcome some of the drawbacks of the standard k-ε model. It is more accurate for rapidly strained flows and swirl flow. It includes a turbulent Prandtl number and accounts for low-Reynolds number effects (it can be integrated to the wall).
- Standard k – ω model (as implemented in FLUENT): it accounts for low-Reynolds number effects, compressibility, and shear flow spreading. It is suited for free jets and wall – bounded flows.
- Shear-stress transport (SST) model: it effectively blends the free-stream independence of the k – ε model in the far field with the robust and accurate formulation of the k – ω model in the near-wall region. This is the model preferred for use in CFX.

Implementation of each turbulence model in the different commercial codes is not necessarily the same!

Looking at the turbulence models, it is obvious that special attention has to be paid to modelling the near-wall region. Near the wall, turbulence is dampened and the velocity decreases to zero as viscous forces start to influence the flow. The velocity shows a steep gradient. Fig. 7 shows the mean velocity profile near a wall on a logarithmic scale. The dimensionless velocity U^+ is shown over the dimensionless distance to the wall y^+, the wall being at $y^+ = 0$. Near the wall, the velocity profile is a universal profile, regardless of the kind of flow in the free stream (outer region), where flow depends on the problem. Velocity U^+ and wall distance y^+ are made dimensionless with the wall shear stress τ_{wall}, the value u_τ is called “friction velocity”:

$$U^+ = \frac{U}{u_\tau}; \qquad y^+ = \frac{u_\tau y}{\nu}; \qquad u_\tau = \sqrt{\frac{\tau_{wall}}{\rho}} \qquad (12), (13), (14).$$

In the sub-layer ($y^+ < 5$) viscous forces predominate the flow. The region $5 < y^+ < 30$ is called the transition zone. For about $30 < y^+ < 350$, the logarithmic law of the wall holds.

In simulation the wall effects have to be taken into account [25]. This may be done by including empirical wall functions. Then, resolving the boundary layer is not necessary. Thus, time and CPU resources are saved, the mesh can be kept comparatively coarse. Another approach is to use the low-Reynolds number method (only applicable with turbulence models that contain an equation for ω). The boundary layer has to be resolved with a very fine mesh, CPU times and storage needs are much higher.

It depends on the turbulence model whether the viscous sublayer has to be resolved. A finer mesh near the wall together with a high-Reynolds number turbulence model and standard wall functions can cause larger errors than a coarse mesh. Generally, the whole boundary layer should contain at least 10 nodes.

Modern codes contain an automatic scaling of the wall functions, such that reliable results are obtained for the simulations independently of the grid resolution. The SST turbulence model switches automatically between the k – ε and the k - ω equation near the wall.

4.6.2 Choice of a turbulence model suited for the test case

The ANSYS CFX company investigated different turbulence models for impinging jet cooling [26]. They used a number of published experiments and simulated them with CFX 5, meshes of different densities, and different turbulence models. The experiments revealed a scatter of about 25% in the local Nusselt number. The predictions of the three turbulence models were in good agreement with the experimental data. The SST and the v2f model (which is not implemented in CFX, results were taken from [27]) fitted the data better than the k – ε model.

Gordeev also investigated turbulence models with the commercial program Star-CD® [28]. Only turbulence models with a limited turbulence production in the stagnation zone were found to predict jet impingement heat transfer correctly for a single jet. For a nozzle array and cross flow, the two-layer RNG turbulence model and the v2f turbulence model showed the best agreement with the experimental values, Fig. 8.

For the simulations in this report, the RNG k – ε model with enhanced wall treatment and the SST model were used in FLUENT and in CFX, respectively (both as suggested by the support teams).

5 Mesh generation and comparison of different meshes

Most meshes for this investigation were generated by the pre-processing program GAMBIT 2 [20], some also with ICEM 10 [22]. In both cases, the geometry usually was created in a third-party computer-aided design (CAD) program, mostly CATIA V5, then converted into the multi-purpose format stp, and exported to the meshing programs. However, both meshing programs also allow for the creation of geometry to a certain extent.

Meshes have to be generated in accordance with the needs of the solver used. For 3D simulations with heat transfer (CFX only works in three-dimensional space), most cells should be hexahedrons. If they are stretched, stretching should be in the direction of the heat transport. Sometimes, it is not possible to mesh complicated volumes only with hexahedrons. Then, tetrahedrons are used. At the interface between hexahedrons and tetrahedrons, pyramids are placed. Unfortunately, CFX is quite intolerable to pyramid elements.

The philosophies of the two meshing programs are completely different: In GAMBIT the most important volume for heat transfer is chosen and meshed first. (In the case treated here, the most sensitive part is the gas volume near the jet impingement surface. Due to its complicated geometry, all GAMBIT (FLUENT) meshes use tetrahedrons in this region.) Then, meshing continues from inside to outside. The mesh quality is measured as "equi-angle skewness" and "equi-size skewness".

The equi-angle skewness is defined as [29]

$$\max\left[\frac{\theta_{max}-\theta_e}{180-\theta_e},\frac{\theta_e-\theta_{min}}{\theta_e}\right] \qquad (15),$$

where θ_{max} is the maximum angle in a cell, θ_{min} is the smallest one, and θ_e is the angle of the equiangular cell, e.g. 60 for a triangle, 90 for a square. The equi-size skewness is defined in an analogous way. It describes the size differences in neighbouring cells. A mesh of high quality should not exceed a value of 0.9. In practice, values of 0.95 are tolerable, if the number of highly skewed cells is not too high. Furthermore, the aspect ratio (length – diameter ratio) of the cells should not be too high. Most modern codes tolerate values around 40 and even higher.

For ICEM (CFX) meshes, a block is built around the whole geometry first. Then, this block is sculpted to fit the geometry and projected on it. The sub-blocks are meshed. In the last step, the mesh is converted to an unstructured mesh and exported to CFX. In contrast to GAMBIT, workflow is from outside to inside.

ICEM allows creating also hexahedron meshes in the gas impingement volume. In contrast to GAMBIT, the quality is measured directly (instead of weighted). The angles of all cells should be higher than 20° (for tetrahedrons: 15°). Angles in pyramids naturally are very small; therefore, pyramids should not be used in a mesh. To overcome this problem, ICEM offers a different method to join mesh parts with hexahedrons and tetrahedrons (GGI interface). On the other hand, the aspect ratio is computed as a normalised value (between 0 and 1).

Transporting a FLUENT mesh to ICEM and vice versa is possible in most cases, but creates some problems as regards the quality control of the mesh and the different needs of the solvers. Transporting a GAMBIT mesh with hexcore elements proved to be impossible [7].

During this investigation, a large number of meshes were created by GAMBIT and by ICEM. Some of them will be compared in performance below, focusing on the mesh density in particular.

5.1 Comparison of different meshes created with GAMBIT and simulated with FLUENT

Tab. 3 shows the results of a meshing study: a number of different meshes was created in GAMBIT and simulated with the reference boundary conditions (i.e. a mass flow of 6.8 g/s at an inlet temperature of 634 °C and an inlet pressure of 100 bar, and a heat load of 10 MW/m² on top of the tile) in FLUENT 6. The inlet boundary condition was given as a mass flow value. 1/6 of the geometry J1a (see below, chapter 10) was meshed for this study. The total number of cells and the number of cells in the gas impingement volume increased from mesh multijet18 to multijet22 (multijet21 does not exist because of a computer failure), while mesh quality was kept almost constant. The meshing strategy always was the same, just the density was increased. Figs. 9 to 11 show the meshes for multijet18, multijet19, and multijet22 (for multijet20, no figures are available). All simulations were completely iterated using the RNG k - ε turbulence model with enhanced wall treatment and second-order discretisation.

The temperatures were assessed as the "facet maximum", the local maximum in a cell. The important design parameters, i. e. the maximum temperature of the tile and maximum temperature of the thimble, decreased with increasing number of cells for multijet 18 to multijet20 (from 1765 °C to 1678 °C for the tile, from 1220 °C to 1126 °C for the thimble). The mean heat transfer coefficient (htc) of the impingement surface increased from about 25 kW/m²K to about 32 kW/m²K, pressure loss between inlet and outlet of the finger decreased from 1.36 bar to 1.25 bar. An exception was mesh multijet22, all values of which went in the opposite direction. The percentage change between the values always became smaller.

5.2 Comparison of different meshes created with ICEM and simulated with CFX

Tab. 4 shows the results for different meshes that were created with ICEM 10 and simulated with CFX 10 under the reference boundary conditions for the same geometry J1a [30]. Figs. 12 to 14 show the meshes, in particular the most interesting region near the jet impingement surface. It should be noted that in contrast to the FLUENT meshes, only 1/12 of the geometry J1a was meshed for CFX to keep the number of cells manageable. One sixth is perfectly symmetric, while 1/12 only is mirror-symmetric. The inlet boundary condition was given to be the mean velocity.

The number of cells and their quality in the impingement jet region were not given separately, because the volumes were subdivided differently from those in GAMBIT and the whole gas volume was meshed as one. For the same reason, the htc could not be given, because the jet impingement surface was not defined separately in the geometry.

The simulations were run with 75% second-order discretisation (see chapter 6 on the best-practice study below), using the SST turbulence model and the reference boundary conditions. For the coarse and medium mesh, they were completely iterated. The fine mesh did not converge to a constant value, but tended to oscillate slightly instead. This can be attributed to transient details of the flow captured by the fine mesh. CFX needs less iteration steps than FLUENT and is faster. During the first iterations, the solver does not compute a solution for every single cell of the mesh. Instead, the mesh is partitioned and for each part a solution is computed. Then, partitioning is refined until every cell is taken into account. In this way, a first coarse solution is reached faster and the initial guess for all cells is improved.

Again, the temperatures of the tile and thimble decrease with an increasing number of cells (tile from 1788 °C to 1763 °C, thimble from 1224 °C to 1190 °C), the percentage change decreases for each refinement. Also, the pressure loss decreases from 1.31 bar to 1.304 bar.

Discussion

Two aspects of the results should be highlighted. Firstly, asymptotic temperature and pressure loss values are reached for the simulation with the finest meshes for both codes. Relative changes from the medium to the fine mesh are less than 1% (CFX), relative changes from multijet19 to multijet20 are about 3% (FLUENT). Secondly, both design parameters are reduced with further mesh refinement and higher-order discretisation. Consequently, the error in the analysis may be assumed to be on the conservative side. The increase of all parameters for multijet22 (FLUENT) probably is due to the same effects as observed in CFX for the fine mesh. Transient effects are solved by the high-mesh resolution.

Investigation was continued with the meshes of multijet19 (FLUENT) and the medium CFX mesh. Multijet19 was deemed a good compromise to save iteration time and disc space, while multijet20 took much longer to converge.

5.3 Cross comparison of different meshes with the two codes

The meshes prepared were exchanged between FLUENT and CFX: GAMBIT (FLUENT) meshes were simulated with CFX and ICEM (CFX) meshes were simulated with FLUENT. The results are given in Tab. 5.

The first lines repeat the information already given in Tab. 3 and Tab. 4. As discussed above, the maximum temperatures of the tile and thimble decreased with a higher number of cells for these meshes. The next lines show the results for the ICEM (CFX) meshes simulated with the FLUENT program. The values for the maximum temperatures of the tile and thimble increase (for the tile from 1700 °C to 1763 °C, for the thimble from 1157 °C to 1176 °C), while the pressure loss continues to decrease. However, all results are in the range of the results given above. With an increasing number of cells, both programs asymptotically yield the same results.

The results for the GAMBIT mesh multijet19 simulated with CFX differed considerably from the results obtained with FLUENT. The temperatures suddenly were about 500 K higher, the pressure loss stayed in about the same range. This case was discussed with the CFX support team. Mesh resolution near the heat transfer surface was quite coarse; the y+ values probably were too high. Since this region was meshed with tetrahedrons, it probably also contained some pyramidal elements that could not be treated properly by CFX. The GAMBIT mesh did not meet the needs of the CFX solver.

For the FLUENT simulations, 1/6 of the geometry was meshed. For the CFX simulations, 1/12 was meshed. To test the influence of symmetry, the FLUENT mesh was cut into two parts and the remaining 1/12 was simulated. The results are given in Tab. 5, they are the same as for the 1/6 geometry. The CFX mesh was doubled to simulate 1/6 of the geometry. Due to a licence problem, this simulation was run on FLUENT. The results were the same as for the 1/12 geometry (Tab. 5). Symmetry did not affect the simulations.

This investigation shows that the two solvers cannot be compared without taking meshing effects into account. Sometimes, the meshes cannot be interchanged easily, since both solvers work differently and a different mesh quality is expected. CFX has the disadvantage of not working in 2D and not accepting pyramids as elements, while FLUENT is more tolerable to a bad cell quality. However, CFX is faster. Generally, both programs yield adequate results. A recommendation for one or the other for this test case can not be given.

6 Avoiding numerical errors: Best-practise study

Numerical errors were defined in chapter 3. The issue of spatial discretisation (mesh density) was discussed in the chapter above. Now, iteration errors and discretisation errors will be discussed [30]. As an example, the reference case (geometry HEMJ J1a, helium mass flow 6.8 g/s at an inlet temperature of 634 °C and an inlet pressure of 100 bar, and a heat load of 10 MW/m²) will be simulated with the CFX meshes described in chapter 5 on CFX 10. In a so–called “best-practice study” [4], possible error sources shall be investigated systematically.

An iteration error [3] is the difference between a fully converged solution and a solution after iteration step “n”. To check whether a simulation is fully converged, the maximum residuals are observed. If the (weighted) difference between iteration step “n” and “n-1” drops to values smaller than 10^{-3}, sometimes 10^{-4}, the simulation is considered to be converged. It should be noted that the “maximum residual” may be defined differently in different codes. This convergence criterion is supposed to drop monotonically. Together with the residuals some monitoring points, for example, temperature in a critical part of the geometry or outlet pressure should be observed, preferably as a function of the residual. Additionally, all balances should be checked.

A discretisation error [3] is the error between a converged solution on a grid and a solution on an ideal, infinitesimally fine grid. To assess it, the dependence of the solution on the mesh density should be checked. In addition, simulations should be run on one mesh with different discretisation schemes. CFX allows to constantly change between first and second order discretisation schemes by defining a blending factor. In FLUENT, the user can only switch between first and second order.

To check the errors, the following simulations were run:

- Coarse mesh, first-order discretisation (upwind scheme): converged in a stationary solution, maximum residuals < 10^{-4}

- Coarse mesh, first-order discretisation with 50% second-order blending: converged in a stationary solution, maximum residuals < 10^{-4}
- Coarse mesh, first-order discretisation with 75% second-order blending: converged in a stationary solution, maximum residuals < 10^{-4}
- Medium mesh, first-order discretisation with 75% second-order blending: converged, maximum residuals < $1.1 \cdot 10^{-3}$, tending to instationary effects
- Fine mesh, first-order discretisation with 75% second-order blending: not converged, maximum residuals < $1.6 \cdot 10^{-2}$, showing instationary effects

Fig. 15 shows the maximum residual over the number of iteration steps for the coarse mesh. On the left side, the simulation was run with the first-order upwind discretisation. After 350 iterations, the solution seemed to be converged. When stopping it and switching to a blending of 75% second order, the residuals go up and drop again with the number of iterations. This shows that the solution was not fully converged, and that a second-order simulation may improve accuracy. This is also clear from Fig. 16 showing the temperatures of the tile and thimble over the iteration steps for the same simulation. The solution seems to be converged for the first-order simulation. After switching to 75% second order, it drops again.

In Fig. 17, the integral balances are shown over the maximum residuals for the coarse mesh and the simulation with 75% second order. Obviously, the maximum residual is expected to drop below 10^{-3} to reach a state where all balances are fulfilled. Near 10^{-4}, the results do not change any more.

Fig. 18 shows the behaviour of two critical design parameters, static pressure difference and maximum temperature of the thimble, both over the maximum residual. Again, the maximum residual is supposed to drop below 10^{-3} at least to reach a steady state for all design parameters. Near 10^{-4}, the results do not change any more.

Tabs. 6 to 13 show the results of the investigation and the mesh study discussed above (chapter 5). For a higher-order discretisation scheme and a finer mesh, the maximum temperatures of the tile and thimble decrease (tile from 1857 °C to 1788 °C, thimble from 1286 °C to 1224 °C), pressure loss decreases from 1.26 to 1.21 bar, and the change becomes asymptotically smaller.

Conclusion

Simulations were run using three discretisation schemes (upwind, upwind blended with 50% second order, and upwind blended with 75% second order) and three different meshes (coarse, medium, and fine). The simulations were performed in accordance with best-practice guidelines for computational fluid dynamics in order to quantify and minimise numerical errors. When using a higher-order discretisation scheme and a finer mesh, maximum temperatures of the tile and thimble decrease, pressure loss decreases, and the change becomes asymptotically smaller. This indicates the conservative nature of the design.

7 Code validation by experimental investigations

To validate the simulation results, to demonstrate the feasibility and performance, and to optimise the parameters of the design, experiments have to be carried out in a helium loop which can be operated at high pressure, high gas temperature, and moderate heat load. The HEBLO (**He**lium **B**lanket Test **Lo**op) facility is available for these investigations. The experimental results are compared with the results simulated by CFD codes under the same boundary conditions. In this way, data for code validation are provided and simulations for real divertor conditions become more reliable.

Two different experimental campaigns were run: an enlarged, 10:1 mock-up provided more space for a detailed instrumentation and a 1:1 mock-up allowed for experiments with a higher heat load. Both will be discussed below.

Description of the HEBLO experimental facility

The facility is outlined schematically in Fig. 19. It consists of a main loop with the compressor as the main part and a test loop which houses the mock-up. The link between them is a temperature equalisation unit and a heat exchanger. The helium gas is supplied from pressure bottles. To minimise the gas losses, a helium supply and retrieval system is part of the HEBLO facility. The test loop can be operated at a helium temperature of up to 450 °C, a pressure of 80 bar, and a maximum mass flow of 120 g/s in the test section. The main loop is operated at 80 bar, 50 °C, and a mass flow of 330 g/s in the compressor. With HEBLO, the DEMO divertor operation conditions (100 bar, 600 °C) cannot be fully reached. Tests were therefore run under boundary conditions with a Reynolds number chosen to be analogous to the reference design conditions. More details about HEBLO can be found in [5].

8 Experiments using a 10:1 mock-up

8.1 Description of the test section

Experiments were run with a 10:1 mock-up, because it allows for a more detailed instrumentation. All details about the campaign with can be found in [5], a summary in [6]. Fig. 20 shows the test section made of steel (15Mo3, density 7850 kg/m^3, heat capacity 584 J/kgK, thermal conductivity 42 W/mK) and the cartridge made of stainless steel 1.4571. It contained 60 pressure sensors. 38 of them were installed in the heat transfer area of the head and 22 were distributed over the whole test insert to measure the temperature in the structure or in the gas room. The pressure was measured at 6 positions by absolute or differential pressure sensors. Sensor distribution is shown in Figs. 21 and 22.

A heater system (Fig. 23) was fixed to the head of the mock-up. From the top to the bottom, the heater system consisted of a ceramic heater plate, a layer of graphite foil (thickness 0.5 mm), a copper plate of 15 mm thickness, and another layer of graphite foil of 1.0 mm in thickness. This set-up was used to ensure a uniform heat distribution of max. 0.4 MW/m² over the head of the mock-up.

8.2 Experiments

Experiments were run at different heat loads, a helium inlet temperature between room temperature and 400 °C, and different mass flows (38 g/s corresponds to the same Reynolds number as in the original DEMO design, additionally, 40, 60, 80, 100, and 120 g/s were chosen). The heat load was adapted to the power that could be removed by helium. It could not be measured directly.

8.3 CFD modelling

Only the upper part of the mock-up was used for CFD modelling without the drillings for the instrumentation. The heater, copper plate, and foils were included in the model; this improved the accuracy of the simulations.

Only 1/6 of the geometry was meshed with GAMBIT [20]. The mesh contained about 2.6 million cells and was comparable to the FLUENT meshes mentioned above in chapter 5.1. Only FLUENT was used for the simulations. The set-up of the simulations corresponded to that described in chapter 4.5. The RNG k-ε turbulence model and second-order discretisation were applied. The only difference was that losses over the side walls were taken into account.

8.4 Comparison of experimental and simulated results

As an example, Figs. 24 a - c compare the experimental and simulated results for the inlet temperature of 250 °C (D250H1 in internal designation) at a heating power of 3.0 kW and a mass flow of 40 g/s. The values are shown over the radius reflecting the positions of the thermocouples (see Fig. 21). The top row of thermocouples represents the values measured/simulated next to the heated surface. The bottom row gives the values measured/simulated next to the cooled surface and the middle row the values measured/simulated in between. The distance of the thermocouples from the heated surface varies for the middle and the bottom rows. No difference was made between thermocouples placed directly above a jet hole and others not placed directly above, i.e. at the radii 12, 37, and 62 mm.

All figures display in blue the results of the first experiment, in pink the values from its repetition, and in green the simulated results. Some thermocouples are redundant. Sometimes, the experiments were difficult to reproduce.

Usually, the simulated temperatures matched the measured results sufficiently. The simulation points were all within the range of the measurements. They lay between the measured points and their repetition within a radius smaller than 35 mm. For positions with a bigger radius, the values matched even better. Usually, the bottom row of thermocouples next to the heat transfer surface fitted the values better. Furthermore, the measurements made at higher mass flows seemed to match better than those at lower mass flows [5].

Tab. 14 and Fig. 25 show a comparison of the pressure loss values measured during the experiment and simulated with FLUENT. The values measured at 120 g/s for D250H-1 and D250H-2 were out of range of the meters. The CFD program constantly overestimates the pressure loss. It is unusual that the deviation stayed the same over the whole range of mass flow investigated, because pressure loss dependence on the mass flow is quadratic.

8.5 Discussion and conclusion

Agreement between simulation and measurement is best for the thermocouples close to the fluid-solid interface (the jet impingement surface, the bottom row). In this region, deviation is about 7%. This indicates that the fluid simulation result is close to reality and that other sources of error may have to be taken into consideration. Possibly, the simulations can be improved by taking into account heat transport over the insulation of the mock-up or modelling of the temperature-dependent material parameter for the solids has to be improved.

Further experiments were needed to improve the heating system and heat losses had to be measured. The simulations were to consider these losses by including the insulation. This was achieved by a 1:1 mock-up in the following test campaign.

9 Experiments using a 1:1 mock-up

9.1 Description of the test section

The objective of this second experimental campaign was to conduct experiments as closely as possible to the real operating conditions. The first test series [5] with a 10:1 mock-up was successful, but revealed some problems with the heating unit. Use of the new 1:1 mock-up was aimed at improving the heating system and reducing the number of thermocouples disturbing the heat flux.

Under a joint project with the Georgia Institute of Technology, Atlanta, a copper body was designed, which was tapered in the direction of the cooling finger [7], [31], [32]. Fig. 26 shows the design of the mock-up. Copper was chosen because of its high heat conductivity. As a result, heat loads of 2 MW/m² were expected to be reached with a 750 W heater.

The manufactured mock-up is shown in Fig. 29. The thimble, cartridge, and the cooling finger were made of brass for easier machining. Thermal conductivity of brass is close to that of tungsten (brass: 119 W/mK, tungsten 124.6 W/mK at 650 °C). The cartridge was made by electron discharge machining (EDM). The other parts were made by milling.

A standard T-part was used to connect to the HEBLO tubing. Crosses after the T-part contained the instrumentation (thermocouples and pressure sensor connections sensors to measure the inlet and outlet temperature and pressure).

The mock-up was equipped with 10 thermocouples (TCs): four TCs (Ø 0.5 mm) were placed in the proximity of the cooled surface to measure local temperature (Fig. 27). Three TCs (Ø 0.5 mm) were installed in the neck of the copper part to measure the incident heat flux (Fig. 28) and two TCs (Ø 1.59 mm) were placed near the heater for safety reasons. A 10th TC was put into the small gap on top of the heater and copper.

9.2 Experiments

At the Georgia Institute of Technology, the new mock-up was tested first in an air loop. All details about the experiments can be found in [31]. The experiments were simulated at Georgia Tech with FLUENT and mesh V6. The agreement was excellent and documented in [31], [32].

Experiments were then run in the HEBLO facility at a constant inlet temperature of 35 °C, 80 bar, and mass flows of 1.2 g/s, 2.6 g/s, 3.6 g/s, 4.7 g/s, and 6.3 g/s. The value of 3.6 g/s approximately corresponded to the nominal design of 6.8 g/s, if the Reynolds number was kept constant (about 21,000). Two power inputs, 227 W and 455 W, corresponding to 1 and 2 MW/m², were chosen for the heater.

During the experiments, the inlet temperature was increased to 38 °C. Due to the small mass flows, it was difficult to control the temperatures adequately. The measurements were repeated twice. Reproducibility was good [7].

9.3 CFD modelling

Meshing was originally done with the commercial product GAMBIT [20] for runs with FLUENT [19] at the Georgia Insitute of Technology. Due to symmetry reasons, it was only necessary to mesh half of the geometry. The mesh (Fig. 30) had to be adapted to CFX. It consisted of 1.55 million cells with the quality equi-size skewness of 0.953, an equi-angle skewness of 0.958, and an aspect ratio of 25.6 (so-called mesh V6mod). The material parameters were taken from [16], and, the parameters of the insulation materials from the internet pages of the suppliers. They are listed in Tab. 15.

The simulation model is shown in Fig. 31. Tubing was not simulated, but the insulation was included in the model. On the outer boundary of the insulation – the external surface – natural convection was assumed. It was assessed using analytical correlations [33]. At the bottom, on the long sides, and at the top, a value of 5 W/m²K was determined taking into account the outer temperature of 20 °C. In the cylindrical opening of the insulation, a value of 35 W/m²K was estimated at an ambient temperature of 68 °C. Additionally, a constant temperature condition was set on the free top of the heater and the free top of the copper part. For this purpose, a thermocouple TC10 was installed that was installed in the opening of the insulation (see also [31]).

The experiments were then simulated with ANSYS CFX 11. The mass flow, inlet temperature and inlet pressure were taken from the measurements. The heat load was not measured directly, it was set to the nominal value of 227 W or 455 W (1 or 2 MW/m² on the top surface of the thimble).

9.4 Post-experimental simulations for air with mesh V6mod and CFX

The air experiments at the Georgia Institute of Technology were also simulated with CFX and mesh V6mod by the Forschungszentrum Karlsruhe. Tab. 16 shows the results of a test at an air mass flow of 3.16 g/s. In this case, the Reynolds number (~ 21,000) corresponded to the Reynolds number in the DEMO reference design. To improve the agreement especially for TC1 to TC4, the locations relevant to heat transfer, the boundary temperatures were reduced. For both free surfaces, the value was set to 265 °C. The agreement for TC1 to TC4 was good and ranged within a few degrees, while the agreement for the other thermocouples was within 40 K. Fig. 32 compares the results of the air experiments with the results simulated over a range of mass flows. Pressure loss of the air experiments is underestimated by a few percent by the CFX simulations.

9.5 Comparison of experimental and simulated results from HEBLO

Tabs. 17 and 18 list the results of the simulations in comparison to the experimental results, second test series, for mesh V6mod, at a heat load of 1 MW/m² (heater power 227 W) and 2 MW/m² (heater power 455 W). Only the results for a mass flow of 3.6 g/s are shown. Due to the Reynolds number analogy (Re about 21,000), this mass flow corresponds approximately to the nominal design mass flow of 6.8 g/s. Figs. 33 and 34 compare the results graphically for all mass flows.

Agreement between experimental and simulated results is good. The temperature values agree best for the thermocouples T5 to T9. With increasing mass flow, agreement for thermocouples T1 to T4 improves. This was observed in [5] already. The highest mass flow of 6.3 g/s showed the best agreement. Agreement for a heating power of 227 W was better than for 455 W.

The simulated pressure loss results underestimate the measured values by about 20%. This is surprising and contradictory to earlier results [5].

9.6 Discussion and conclusion

Agreement between experimental and simulated results is good. The thermohydraulic code provides acceptable results with resprect to the temperature distribution, while pressure loss is underestimated by about 20%.

Scaling the experimental pressure loss to the real operating conditions of a divertor in a fusion power plant (100 bar instead of 80 bar, inlet temperature 634 °C instead of 38 °C) would result in a pressure loss of 1.2 bar per cooling finger. The scaled results of the simulations would give a pressure loss of 1.3 bar per cooling finger. Both values correspond to those of the best-practice study [30], where pressure losses of about 1.2 bar were simulated.

10 Parametric study for design optimisation

A variety of HEMJ design options were simulated with FLUENT to optimise the design and to propose a reference design [8]. Tab. 19 gives an overview of the options. The jet-to-wall distance h, the diameter of the jet holes, and the number of jets were investigated among other parameters. Target values were the maximum thimble temperature which is limited by the material parameters and the pressure loss.

10.1 Parameter field

A parameter field was defined to test most of these parameters. This field mainly consisted of deviations of a basic design, J1a, but also contained some special designs, such as the single-jet design. The basic design J1a is obvious from the technical drawing, Fig. 35.

Details of the parameter field are summed up in Tab. 19: options J1a, J1b, and J1c differ by the jet-to-wall distance h only. The next group, J1c, J1c0.4, J1d, and J1e, differ by the diameter of the jet holes. The latter parameter is limited. To prevent the holes from being blocked by dust particles, the jet diameter should not be smaller than 0.4 mm.

The last group, J1e to J1h, all show the same gap width h and the same flow cross-sectional area. However, this area is distributed over a different number of holes.

Special investigations of the different pitch circle diameters for the holes, tile shapes, thicker cartridges, single-jet options, and larger multijet options will not be discussed in this summary report. All details can be found in [8].

10.2 CFD simulation

Meshing was done in GAMBIT [20] in analogy to the procedure described in chapter 5. The mesh used for this study consisted of a total of about 2.3 million cells in the case of J1-a. Other design options were meshed in a similar way, but differed slightly in the total number of cells.

Simulations were done using FLUENT at heat loads of 8 MW/m², 10 MW/m², 12 MW/m², and 15 MW/m². The reference pressure for the coolant was set to 10 MPa at the inlet of the model. Three values for the mass flow (6.8 g/s, 11.5 g/s, and 15.5 g/s per finger) were simulated. The helium inlet temperature was set to 634 °C (reference conditions). The RNG (Reynolds normalised group) k-ε turbulence model was chosen, including an enhanced wall treatment.

10.3 Results and discussion

The results obtained for the maximum temperature of the thimble at the jet-to-wall distance h are shown in Fig. 36 a. The temperature remains almost unchanged. The

influence of h on heat transfer is only small. An increasing h, however, leads to a lower pressure loss and, hence, to a smaller pumping power, Fig. 36 b. An increased gap between thimble and cartridge allows the gas to flow away more easily, interaction between the jets is less pronounced. This finding is very advantageous, since it allows for a wider tolerance in mounting cartridge and thimble.
The next two figures, Figs. 37 a and 37 b, show the influence of the number of holes, which is minor only: with an increasing number (6 to 24 without the central jet), the temperature drops by about 30 degrees. The coolant then is more homogeneously distributed, which increases the cooling performance. Since the total area of flow stays the same, pressure loss remains practically unchanged.

The influence of the jet diameter D on the cooling performance is much more pronounced, as can be seen from Fig. 38 a: the thimble temperature increases considerably with the jet diameter. Bigger holes reduce the velocity of the jets and the heat transfer decreases. On the other hand, pressure loss decreases considerably with increasing jet diameter, Fig. 38 b. This parameter is the most sensitive one.

10.4 Conclusion

The jet diameter is the parameter most important to the cooling performance. The holes have to be manufactured with narrow tolerances to ensure a high heat transfer. Other parameters influence the performance of the cooling finger to a minor extent only. The jet-to-wall distance h (within the design range of 0.6 – 1.2 mm) has no major influence on the divertor performance. The number of holes has a small influence on the temperature only.

Most design options, except for J1d, f, g, h, are able to remove a heat load of 10 MW/m² in the nominal case with 6.8 g/s helium at least. All others can also remove this amount of heat, but the pressure loss rises. The limitation of 10% pumping power is not considered a hard criterion. For none of the options, the limit of 2500 °C tile temperature is exceeded.

Fig. 39 presents an overview of all J1-x design options under nominal conditions (heat load 10 MW/m², mass flow 6.8 g/s). After evaluating all design options, the design J1c was chosen for further investigation. J1c shows a good cooling performance at an acceptable pumping power. It represents a good compromise between the extreme cases J1c-0.4 and J1e.

11 Summary, conclusions, and outlook

This summary report gives an overview of thermohydraulic investigations relating to the helium-cooled divertor. The main objective was to validate the results of simulations with commercial CFD codes with experimental results and to optimise the HEMJ design.

First, numerous possible error sources were investigated systematically. Mesh density was studied and the best mesh chosen. In a best–practice approach, numerical errors were eliminated. Modelling was checked by the support teams of the commercial codes and discussed at national and international conferences.

In the next step, the simulated results were compared with experimental values obtained in the helium loop HEBLO. It was focussed on the critical design parameters of temperature and pressure loss. Agreement between measured and simulated temperature results was good. By improving the experimental set-ups, it may be further improved. For the 10:1 mock-up, the temperature deviation was about 7%. For the 1:1 mock-up, deviations between measured and simulated temperatures were about 1 - 2 K. The pressure loss always was overestimated by about 30%, which is on the conservative side. Probably, the description of the helium material properties has to be corrected.

The overall results provide confidence in the results of the numerical model and its applicability to the design of the HEMJ divertor as well as to other gas-cooled high-heat-flux components under fusion reactor operating conditions.

In the future, it will be necessary to simulate the thermohydraulic behaviour of a nine-finger unit, a stripe unit, and of the whole target plate with its internal flow paths. Experimental results are expected to result from a cooperation project with the EFREMOV Institute in St. Petersburg, Russia, and the large helium loop HELOKA which is under construction at the Forschungszentrum Karlsruhe. There, an outboard target plate will be tested. The experiments will have to be prepared, accompanied, and recalculated by CFD codes. Further simulations will have to cover the design of the test divertor module to be introduced in ITER, its tubings, pumps, filters, etc. In addition, simulations of accident scenarios like LOCA (loss-of-coolant accident) and LOFA (loss-of-flow accident) as well as of transient operation conditions will be required. In parallel, a new design shall be investigated. It shall replace the HEMJ design and contain bigger components that are easier to manufacture and control.

Acknowledgement

This work has been performed within the framework of the Nuclear Fusion Program of the Forschungszentrum Karlsruhe and is supported by the European Union within the European Fusion Technology Programme. The content of the publication is the sole responsibility of its publishers and does not necessarily represent the views of the Commission or its services.

I wish to thank T. Ihli for the HEMJ design and the generation of the parameter matrix, S. Stickel for the preparation of the CAD drawings, and S. Gordeev, M. Böttcher, P. Karditsas, I. Ovchinnikov, and P. Norajitra for the valuable discussions. Thanks also go to Prof. Abdel-Khalik and his team at Georgia Tech, Atlanta. Special thanks go to V. Widak and J. Reiser for their support.

References

[1] P. Norajitra (ed.), T. Chehtov, A. Gervash, R. Giniyatulin, T. Ihli, R. Kruessmann, V. Kuznetsov, A. Makhankov, I. Mazul, I. Ovchinnikov, J. Weggen, B. Zeep, Status of He-cooled divertor development (PPCS Subtask TW4-TRP-001-D2). Forschungszentrum Karlsruhe, Wissenschaftliche Berichte, Februar 2005, FZKA 7100.

[2] R. Kruessmann, P. Norajitra, L. V. Boccaccini, T. Chehtov, R. Giniyatulin, S. Gordeev, T. Ihli, G. Janeschitz, A. O. Komarov, W. Krauss, V. Kuznetsov, R. Lindau, I. Ovchinnikov, V. Piotter, M. Rieth, R. Ruprecht, Conceptual design of a He-cooled divertor with integrated flow and heat transfer promoters (PPCS Subtask TW3-TRP-001-D2), Part I (Summary) and Part II (Detailed Version), Forschungszentrum Karlsruhe, Wissenschaftliche Berichte, FZKA 6974 & 6975.

[3] J. Fröhlich (ed.), Numerische Berechnung turbulenter Strömungen in Forschung und Praxis. Hochschulkurs, Institut für Technische Chemie und Polymerchemie, Universität Karlsruhe (TH), 2006.

[4] M. Casey, T. Wintergerste (ed.), ERCOFTAC Special Interest Group on “Quality and Trust in Industrial CFD” – Best Practice Guidelines, 2000.

[5] R. Krüßmann, G. Messemer, K. Zinn, J. Weggen, Interner Bericht, Forschungszentrum Karlsruhe, 2007.

[6] R. Kruessmann, G. Messemer, P. Norajitra, J. Weggen, K. Zinn, Validation of computational fluid dynamics (CFD) tools for the development of a helium-cooled divertor. Proceedings of the 24th Symposium on Fusion Technology, 11th – 15th September 2006, Warsaw, Poland, Fusion Engineering and Design, 82 (2007) 2812 – 2816.

[7] R. Krüßmann, G. Messemer, K. Zinn, Interner Bericht, Forschungszentrum Karlsruhe, 2008.

[8] R. Krüßmann, Interner Bericht, Forschungszentrum Karlsruhe, 2006.

[9] http://de.wikipedia.org/wiki/Finite-Differenzen-Methode
http://de.wikipedia.org/wiki/Finite-Elemente-Methode,
http://en.wikipedia.org/wiki/Finite_volume_method.

[10] Personal communication, R. Meier-Staude, ANSYS CFX Germany.

[11] P. L. Roache, Verification and Validation in Computational Science and Engineering. Albuquerque, NM, Hermosa Publ., 1998.

[12] U. Mehta, Guide to credible computational fluid dynamics simulations, AIAA Paper 95-2225, June 1995.

[13] T. I.-P. Shih, Estimating Grid-Induced Errors in CFD Solutions. In: D. A. Caughey, M. M. Hafez (ed.), Frontiers of Computational Fluid Dynamics 2006, World Scientific, New Jersey, 2006.

[14] P. Norajitra, R. Kruessmann, S. Malang, G. Reimann, Assessment of the Integration of a He-cooled Divertor System in the Power Conversion System for the Dual-coolant Blanket Concept (TW2-TRP-PPCS12D8), Forschungszentrum Karlsruhe, Wissenschaftliche Berichte, Dezember 2002, FZKA 6771.

[15] VDI Wärmeatlas, 9. Auflage 2002, VDI-Verlag.

[16] ITER Materials Properties Handbook, 2001.

[17] European Fusion Development Agreement (EFDA): Fusion Materials Topical Group: W and W-alloys. Meeting Garching (D), 21st January 2008.

[18] J. Reiser, P. Norajitra, V. Widak, W. Krauss, He-Cooled Divertor for DEMO: Fabrication Technology for Tungsten Cooling Fingers. Jahrestagung Kerntechnik 2008, Hamburg, 27.-29. Mai 2008, Berlin: Inforum GmbH 2008, S. 680-684.

[19] Fluent, Version 6.2.16 and 6.3.26, Fluent Inc., 2005 and 2006, www.fluent.com.
[20] Gambit, Version 2.2.30 and 2.3.16, Fluent Inc., 2005 and 2006, www.fluent.com.
[21] ANSYS CFX5, CFX10, and CFX11, ANSYS Inc., 2006, www.ansys.com.
[22] ANSYS ICEM11, ANSYS Inc., 2006, www.ansys.com.
[23] FLUENT 6.2 Documentation, 2006.
[24] P. Galphin, A. Bakker, The new wave of fluids technology. Advantage, Vol. II, 2 (2008), 17 - 19
[25] CFX 11 Documentation, 2007.
[26] W. Vieser, T. Esch, F. Menter, Heat Transfer Predictions Using Advanced Two-Equation Turbulence Models. CFX Validation Report CFX-VAL10/0602, 2002.
[27] M. Behnia, S. Parneix, P. Durbin, Accurate modelling of impinging jet heat transfer. Annual Research Briefs, Center for turbulence research, NASA Ames/Stanford University, 1997, 149 – 164.
[28] Personal communication, S. Gordeev, HEBLO-Meeting 2005.
[29] GAMBIT Training Kurs, Darmstadt 2003.
[30] R. Krüßmann, R. Meier-Staude, Numerical Validation of Thermohydraulic Simulations for the Development of a Helium-cooled Divertor. Jahrestagung der Kerntechnischen Gesellschaft Deutschland, Karlsruhe, May 2007, Proceedings: Berlin: INFORUM GmbH (2007), 600 - 603.
[31] J. B. Weathers, Thermal performance of helium-cooled divertors for magnetic fusion applications. Master Thesis, Georgia Institute of Technology, August 2007.
[32] J. B. Weathers, L. Crosatti, R. Kruessmann, D. L. Sadowski, S. I. Abdel-Khalik, Development of Modular Helium-cooled Divertor for DEMO Based on the Multi-Jet Impingement (HEMJ) Concept: Experimental Validation of Thermal Performance. Proceedings of the 8th ISFNT, Heidelberg, Oct. 2007, Fusion Engineering and Design, doi:10.1016/j.fusengdes.2008.06.045.
[33] F. Incropera, D. DeWitt, Fundamentals of Heat and Mass Transfer, 5th Ed., John Wiley & Sons, Hoboken, NJ, 2002.
[34] Fachtagung “Simulation turbulenter Strömungen”, Dec. 2007, Munich, organised by ANSYS

List of Tables

List of Figures

Fig. 20: Test section for the 10:1 campaign.

Fig. 21: Positions of temperature measurement.

Fig. 22: Positions of pressure measurement.

Fig. 23: Schematic representation of the arrangement of the electrical heater on top of the HEMJ model.

Fig. 24: Comparison of measured and simulated results for D250H1, 40 g/s.

Fig. 25: Comparison of pressure losses, experimental and simulated results.

Fig. 26: Design sketch of the 1:1 mock-up (D. Sadowski, Georgia Tech).

Fig. 27: Positions of the thermocouples TC 1 to TC 4 (D. Sadowski, L. Crosatti).

Fig. 28: Positions of the thermocouples TC 5 to TC 9 (D. Sadowski, L. Crosatti).

Fig. 29: Photographs of the mock-up and the cartridge (by L. Crosatti).

Fig. 30: Mesh V6 for thermohydraulic simulations (detail near the heat transfer surface).

Fig. 31: Simulation model.

Fig. 32: Comparison of experimental and simulated temperature and pressure loss results for the air tests.

Fig. 33: Comparison of measured and simulated temperatures and pressure losses (mesh V6mod, second test series) in the different parts of the mock-up for the case of 227 W.

Fig. 34: Comparison of measured and simulated temperatures and pressure losses (mesh V6mod, second test series) in the different parts of the mock-up for the case of 455 W.

Fig. 35: Technical drawings of tile, thimble, and cartridge for J1a.

Fig. 36: Results for jet-to-wall distance h.

Fig. 37: Results for the number of jets.

Fig. 38: Results for the jet diameter D.

Fig. 39 a: Max. thimble temperature over mass flow for all design variants J1x.

Fig. 39 b: Max. pressure loss over mass flow for all design variants J1x.

Tables

Tab. 1: Material properties relevant to flow simulation

Material	Helium	Tungsten	WL10	Steel (represented by T91 at 900 °C)
Density [kg/m³]	Ideal gas, $M = 4.0026$ kg/mol	19300	18750	7412.07
Dynamic viscosity [kg/ms]	$\eta = 0.4646*10^{-6}*T^{0.66}$	-	-	-
Specific heat capacity [J/kgK]	$Cp = 5193$	$Cp = 119.10 + 3.4659*10^{-2}*T - 3.4097*10^{-6}*T^{2}$	$Cp = 131.24957 + 0.0276933*T - 1.3059564*10^{-5}*T^{2} + 3.4090909*10^{-9}*T^{3}$	1202.11
Thermal conductivity [W/mK]	$\lambda = 3.623*10^{-3}*T^{0.66}$	$\lambda = 207.95 - 0.13579*T + 5.6484*10^{-5}*T^{2} - 7.8349*10^{-9}*T^{3}$	$\lambda = 144.78732 - 0.079055872*T + 4.6411274*10^{-5}*T^{2} - 1.0419238*10^{-8}*T^{3}$	23.74

M = molecular mass
T = insert temperature (in [K])

Tab. 2: Total energy balance of a model C divertor

48 cassettes (7.5°); cassette = target plates + dom + baffle+ bulk structure
Q_α = 136 MW, $Q_{heating}$ = 122 MW, fusion power = 3410 MW, total temperature difference of coolant 200 K

	Toroidal sum of 48 cassettes					**Values for one cassette**	
	Surface heat power $Q_\alpha + Q_{heating}$ (56%OB, 44%IB) (MW) *(A)*	$Q_{Neutronen, (56\%OB, 44\%IB)}$ (MW)			$Q_{surf.+Neutr.}$ (MW) *(A+B)*	$Q_{surf.+Neutr., 1 cass.}$ (MW)	Necessary He mass flow (kg/s)
		*Target plates *)*	*Bulk*	Sum *(B)*			
Outboard (OB)	198.4	*44.1*	*143.5*	187.6	386	8.042	7.733
Inboard (IB)	49.6	*34.7*	*112.7*	147.4	197	4.104	3.946
Sum	248	*78.8*	*256.2*	335	583	12.146	11.679

*) $V_{plate, 1 cassette}$ = 54057 cm^3 (value from CAD); $q_{Vol., avg}$. about 17 W/cm^3; size OB plate about 814.5 x 1000 mm^2 (tor. * pol.)

Calculation for one OB divertor plate

Heat flow density:
Mean heat flow density: about (1/48*198.4)/0.8145 = 5.075 MW/m^2
Mean equivalent total heat flow density (α+neutronic): about 1/48*(198.4+44.1)/0.8145 = 6.203 MW/m^2
Flow throughput:
Throughput for one poloidal finger row = 7.733 / 50 = 0.15466 kg/s
Throughput for one finger module = 0.15466 / 21 kg/s = 0.00736 kg/s
Temperature differences: a) DT_{Plate} = 200*(198.4+44.1)/386 = 200 * 0.6282 = 125.65 K, b) DT_{bulk} = 200 – 125.65 = 74.35 K
He temperatures:
Cassette inlet 526 °C
→ At inlet divertor plate about 600.4 °C (1st stage) or 661.3°C (2nd stage) 718.7°C (3rd stage)
outlet cassette 726 °C.

Tab. 3: Comparison of different GAMBIT meshes simulated in FLUENT

	multijet18	**multijet19**	**multijet20**	**multijet22**
Meshing				
Total number of cells	1,483,096	2,326,222	5,147,489	6,873,446
Equi-angle skewness. <0.95	0.821	0.871	0.933	0.828
Aspect ratio	3.446	8.68	41.5	12.353
Y+	0 – 49.24	0 – 56.4	0 – 17	0 – 27
Number of cells in gas jet region	290,060	500,349	1,983,661	2,183,124
Meshing strategy for gas jet region	Tet/Hybrid 0.1, 100 % Prismn	Tet/Hybrid 0.05, 100 % Prismn	Tet/Hybrid 0.03, 100 % Prismn	Tet/Hybrid 0.05, 100% Prism
Quality of mesh in gas jet region, AR /skewn.	3.43 / 0.817	3.379 / 0.824	3.349 / 0.822	3.468 / 0.820
Simulation				
Name file	Multijet18-bcok-ref1979	Multijet19-ref-korrODSconst-source9848	Multijet20-bcok-ref2554	Multijet22-ref1471
Number of iterations	1979	9848 (net: 1225 after last change of b.c.)	2554	1471
Results				
T max tile [°C]	1765.20	1711.02	1678.47	1707.67
T max thimble [°C]	1220.21	1163.71	1125.71	1164.09
Htc mean [W/m²K]; related to surface A	24697.26	29271.21	32242.7	29091.82
Surface A [m²]	3.744127e-05	3.744127e-05	3.744127e-05	3.744127e-05
Δp total [MPa]	0.135528	0.134954	0.125312	0.126
Max. velocity [m/s]	229	231	241.6	234
Energy balance				
Tin / Tout / ΔT [°C]	634.42 / 713.64 / 79.22	631.23 / 710.13 / 78.9	634.35 / 713.9 / 79.55	634.3 / 713.32 / 79.02
Qin / Q out [W/m²]	1e07 / 10195525.65	1e07 / 1015442.01	1e07 / 10237996.28	1e07 / 10169785.87
Error in energy [%]	+ 1.955 %	+ 1.54 %	+ 2.38 %	+1.70 %

Tab. 4: Comparison of different ICEM meshes simulated in CFX

	coarse	**medium**	**fine**
Meshing			
Total number of cells	207098	1,304,816	5,523,973
Angle, > 20°	28.3	28.2	28.4
Aspect ratio	-	-	-
Y+ average / in gas	13.9 / 4.2	5.5 / 1.6	-
Number of eells in total gas region	142,360	910,930	3,879,181
Meshing strategy for gas jet region	Hexaeders	Hexaeders	Hexaeders
Quality of mesh in gas jet region, AR /skewn.	-	-	-
Simulation			
Name file	JetsGrobNeu2_BF075_dt64_001	JetsGrobNeu2Mittel_BF075_dt1064_002	JetsGrobNeu2Fein_BF075_dt128_001
Number of iterations	814	1219	206
Results			
T max tile [°C]	1787.75	1771.45	1762.75 – 1763.55
T max thimble [°C]	1223.65	1198.55	1189.45 – 1190.15
Htc mean [W/m^2K]; related to surface A	-	-	-
Surface A [m^2]	3.744127e-05	3.744127e-05	3.744127e-05
Δp total [MPa]	0.1310	0.1305	0.1304
Max. velocity [m/s]	231.64	244.93	255.9
Energy balance			
Tin / Tout / ΔT [°C]	634.12 / 715.0 / 80.88	634.07 / 714.25 / 80.18	634.04 / 715.12 / 81.08
Qin / Q out [W/m^2]	1e07 / 10422759	1e07 / 10332553	1e07 / 10448533
Error in energy [%]	4.23 %	3.3 %	4.49 %

Tab. 5: Cross comparison of meshes and commercial codes

Mesh / code	**T max tile [°C]**	**T max thimble [°C]**	**Δp total [MPa]**
Multijet18 / FLUENT	1765.20	1220.21	0.136
Multijet19 / FLUENT	1711.02	1163.71	0.1345
Multijet20 / FLUENT	1678.47	1125.71	0.1238
Multijet22 / FLUENT	1707.67	1164.09	0.1261
CFX coarse / CFX	1787.75	1223.65	0.1310
CFX medium / CFX	1771.45	1198.55	0.1305
CFX fine / CFX	~ 1763	~ 1190	~ 0.1304
CFX coarse / FLUENT	1700.14	1157.04	0.1221
CFX medium/FLUENT	1751.16	1175.94	0.1174
CFX fine / FLUENT	1763.02	1179.0	0.119
Multijet19 / CFX	2257.09	1680.85	0.124
Multijet19- one twelvth	1707.62	1160.76	0.1316
CFX medium one sixth / Fluent	1751.22	1176.08	0.1164

Tab. 6: Results for the maximum temperature of the tile

Tmax,tile [°C]	Upwind (Blend Factor 0.0)	50% second order	75% second order
Coarse mesh	1857.2	1817.3	1787.8
Medium mesh			1771.5
Fine mesh			1762.8 – 1763.6

Tab. 7: Results for the maximum temperature of the tile, relative change

Tmax,tile	Upwind (Blend Factor 0.0)	50% second order	75% second order
Coarse mesh	4.2 %	2.2 %	0.8 %
Medium mesh			0,0 %
Fine mesh			- 0.4 %

Tab. 8: Results for the maximum temperature of the thimble

Tmax,thimble [°C]	Upwind (Blend Factor 0.0)	50% second order	75% second order
Coarse mesh	1286.2	1250.1	1223.7
Medium mesh			1198.6
Fine mesh			1189.5 – 1190.2

Tab. 9: Results for the maximum temperature of the thimble, relative change

Tmax,thimble	Upwind (Blend Factor 0.0)	50% second order	75% second order
Coarse mesh	6.0 %	3.5 %	1.7 %
Medium mesh			0.0 %
Fine mesh			- 0.6 %

Tab. 10: Results for the static pressure loss

Dpstat [bar]	Upwind (Blend Factor 0.0)	50% second order	75% second order
Coarse mesh	1.262	1.215	1.211
Medium mesh			1.215
Fine mesh			1.214 – 1.227

Tab. 11: Results for the static pressure loss, relative change

Dpstat [bar]	Upwind (Blend Factor 0.0)	50% second order	75% second order
Coarse mesh	3.9 %	0.0 %	- 0.3 %
Medium mesh			0.0 %
Fine mesh			- 0.1 % - 1.0%

Tab. 12: Results for the total pressure loss

	Coarse mesh	Medium mesh	Fine mesh
Dptotal [bar]	1.310 bar	1.305 bar	1.304 bar
Relative change	0.38 %	0.0 %	-0.08 %

Tab. 13: Energy balance

Energy, W	Coarse mesh	Medium mesh	Fine mesh
Qin,He	2665.8	2666.1	2666.2
Qout,He	- 2899.5	-2898.8	- 2894.4
Qin,armor (heated surface)	228.66	228.66	228.66
QSource,neutrons	4.82	4.82	4.82
Error	- 0.22	0.78	5.28

Tab. 14: Comparison of pressure loss, experimental and simulated results

Mass flow, g/s	**Exp. D250H-1 Δp, Pa**	**Exp. D250H-2 Δp, Pa**	**FLUENT Δp, Pa**
38	190	189.57	300
40	223	220.54	339
60	575	569.31	755
80	1041	1054.8	1330
100	1676	1698.5	2010
120	1939	1913.8	2876

Tab. 15: Material parameters of the 1:1 mock-up

Material	**Density ρ**	**Thermal conductivity k**		**Specific heat c_p**
	[kg/m^3]	[W/m-K]		[J/kg-K]
Steel AISI 316 SS (tee, inlet tube)	8027	16.26		502
Brass C36000 (thimble, outlet connector, jet cartridge)	8500	116		380
Rockwool, Rockwool wrapping (insulation)	130	$0.0407-10^{-4}*T+3*10^{-7}*T^2$		840
Copper C14500 (bottle)	8940	354.8		376.8
Magnesium oxide (heater)	3580	T [K]	k [W/m-K]	877
		273	42	
		400	29	
		600	20	
		800	14	
		1000	11	

Tab. 16: Comparison of experimental and numerical results, air experiments at Georgia Tech

Test Number	Mass Flow	Power	Angle	q"	ΔP	T_{red}
	[g/s]	[W]	[^{o}]	[MW/m^2]	[kPa]	[^{o}C]
7	3.16	182.2	0	0.713	22.06	265

Air loop experiments

	Value	Units	Description
Q_{Heater}	182.2	[W]	Heater Input Power
MFR	3.16	[g/s]	Measured Mass Flow Rate
Θ	0	[^{o}]	Azimuthal Position
T1	187.1	[^{o}C]	Embedded TC Ref. 1 in brass
T2	198.7	[^{o}C]	Embedded TC Ref. 2 in brass
T3	203.7	[^{o}C]	Embedded TC Ref. 3 in brass
T4	205.2	[^{o}C]	Embedded TC Ref. 4 in brass
T5	243.6	[^{o}C]	TC Ref. 5 in copper "neck"
T6	254.2	[^{o}C]	TC Ref. 6 in copper "neck"
T7	263.7	[^{o}C]	TC Ref. 7 in copper "neck"
T8	305	[^{o}C]	TC Ref. 8 in copper (maximum)
T9	305	[^{o}C]	TC Ref. 9 in copper (maximum)
T_{in}	21	[^{o}C]	Inlet Temperature
T_{out}	67.5	[^{o}C]	Outlet Temperature
P_{in}	730.84	[kPa]	Inlet Pressure
P_{out}	708.78	[kPa]	Outlet Pressure
ΔP	22.06	[kPa]	

CFX results, mesh V6mod

	Value	Units	Description
Q_{Heater}	182.2	[W]	Heater Input Power
MFR	3.16	[g/s]	Measured Mass Flow Rate
Θ	0	[^{o}]	Azimuthal Position
T1	185.6	[^{o}C]	Embedded TC Ref. 1 in brass
T2	198.6	[^{o}C]	Embedded TC Ref. 2 in brass
T3	198.4	[^{o}C]	Embedded TC Ref. 3 in brass
T4	200.8	[^{o}C]	Embedded TC Ref. 4 in brass
T5	225.8	[^{o}C]	TC Ref. 5 in copper "neck"
T6	233.1	[^{o}C]	TC Ref. 6 in copper "neck"
T7	240.6	[^{o}C]	TC Ref. 7 in copper "neck"
T8	268.0	[^{o}C]	TC Ref. 8 in copper (maximum)
T9	268.0	[^{o}C]	TC Ref. 9 in copper (maximum)
T_{in}	21.0	[^{o}C]	Inlet Temperature
T_{out}	57.4	[^{o}C]	Outlet Temperature
P_{in}	726.163	[kPa]	Inlet Pressure
P_{out}	708.78	[kPa]	Outlet Pressure
ΔP	17.383	[kPa]	

Tab. 17: Comparison of experimental and numerical results, HEBLO experiments

Test Number	Mass Flow [g/s]	Power [W]	Angle [°]	q" [MW/m^2]	ΔP [Pa]	T_{max} [°C]
227-2	3.6	227	0	1	18200	283

HEBLO Experiments

	Value	Units	Description
Q_{Heater}	227	[W]	Heater Input Power
MFR	3.6	[g/s]	Measured Mass Flow Rate
Θ	0	[°]	Azimuthal Position
T1	120	[°C]	Embedded TC Ref. 1 in brass
T2	134	[°C]	Embedded TC Ref. 2 in brass
T3	153	[°C]	Embedded TC Ref. 3 in brass
T4	137	[°C]	Embedded TC Ref. 4 in brass
T5	196	[°C]	TC Ref. 5 in copper "neck"
T6	212	[°C]	TC Ref. 6 in copper "neck"
T7	225	[°C]	TC Ref. 7 in copper "neck"
T8	288	[°C]	TC Ref. 8 in copper (maximum)
T9	288	[°C]	TC Ref. 9 in copper (maximum)
T_{in}	38	[°C]	Inlet Temperature
T_{out}	51	[°C]	Outlet Temperature
ΔT	13	[K]	
P_{in}	7851	[kPa]	Inlet Pressure
P_{out}	7762	[kPa]	Outlet Pressure
ΔP	18217	[Pa]	

CFX Results on mesh V6 mod

	Value	Units	Description
Q_{Heater}	227	[W]	Heater Input Power
MFR	3.6	[g/s]	Measured Mass Flow Rate
Θ	0	[°]	Azimuthal Position
T1	125	[°C]	Embedded TC Ref. 1 in brass
T2	135	[°C]	Embedded TC Ref. 2 in brass
T3	142	[°C]	Embedded TC Ref. 3 in brass
T4	141	[°C]	Embedded TC Ref. 4 in brass
T5	195	[°C]	TC Ref. 5 in copper "neck"
T6	209	[°C]	TC Ref. 6 in copper "neck"
T7	224	[°C]	TC Ref. 7 in copper "neck"
T8	282	[°C]	TC Ref. 8 in copper (maximum)
T9	282	[°C]	TC Ref. 9 in copper (maximum)
T_{in}	38	[°C]	Inlet Temperature
T_{out}	50	[°C]	Outlet Temperature
ΔT	12	[K]	
P_{in}	7777	[kPa]	Inlet Pressure
P_{out}	7762	[kPa]	Outlet Pressure
ΔP	15038	[Pa]	

Tab. 18: Comparison of experimental and numerical results, HEBLO experiments

Test Number	Mass Flow	Power	Angle	q"	ΔP	T_{max}
	[g/s]	[W]	[^{o}]	[MW/m^{2}]	[Pa]	[^{o}C]
455-2	3.6	455	0	2	18500	479

HEBLO Experiments

	Value	Units	Description
Q_{Heater}	455	[W]	Heater Input Power
MFR	3.6	[g/s]	Measured Mass Flow Rate
Θ	0	[^{o}]	Azimuthal Position
T1	184	[^{o}C]	Embedded TC Ref. 1 in brass
T2	209	[^{o}C]	Embedded TC Ref. 2 in brass
T3	241	[^{o}C]	Embedded TC Ref. 3 in brass
T4	214	[^{o}C]	Embedded TC Ref. 4 in brass
T5	315	[^{o}C]	TC Ref. 5 in copper "neck"
T6	345	[^{o}C]	TC Ref. 6 in copper "neck"
T7	371	[^{o}C]	TC Ref. 7 in copper "neck"
T8	488	[^{o}C]	TC Ref. 8 in copper (maximum)
T9	487	[^{o}C]	TC Ref. 9 in copper (maximum)
T_{in}	38	[^{o}C]	Inlet Temperature
T_{out}	62	[^{o}C]	Outlet Temperature
ΔT	25	[K]	
P_{in}	7849.3	[kPa]	Inlet Pressure
P_{out}	7754.2	[kPa]	Outlet Pressure
ΔP	18467	[Pa]	

CFX Results on mesh V6mod

	Value	Units	Description
Q_{Heater}	455	[W]	Heater Input Power
MFR	3.6	[g/s]	Measured Mass Flow Rate
Θ	0	[^{o}]	Azimuthal Position
T1	197	[^{o}C]	Embedded TC Ref. 1 in brass
T2	216	[^{o}C]	Embedded TC Ref. 2 in brass
T3	228	[^{o}C]	Embedded TC Ref. 3 in brass
T4	227	[^{o}C]	Embedded TC Ref. 4 in brass
T5	325	[^{o}C]	TC Ref. 5 in copper "neck"
T6	350	[^{o}C]	TC Ref. 6 in copper "neck"
T7	376	[^{o}C]	TC Ref. 7 in copper "neck"
T8	480	[^{o}C]	TC Ref. 8 in copper (maximum)
T9	480	[^{o}C]	TC Ref. 9 in copper (maximum)
T_{in}	38	[^{o}C]	Inlet Temperature
T_{out}	60	[^{o}C]	Outlet Temperature
ΔT	22	[K]	
P_{in}	7769	[Pa]	Inlet Pressure
P_{out}	7754	[Pa]	Outlet Pressure
ΔP	15208	[Pa]	

Tab. 19: Design options for multi-jet cooling

Option	Hole diam. D (mm)	Jet-to-wall distance h (mm)	Number of holes + 1 bigger central hole
J1-a	0.6	1.2	24 + 1
J1-b	0.6	0.6	24 + 1
J1-c	0.6	0.9	24 + 1
J1-c0.4	0.4	0.9	24 + 1
J1-d	0.7	0.9	24 + 1
J1-e	0.85	0.9	24 + 1
J1-f	0.794	0.9	18 + 1
J1-g	0.939	0.9	12 + 1
J1-h	1.212	0.9	6 + 1

Figures

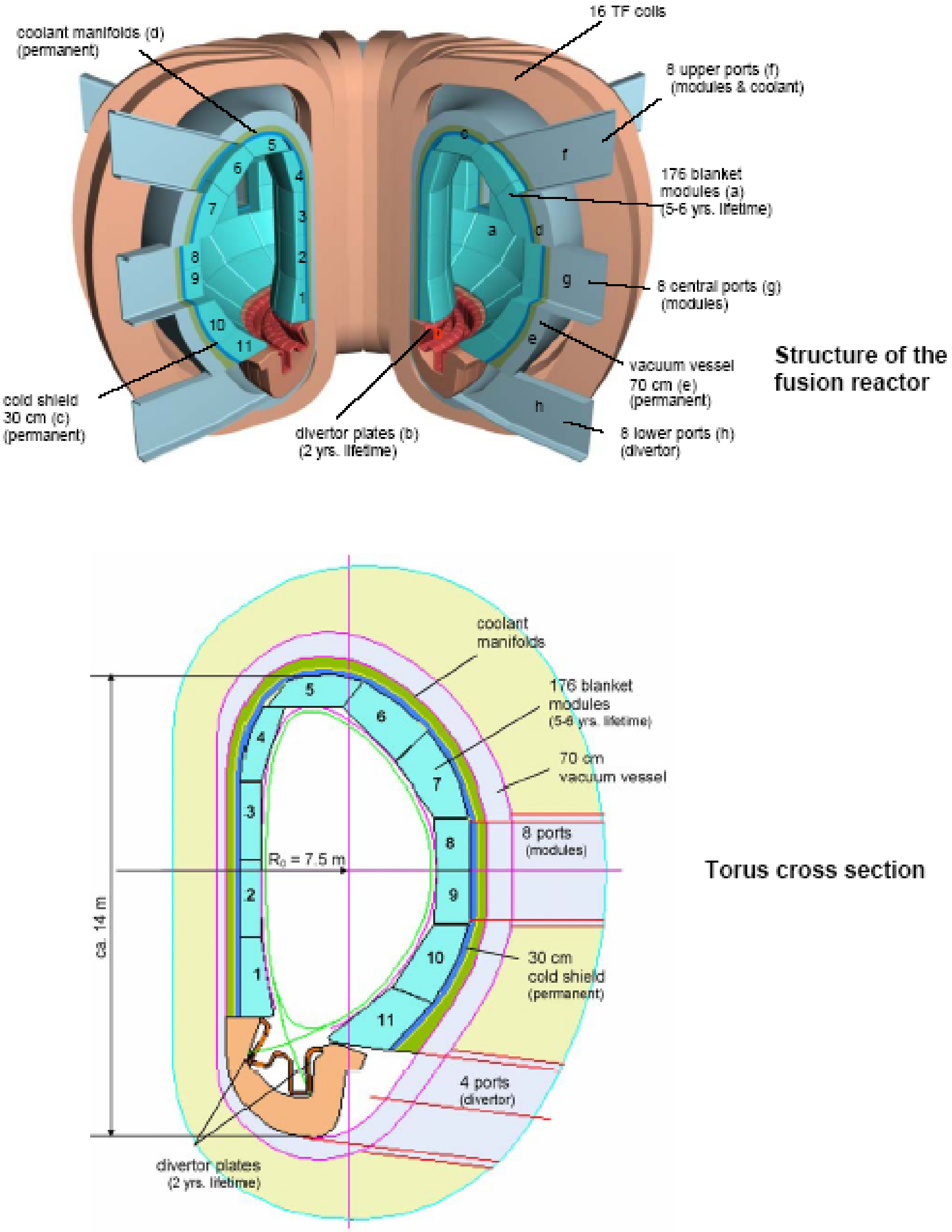

Structure of the fusion reactor

Torus cross section

Fig. 1: Fusion tokamak reactor with dual-coolant blanket and He-cooled divertor.

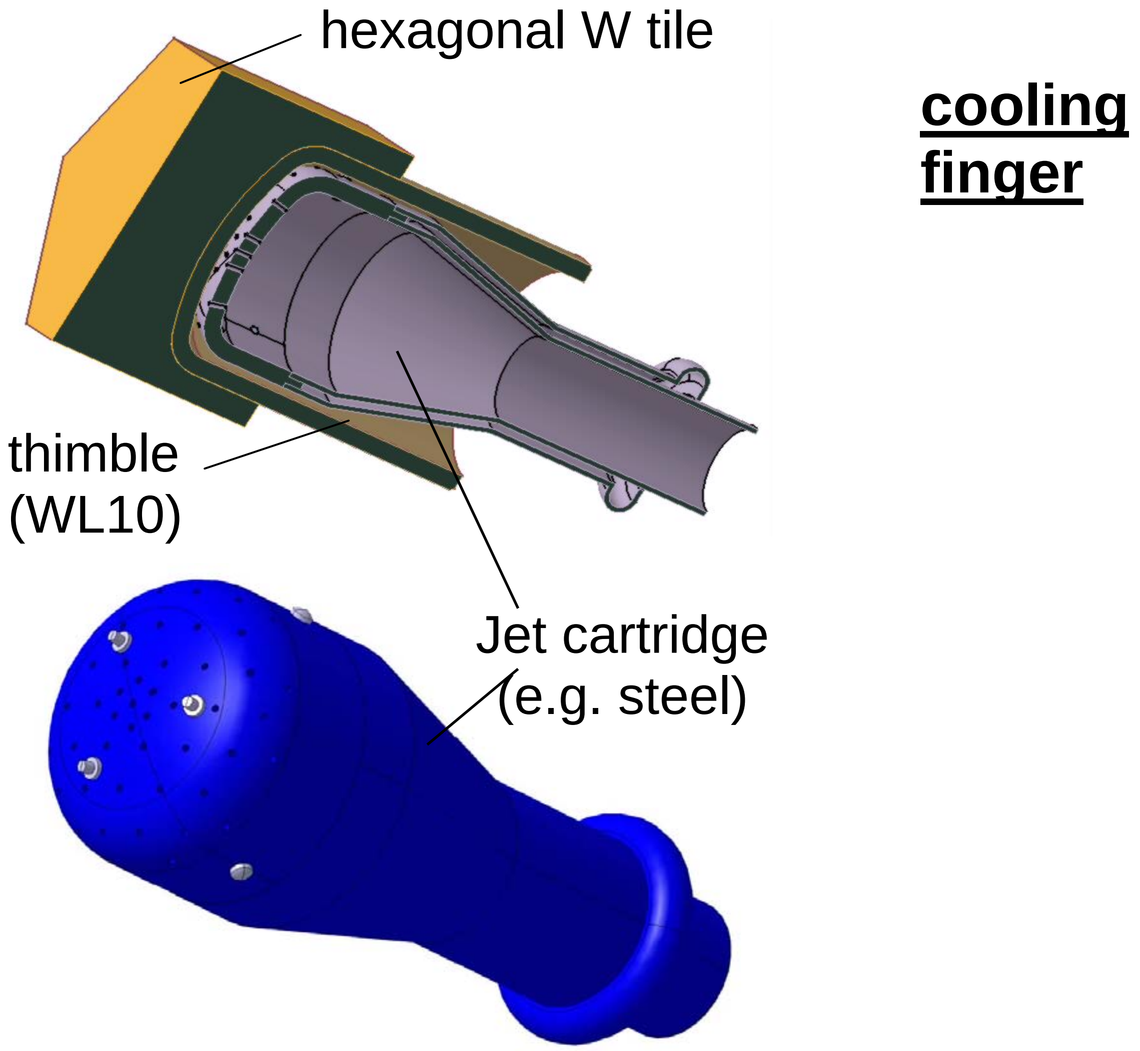

Fig. 2: Cooling finger with jet cartridge (HEMJ).

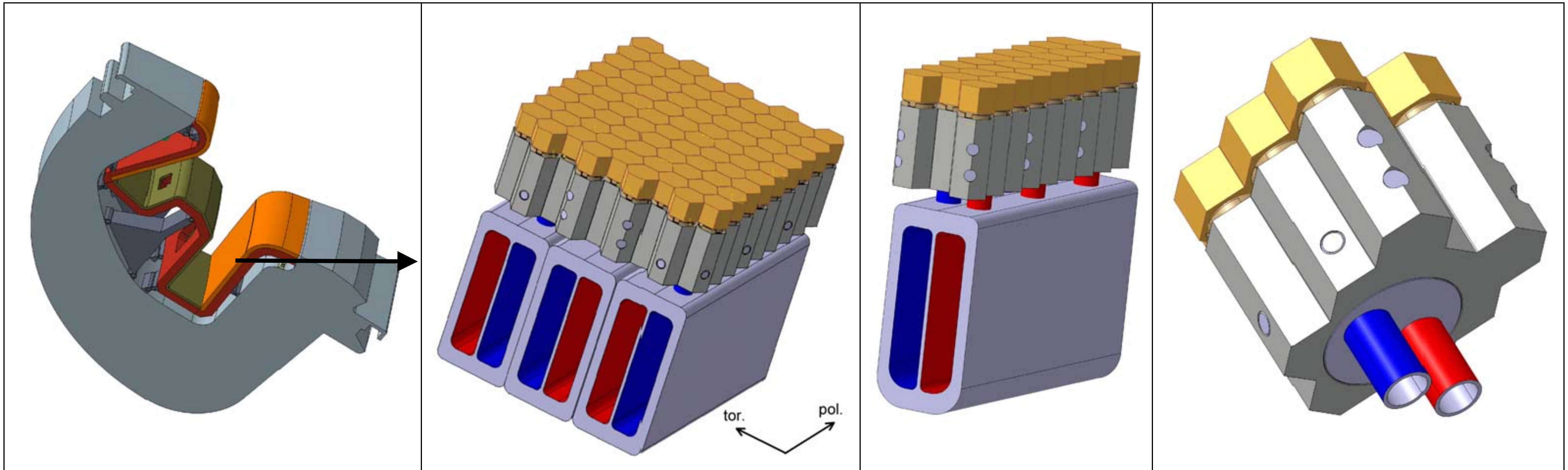

Divertor cassette body | Target plate | Stripe unit | Module with nine cooling fingers

Fig. 3: Divertor design.

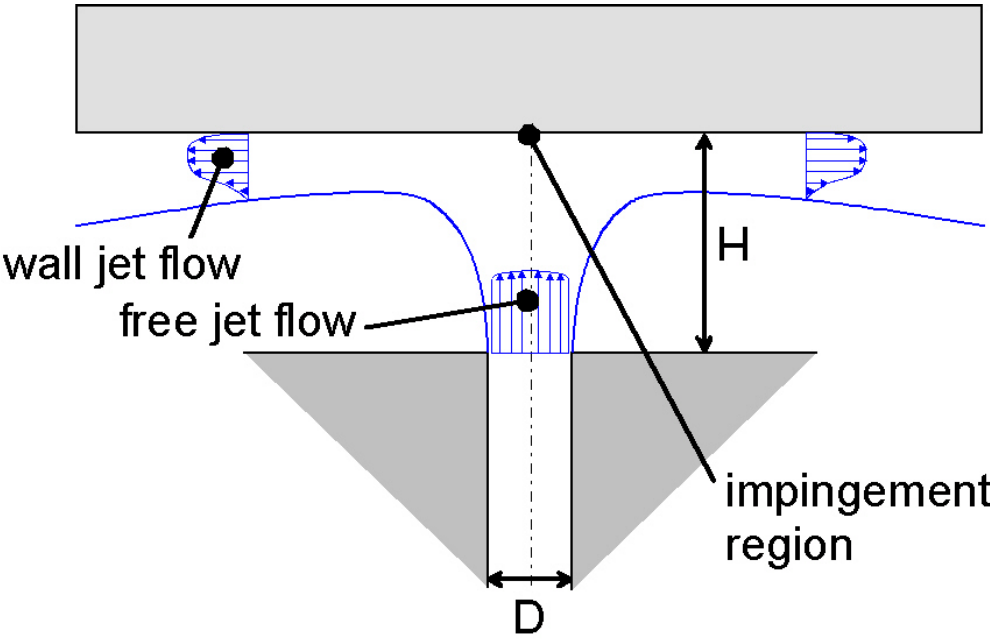

Fig. 4: Zones of an impingement jet.

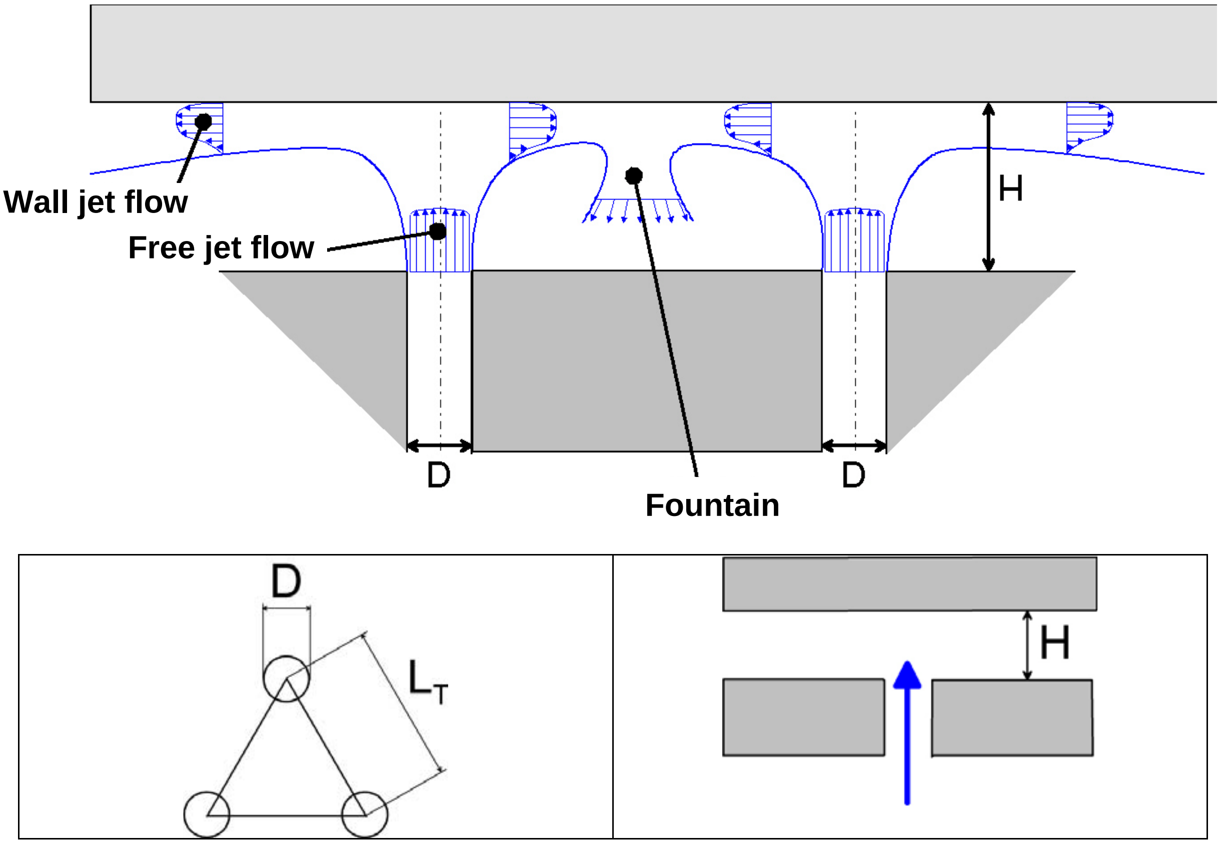

Fig. 5: Multiple impingement jet and geometrical parameter model.

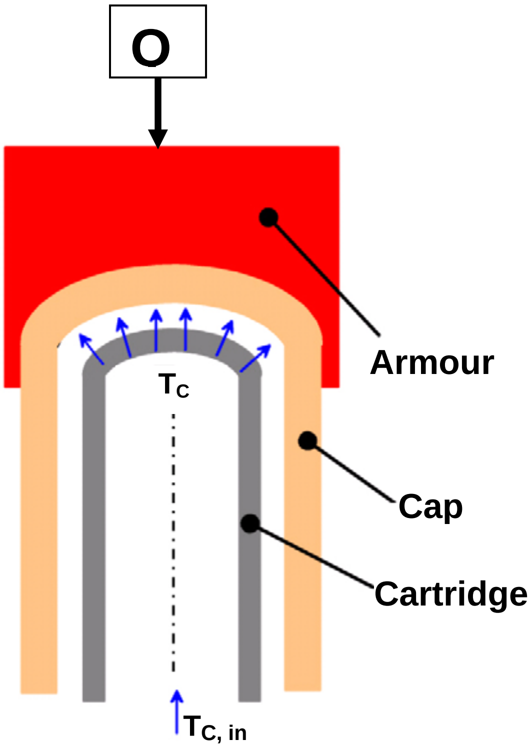

Fig. 6: Principle of a jet impingement cooling finger for the gas-cooled divertor.

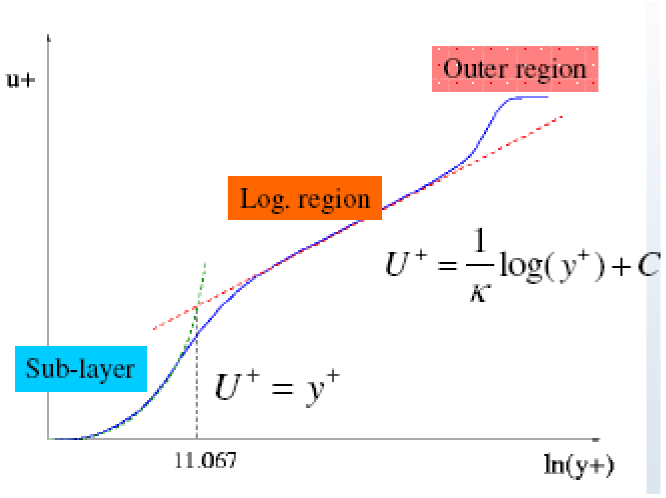

Fig. 7: Logarithmic law of the wall [33] (courtesy of ANSYS Germany).

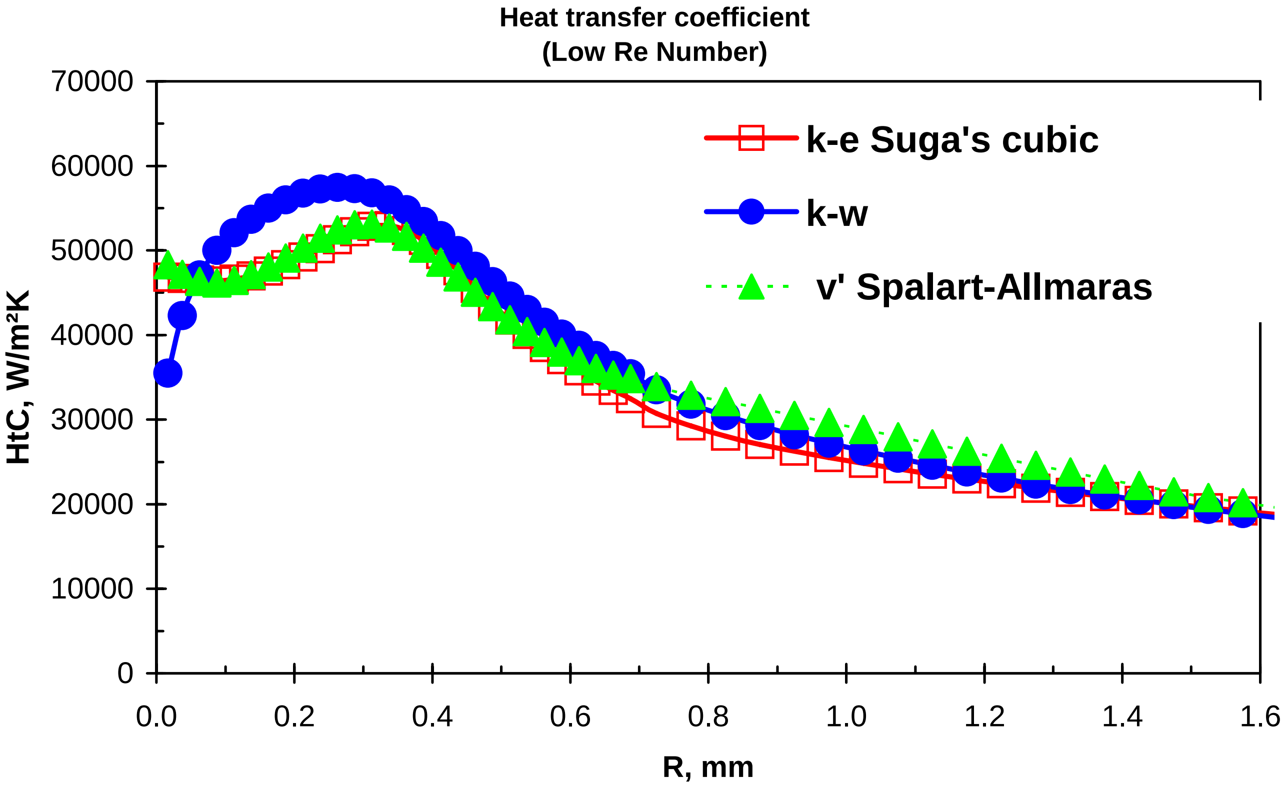

Fig. 8: Heat transfer coefficient versus distance from jet axis for different low-Re-number turbulence models (S. Gordeev).

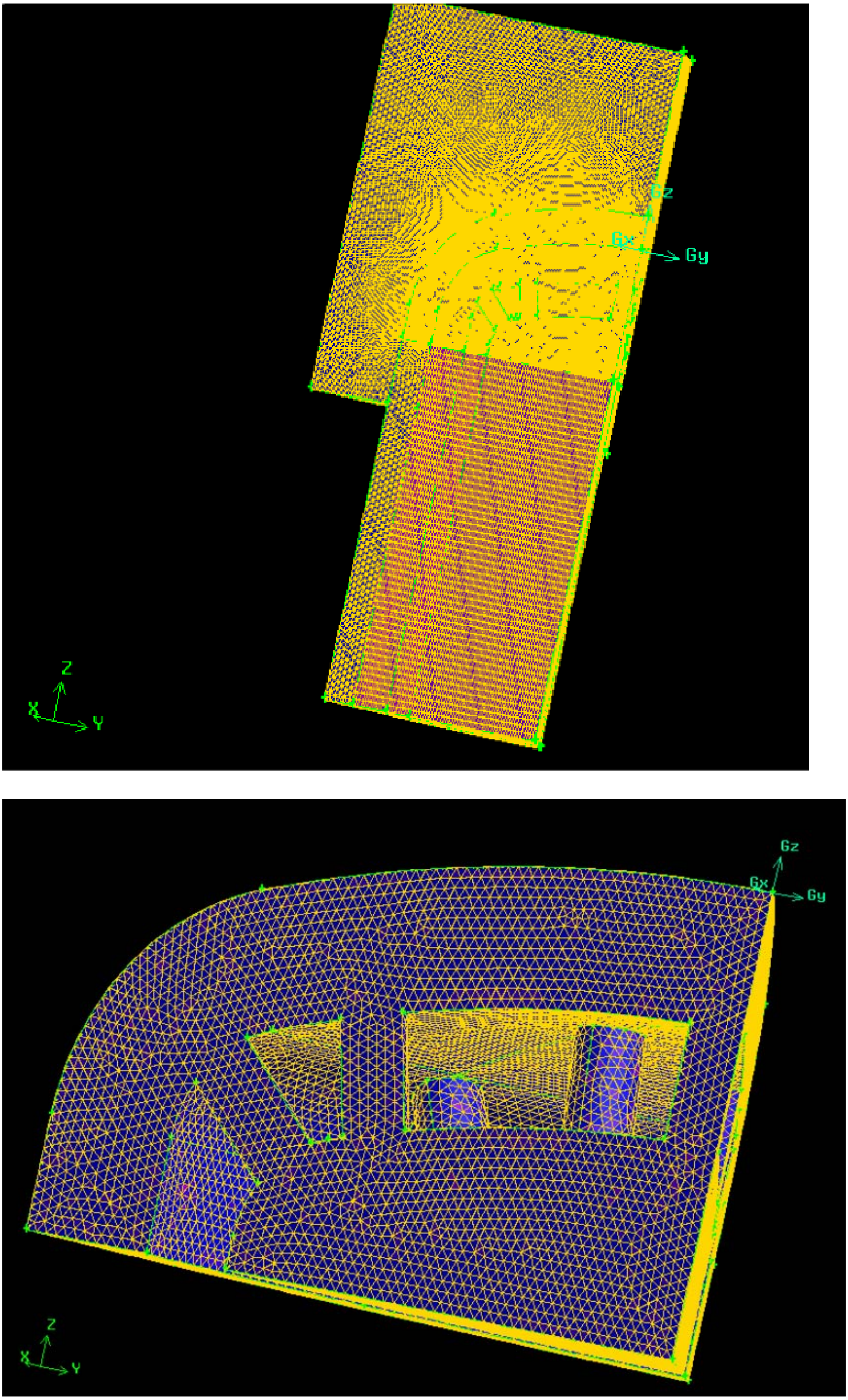

Fig. 9: Mesh made by GAMBIT for the FLUENT case **multijet18** and detail of the jet impingement region.

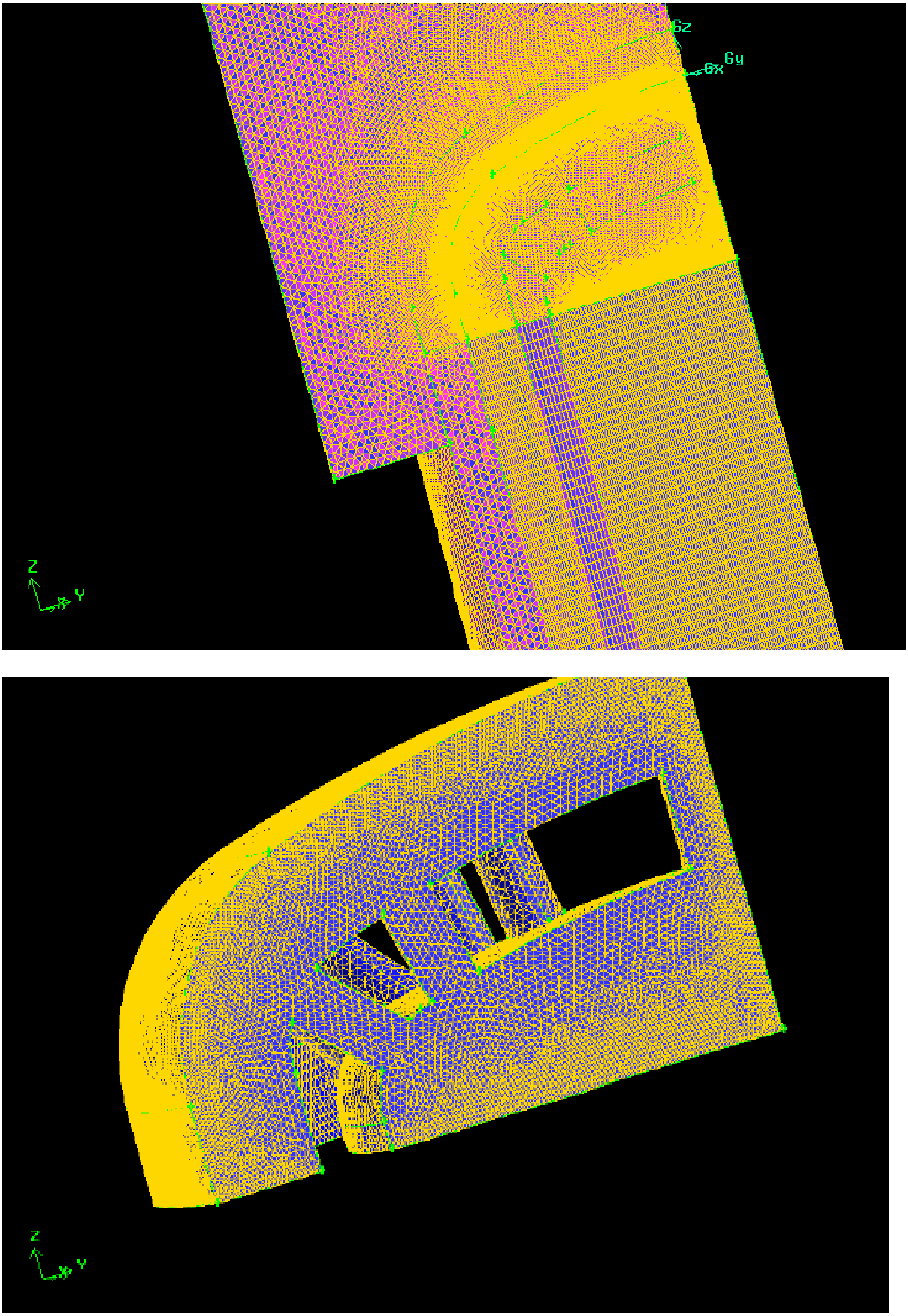

Fig. 10: Mesh made by GAMBIT for the FLUENT case **multijet19** and detail of the jet impingement region.

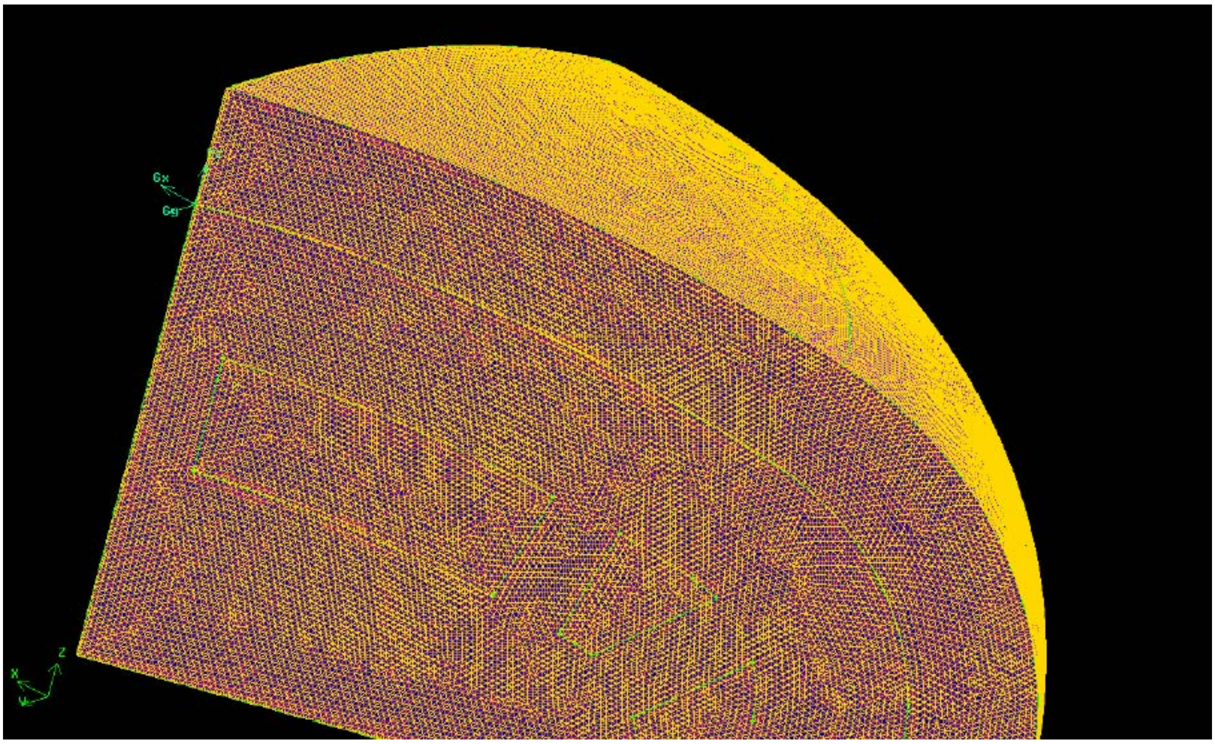

Fig. 11: Mesh made by GAMBIT for the FLUENT case **multijet22**, detail of the jet impingement region.

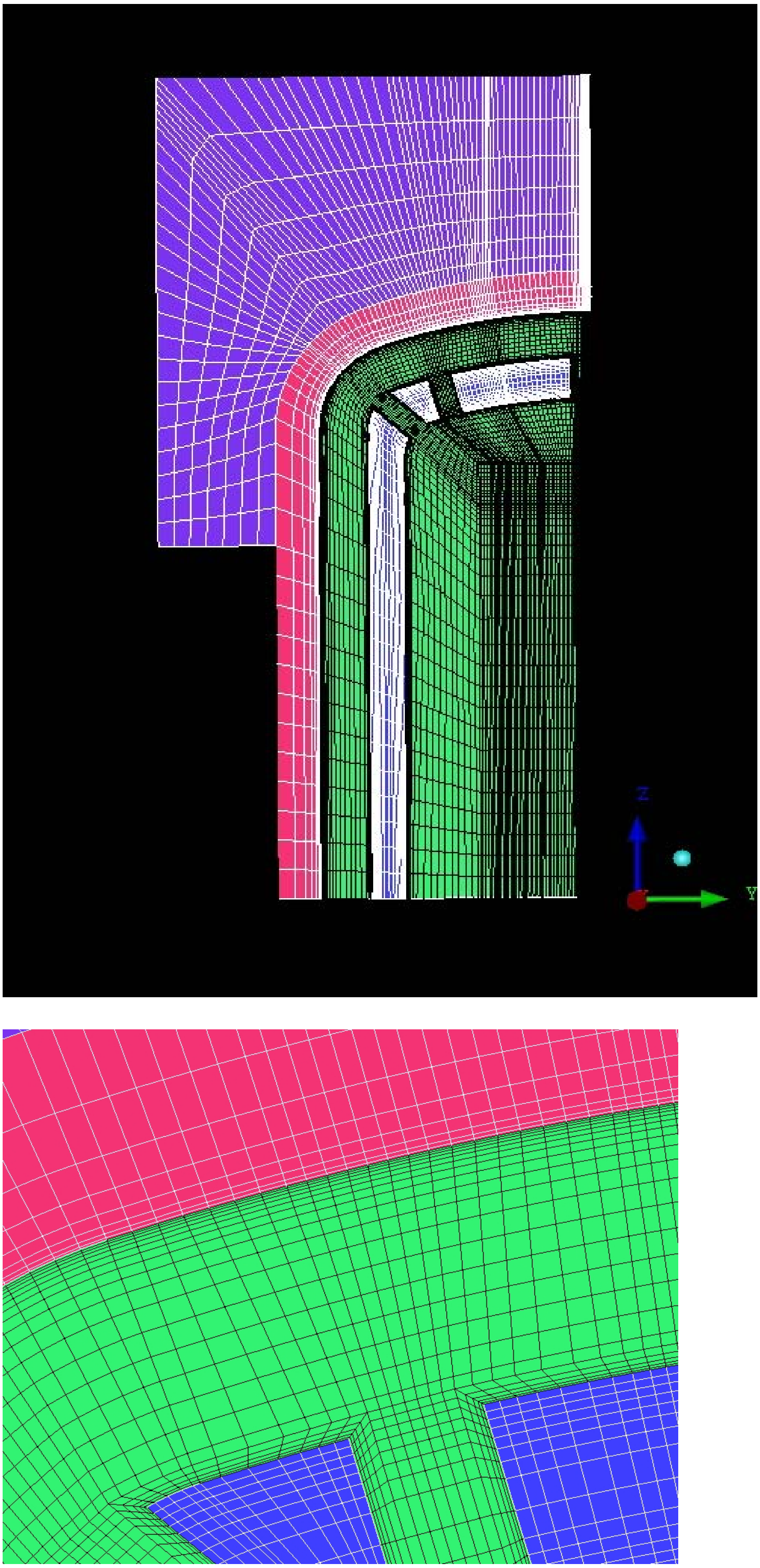

Fig. 12: Mesh made by ICEM 5 for the CFX case **“Coarse mesh”** and detail of the jet impingement region.

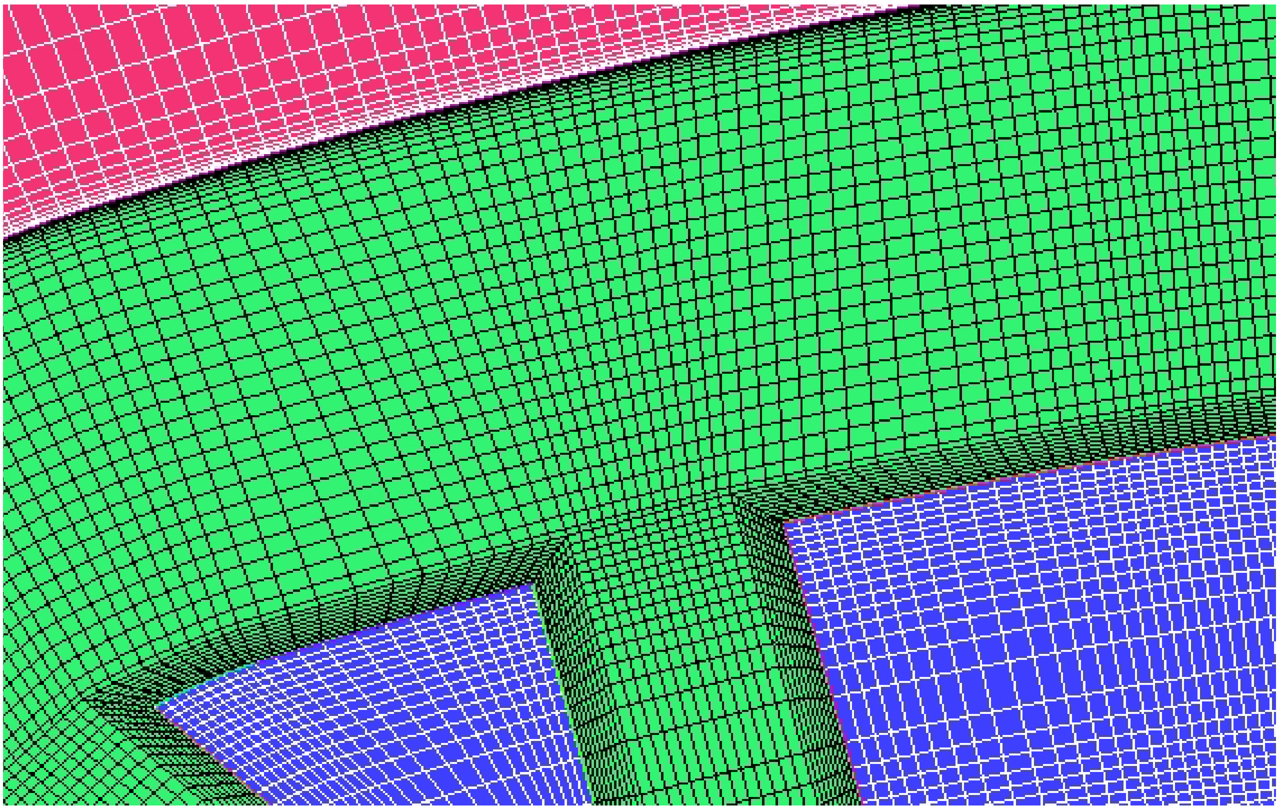

Fig. 13: Mesh made by ICEM 5 for the CFX case **“Medium mesh”,** detail of the jet impingement region.

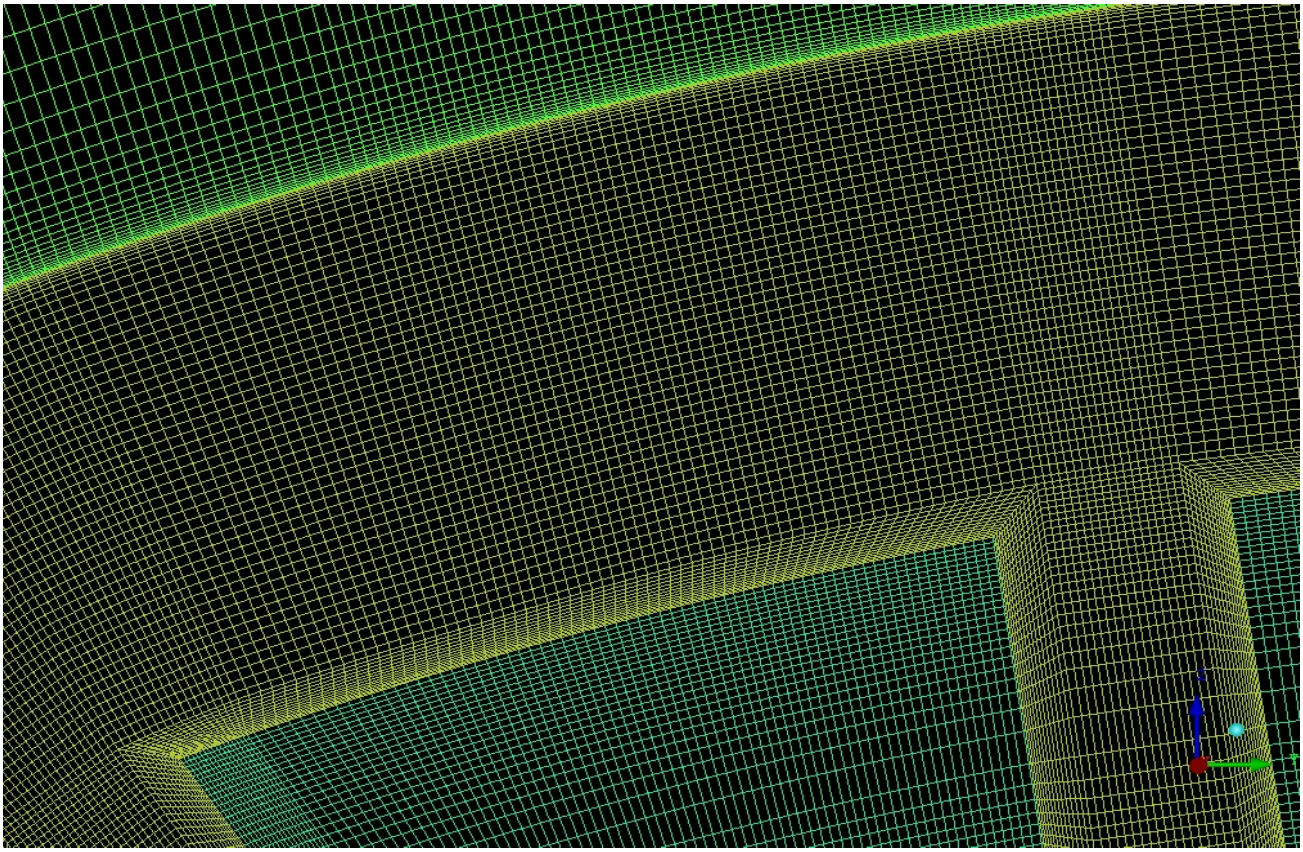

Fig. 14: Mesh made by ICEM 5 for the CFX case **“Fine mesh”,** detail of the jet impingement region.

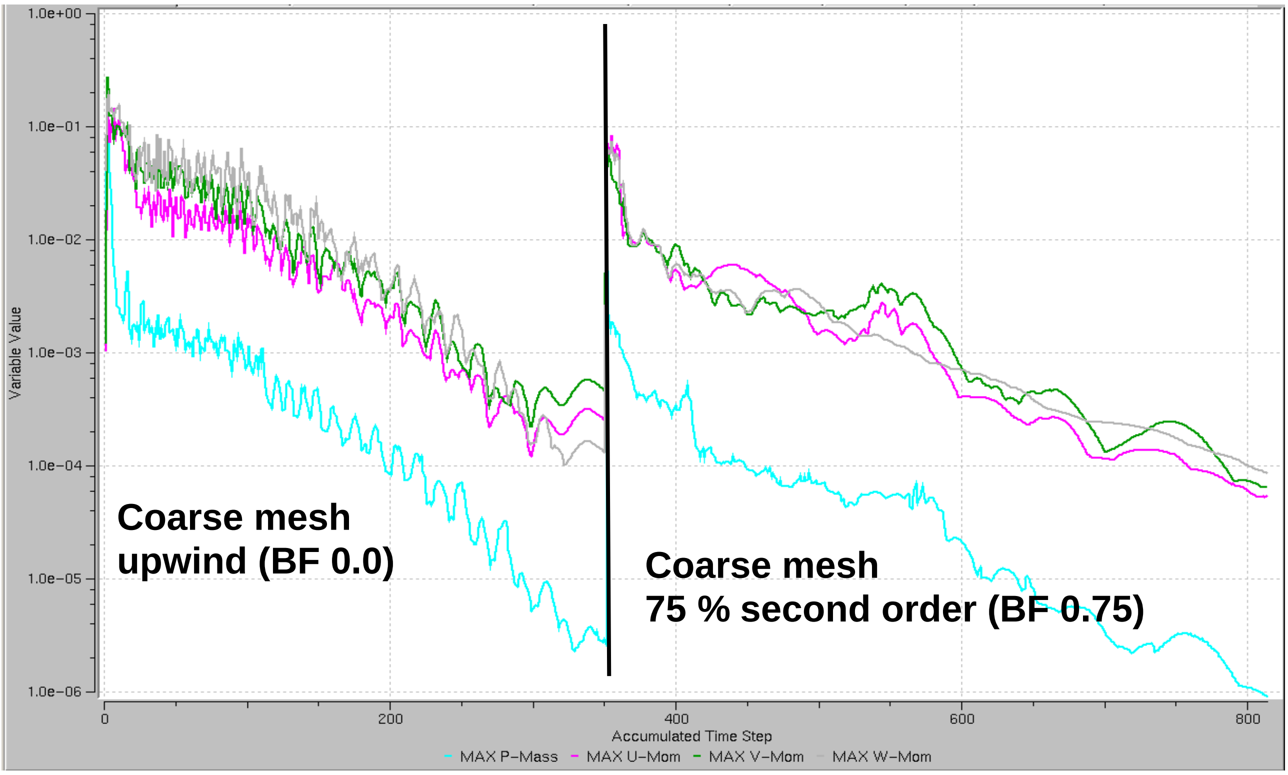

Fig. 15: Maximum residual (mass and impulse) over iteration steps, coarse mesh (BF = blending factor).

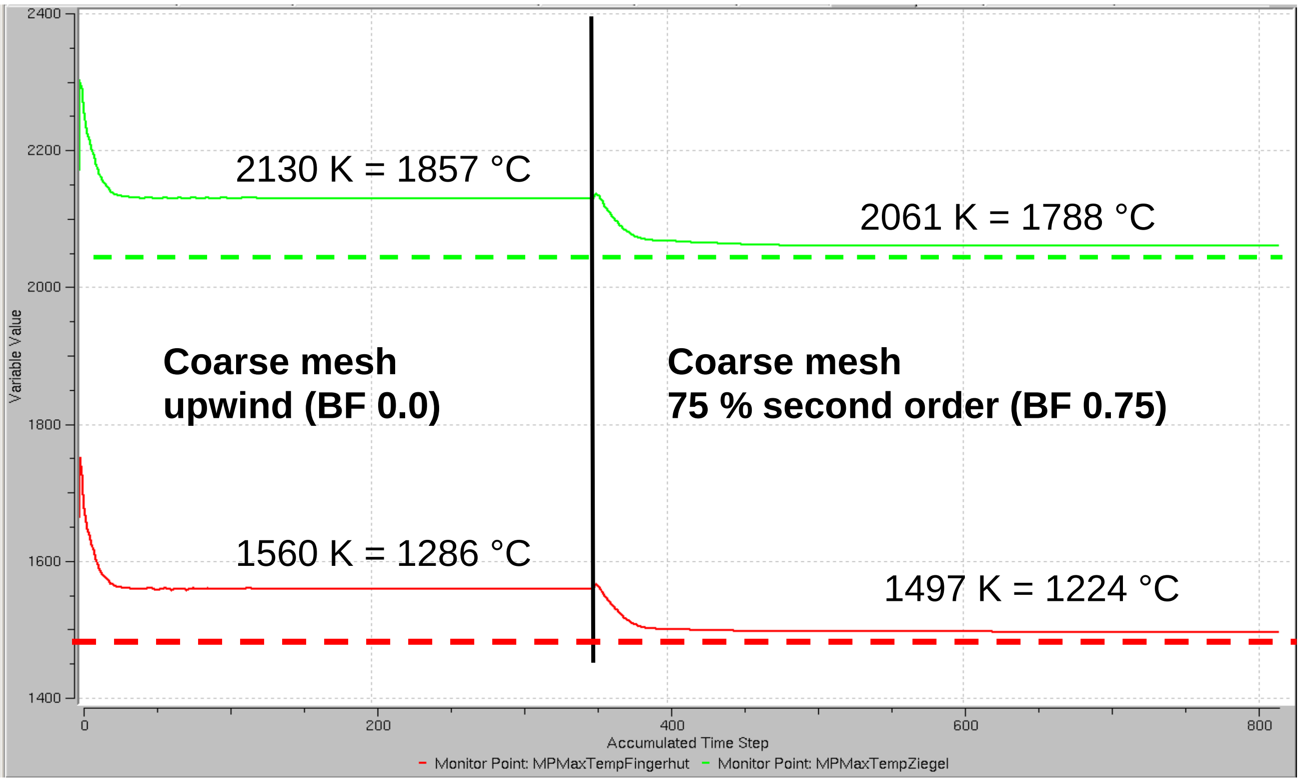

Fig. 16: Maximum temperatures of the tile and thimble over iteration steps, coarse mesh, (BF = blending factor).

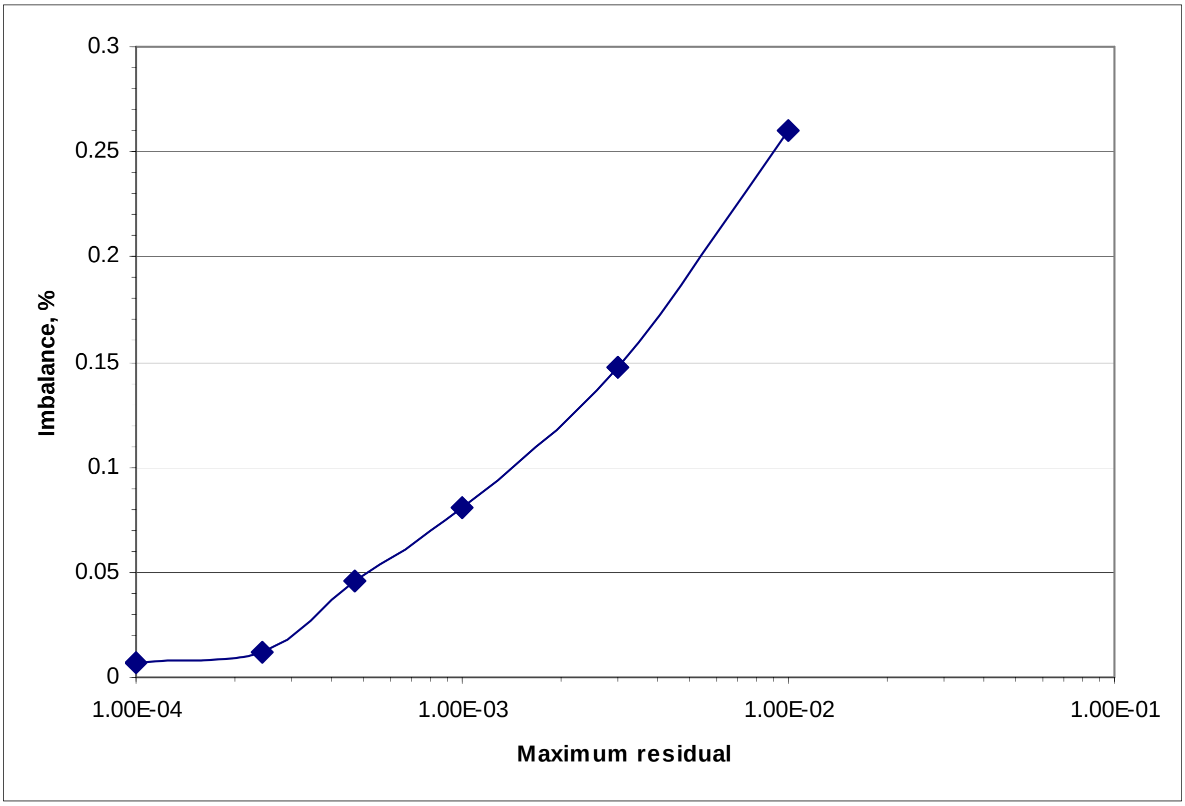

Fig. 17: Integral balances over the maximum residual, coarse mesh, blending factor 0.75.

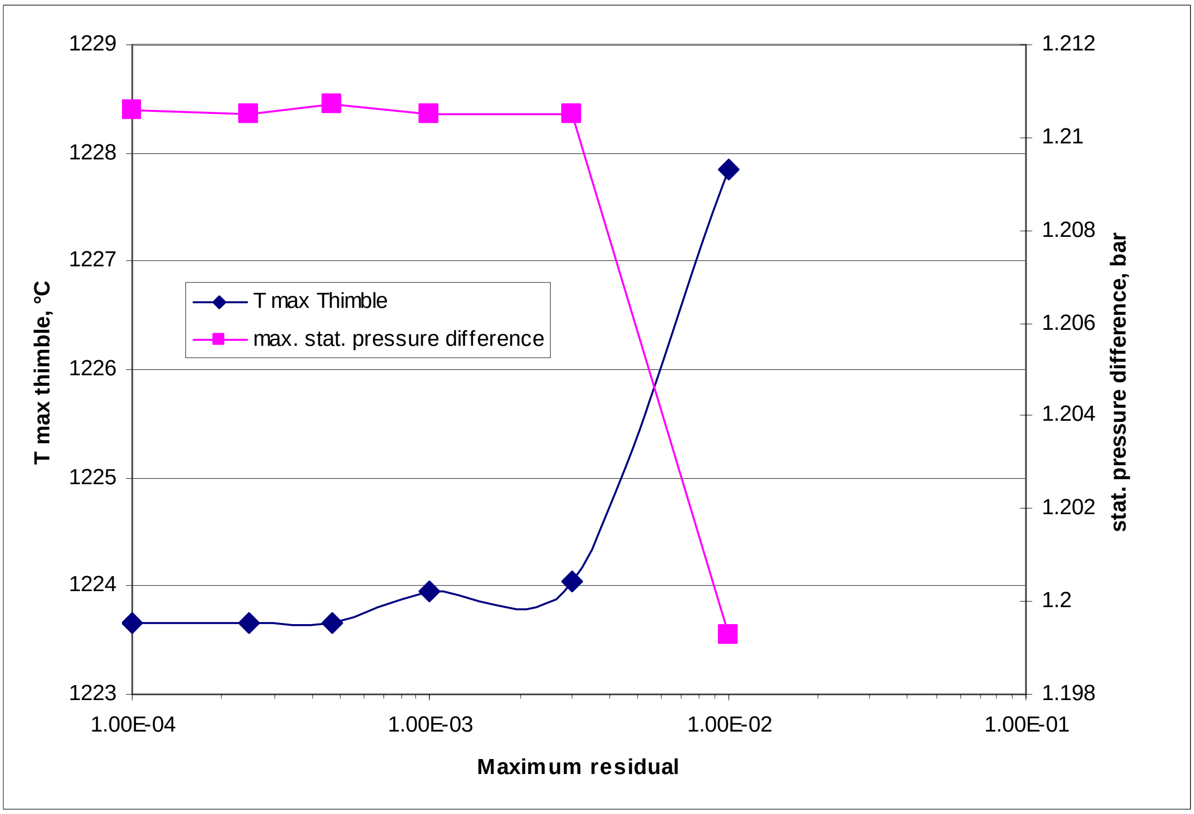

Fig. 18: Critical design parameters over the maximum residual, coarse mesh, blending factor 0.75.

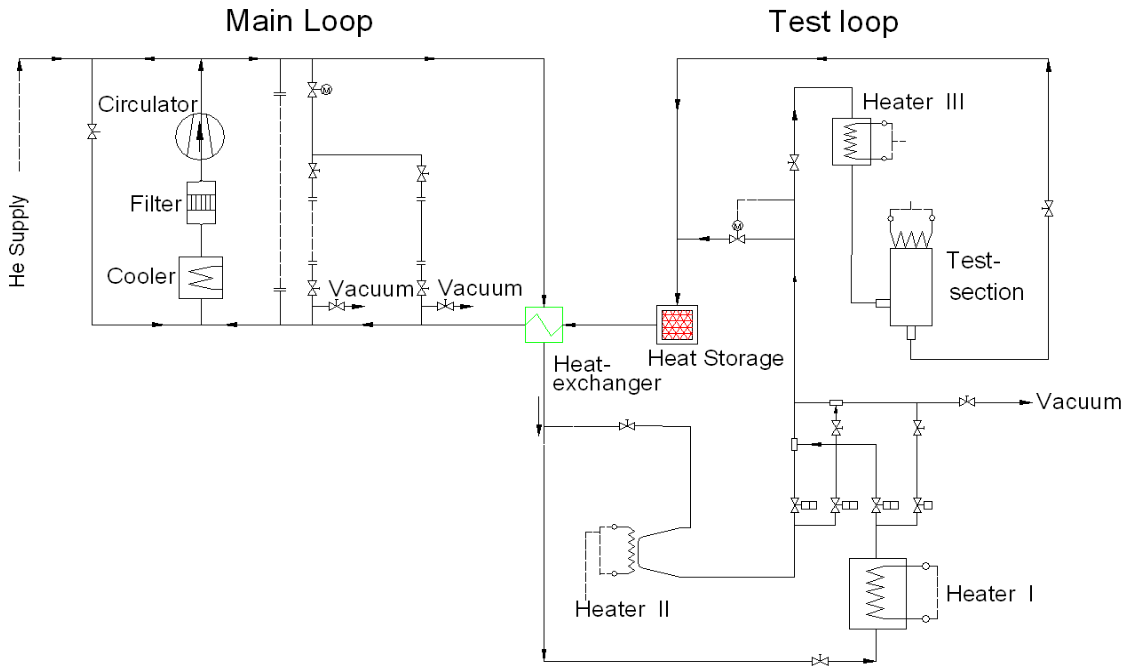

Fig. 19: Simplified schematic representation of HEBLO.

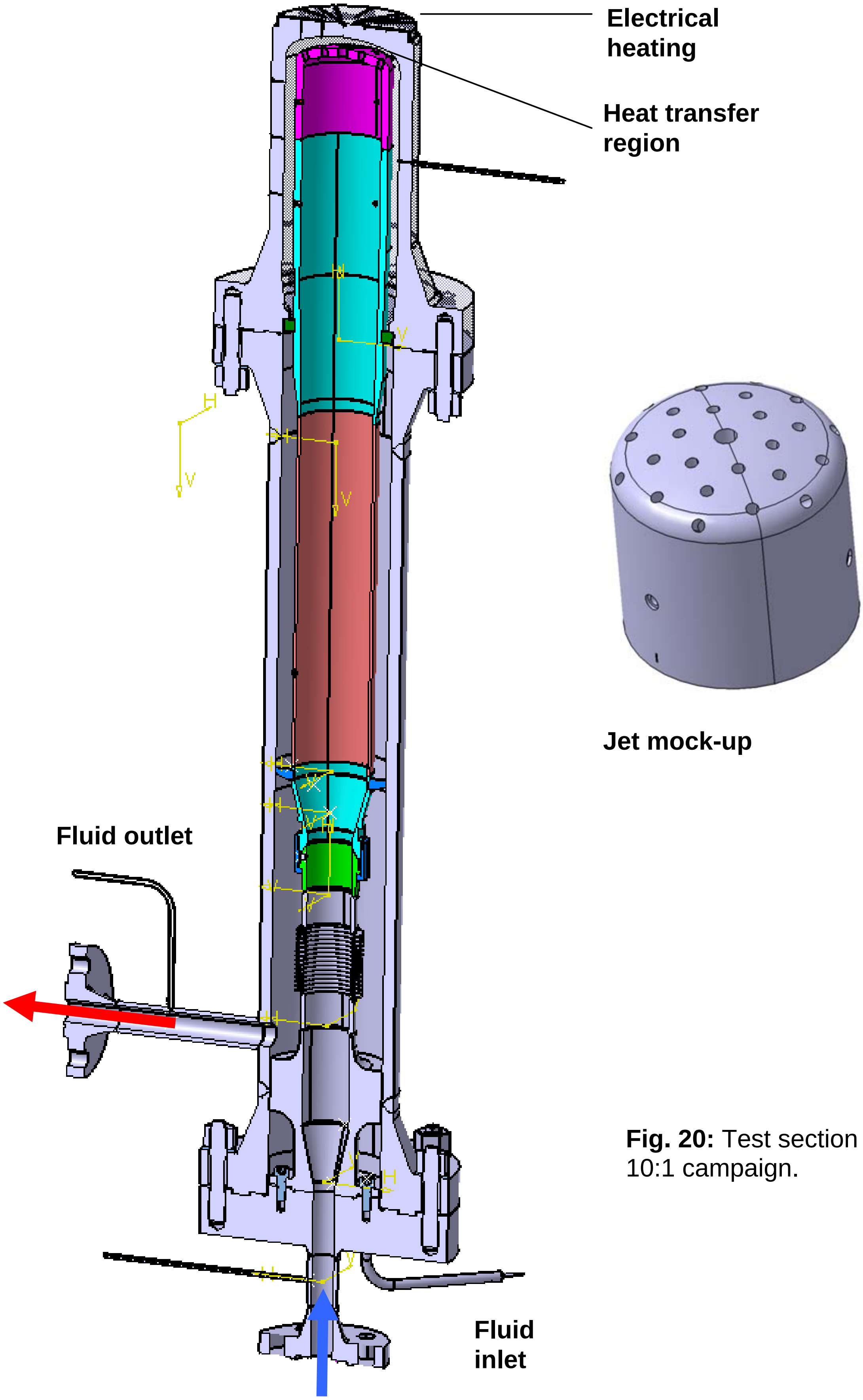

Fig. 20: Test section for the 10:1 campaign.

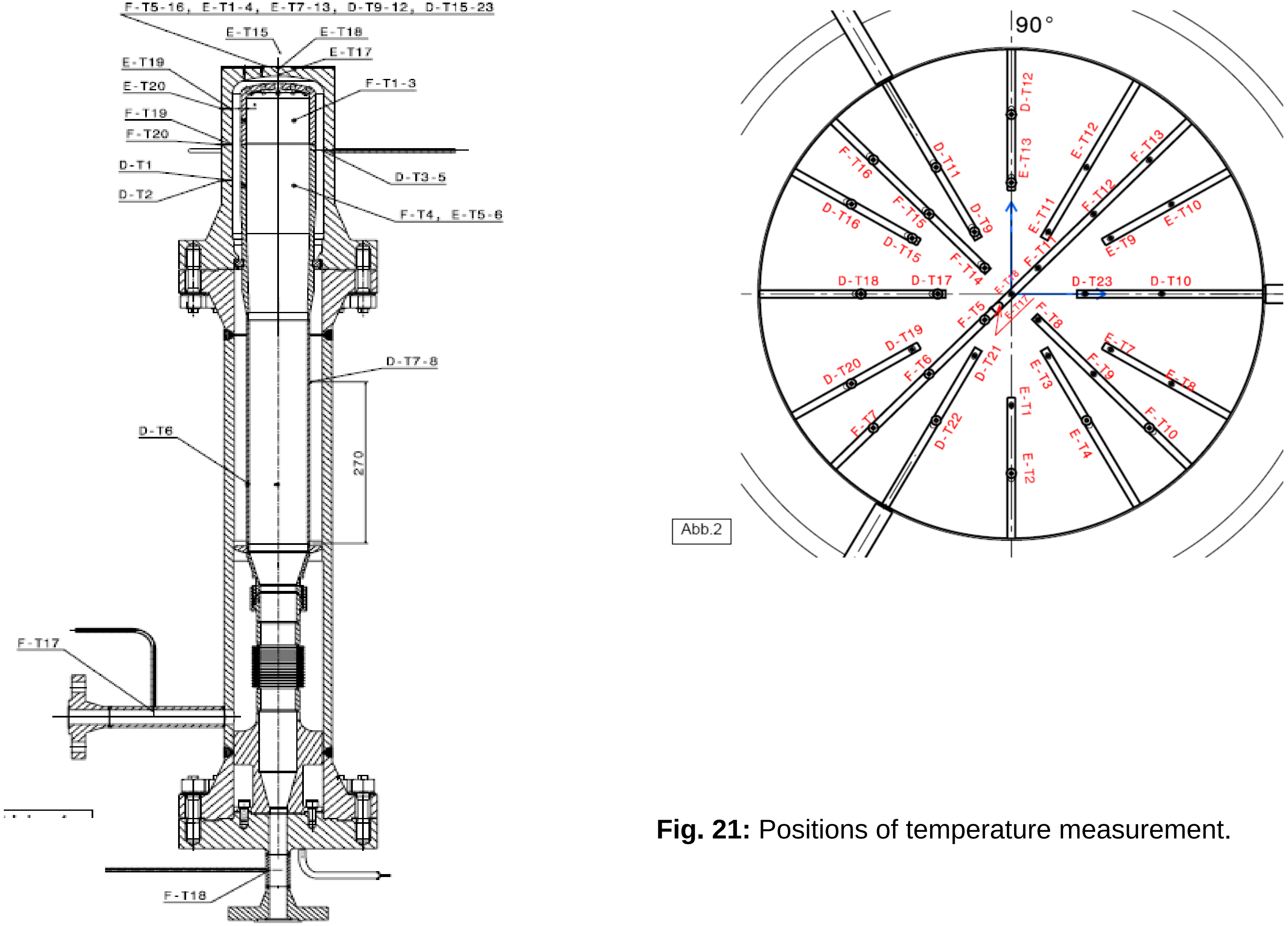

Fig. 21: Positions of temperature measurement.

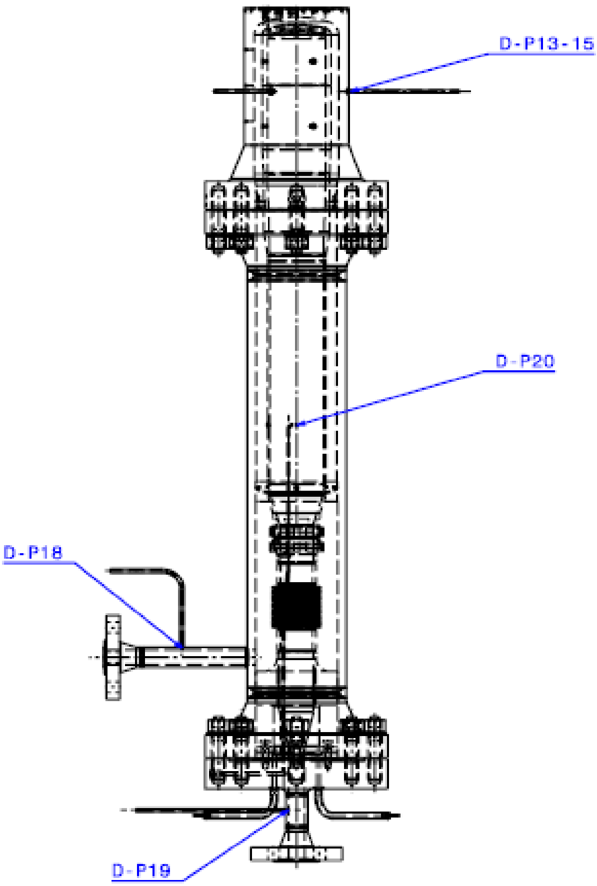

Fig. 22: Positions of pressure measurement.

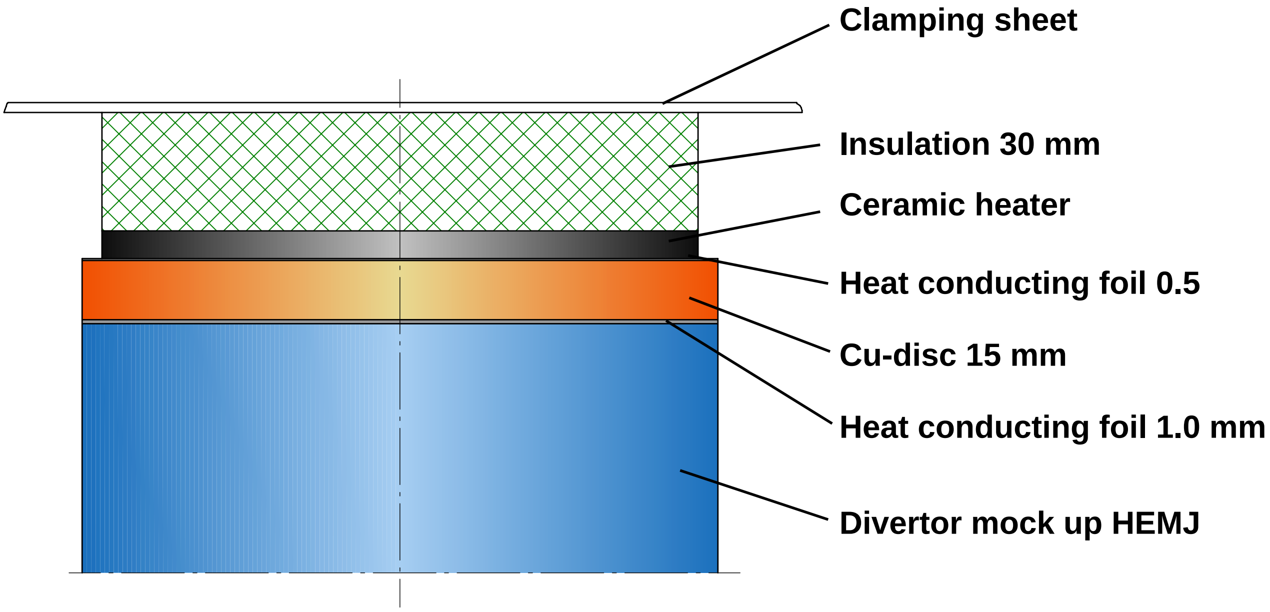

Fig. 23: Schematic representation of the arrangement of the electrical heater on top of the HEMJ model.

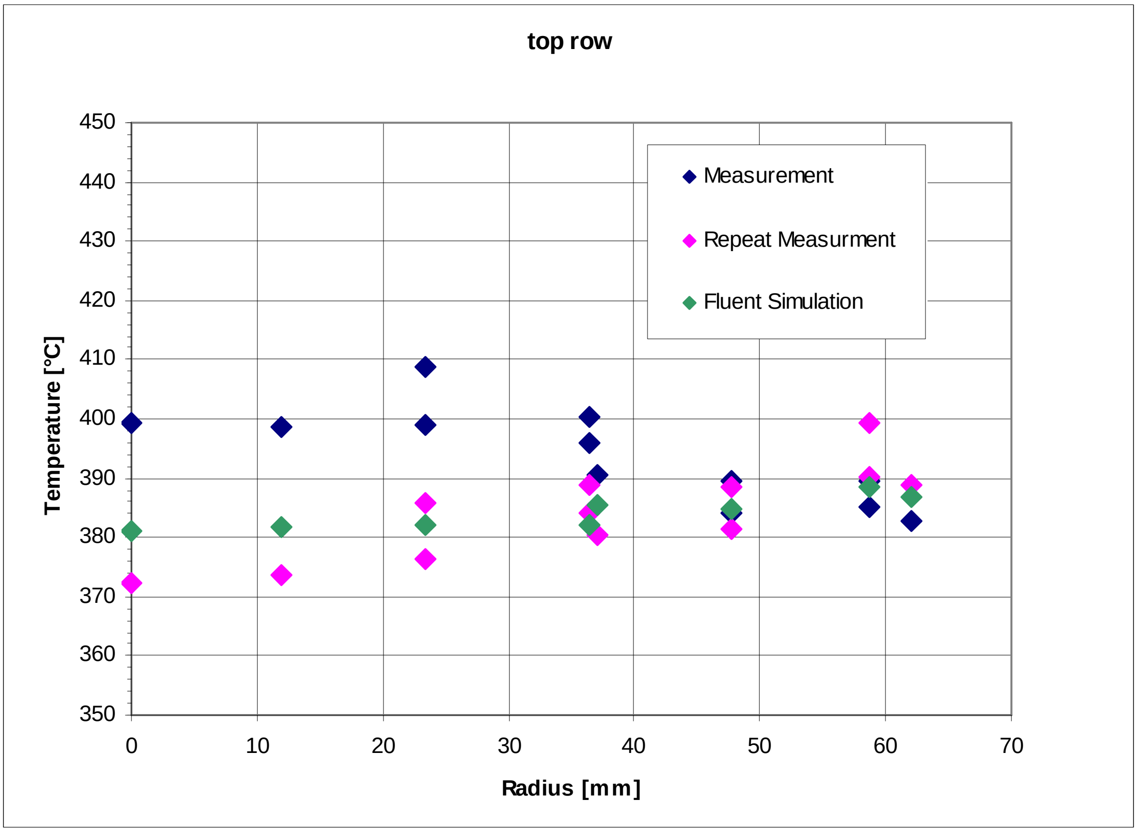

Fig. 24 a: Top row of thermocouples.

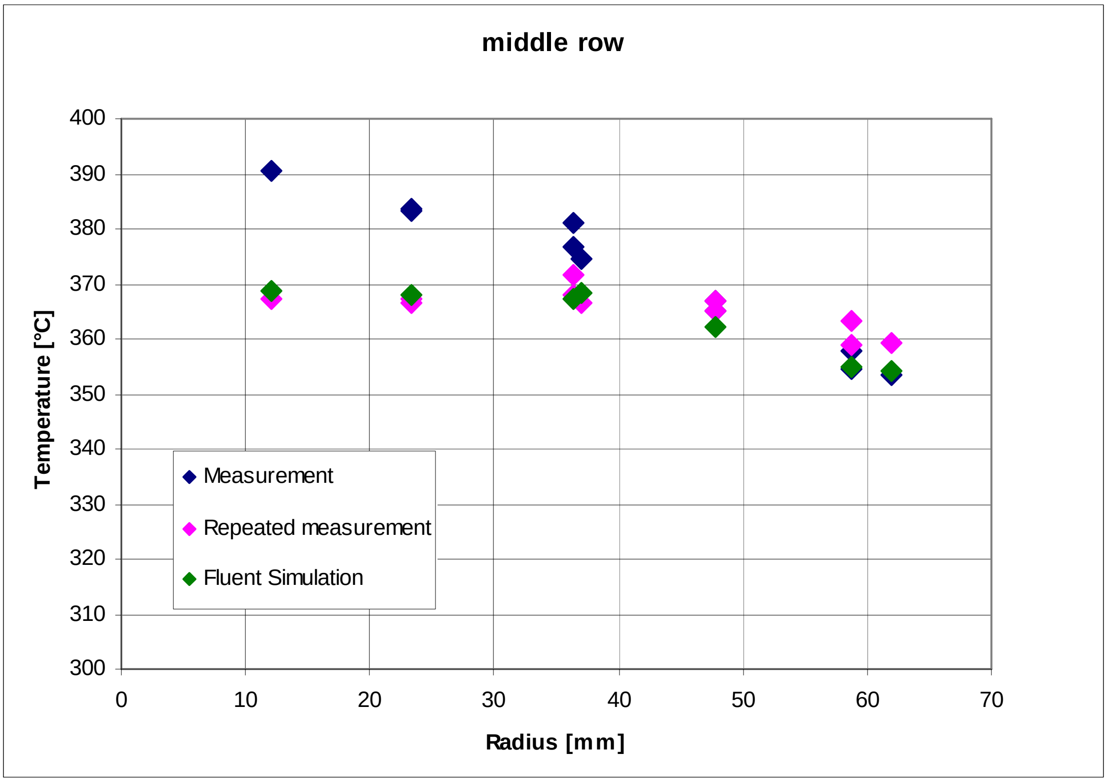

Fig. 24 b: Middle row of thermocouples.

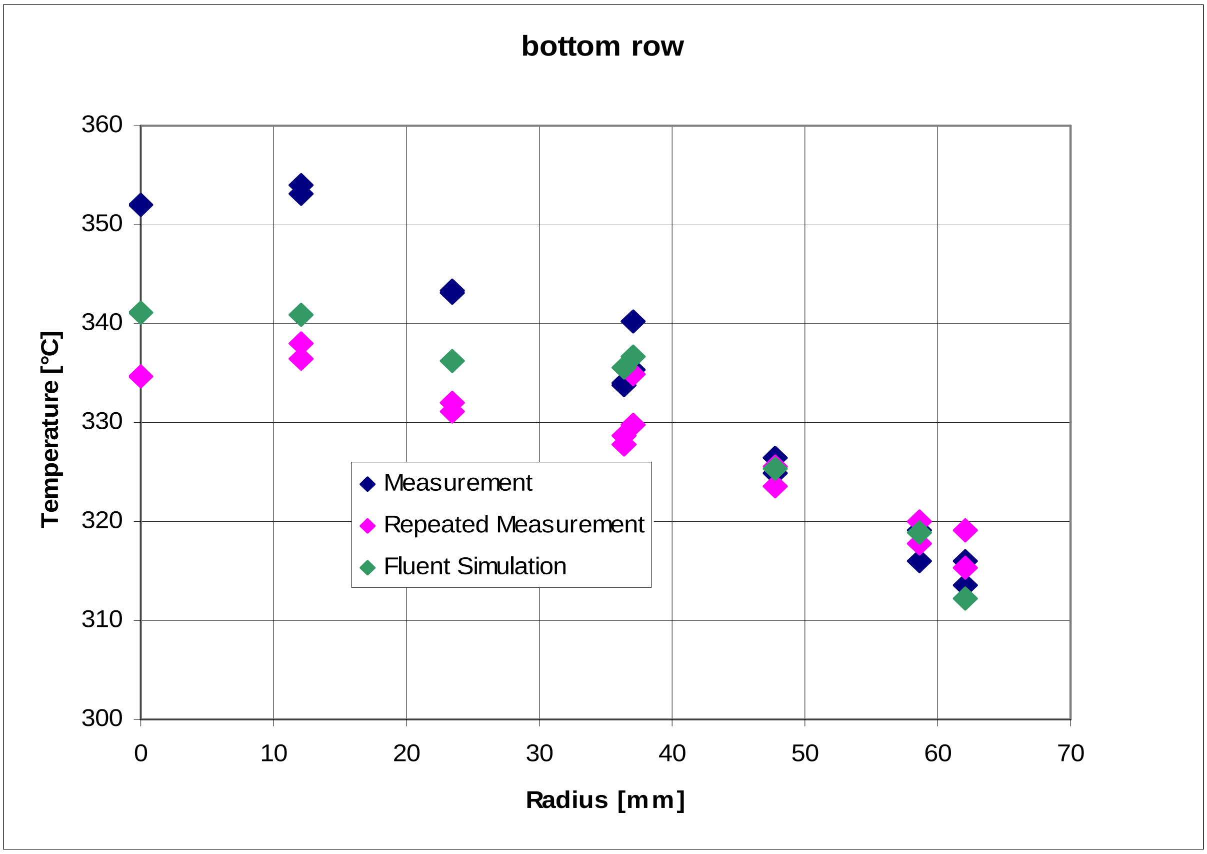

Fig. 24 c: Bottom row of thermocouples.

Fig. 24: Comparison of measured and simulated results for D250H1, 40 g/s.

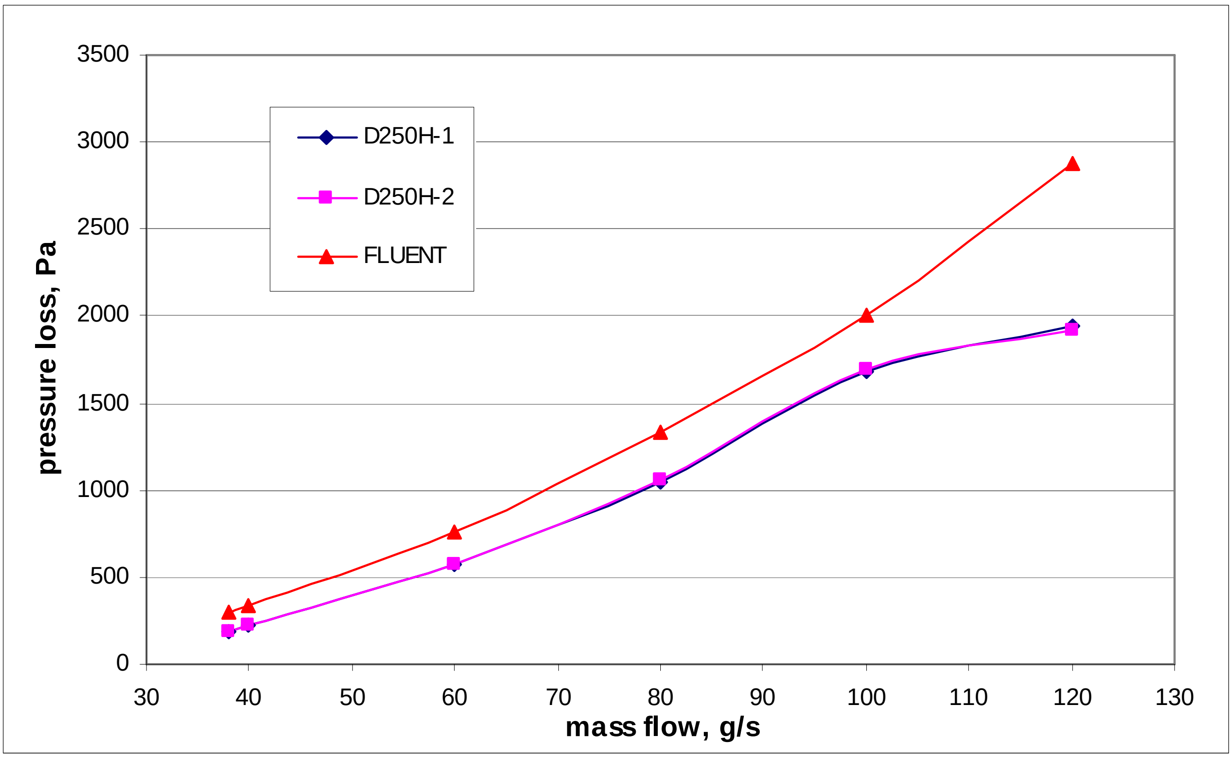

Fig. 25: Comparison of pressure losses, experimental and simulated results.

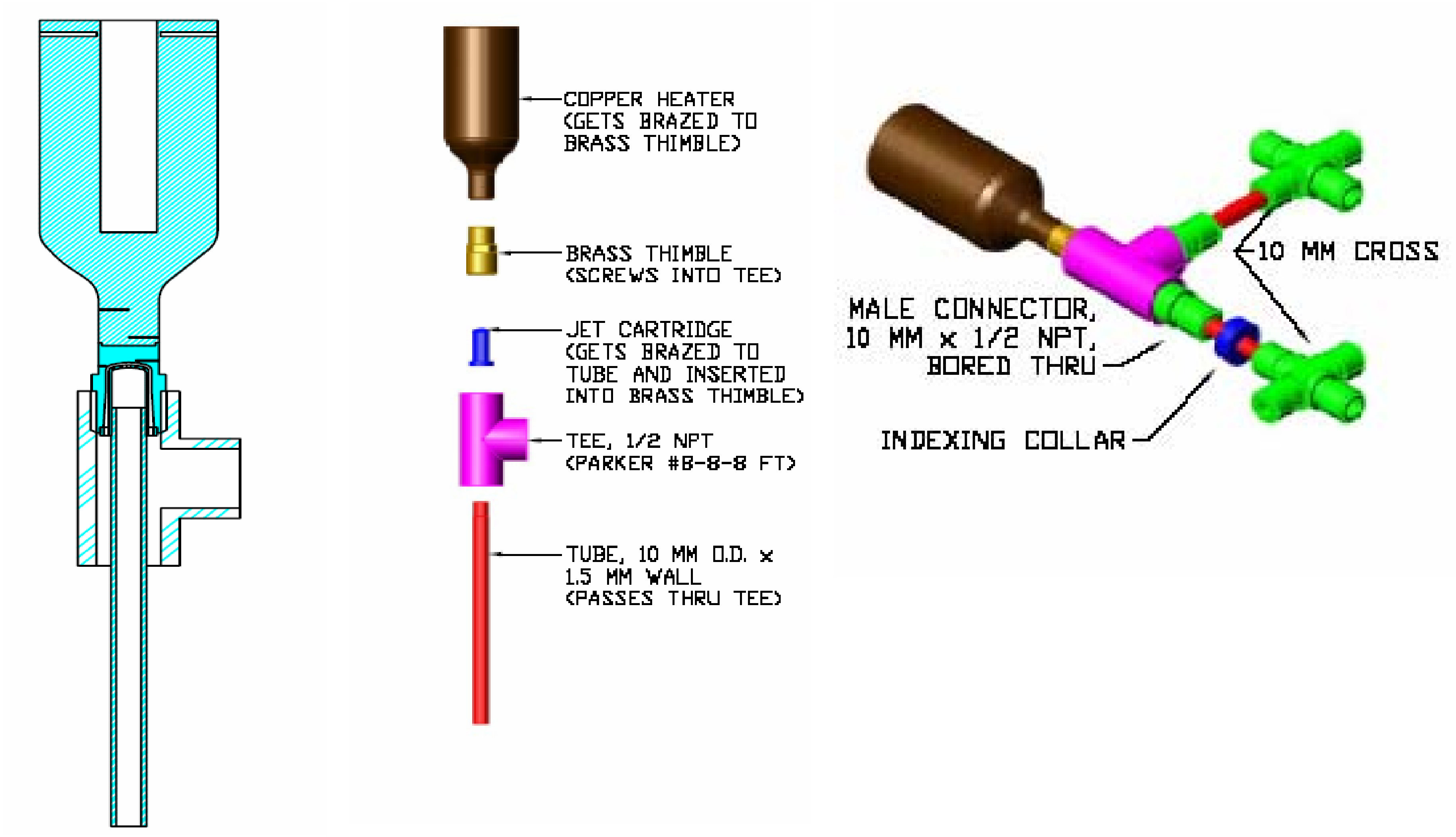

Fig. 26: Design sketch of the 1:1 mock-up (D. Sadowski, Georgia Tech).

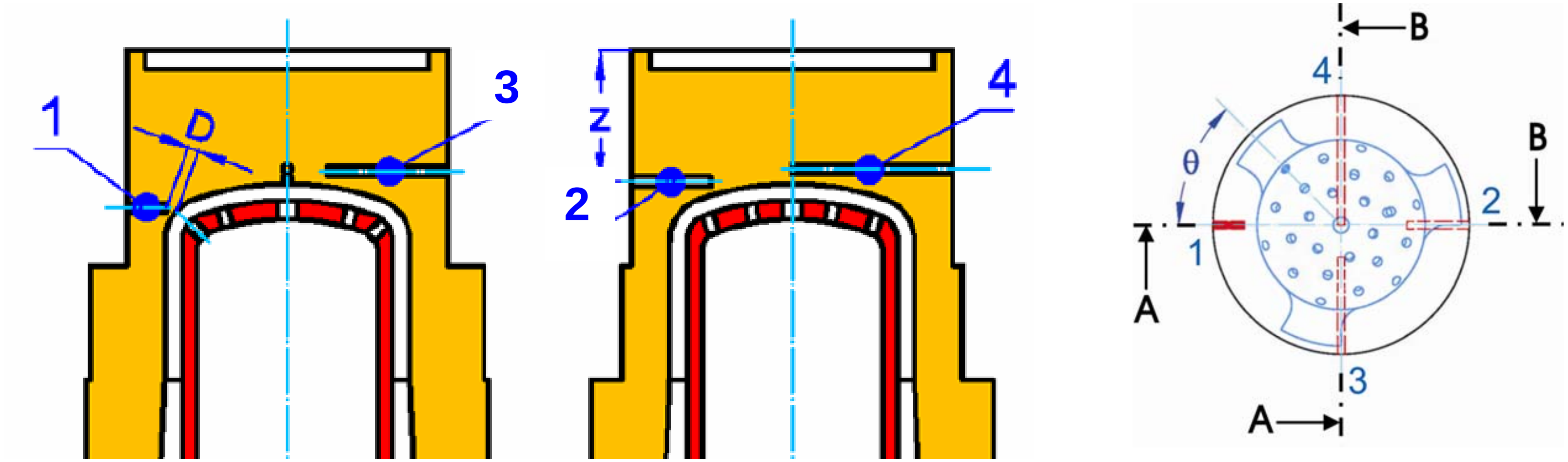

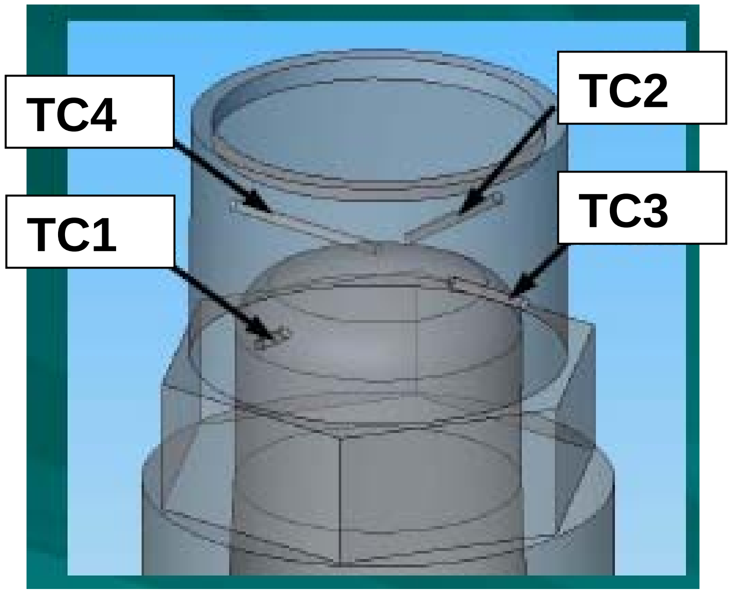

TC	R	z	D
#	[mm]	[mm]	[mm]
1	6.4	8.26	0.5
2	2.1	6.36	0.5
3	4.3	6.88	0.5
4	0.0	6.25	0.5

Fig. 27: Positions of the thermocouples TC 1 to TC 4 (D. Sadowski, L. Crosatti).

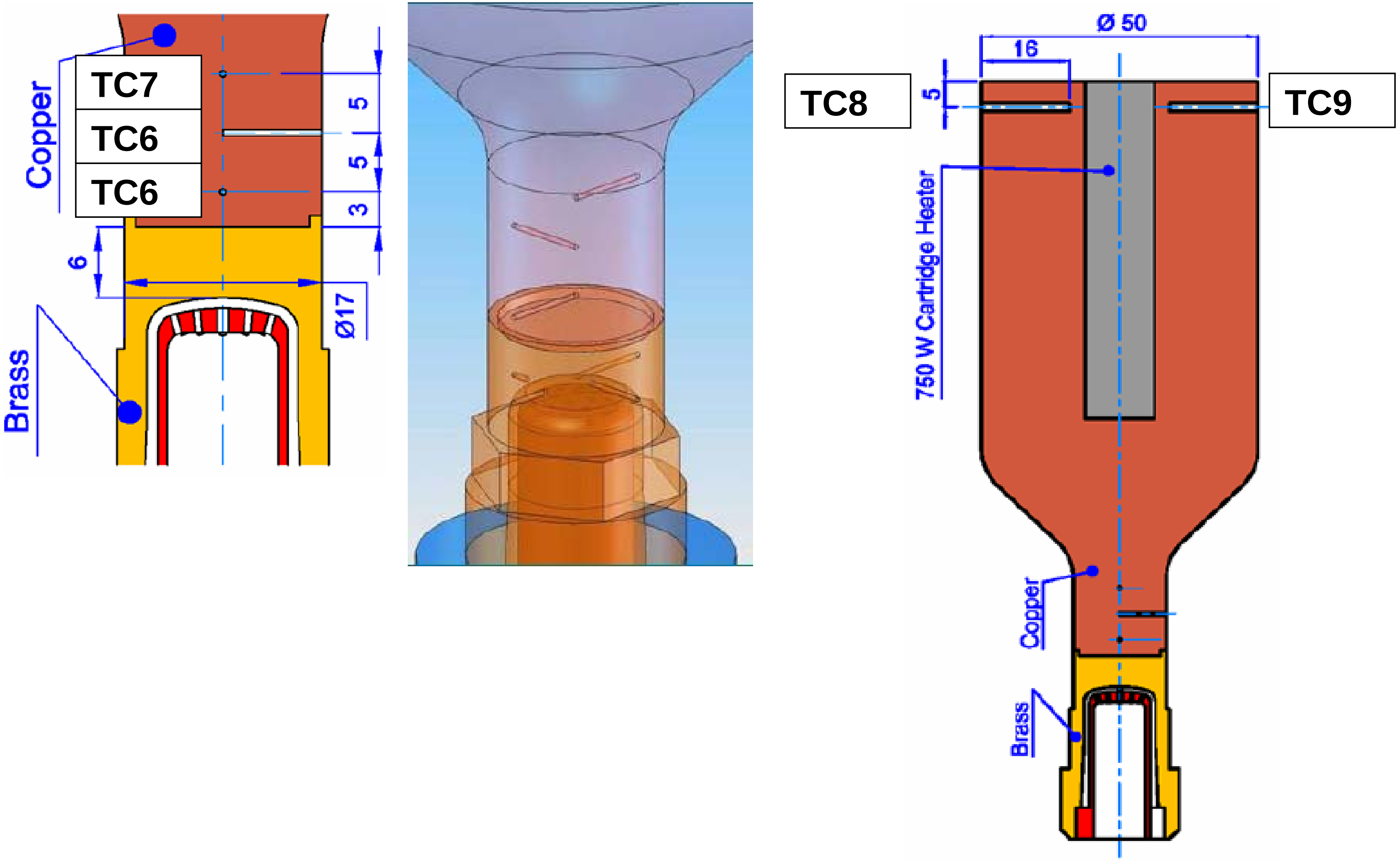

Fig. 28: Positions of the thermocouples TC 5 to TC 9 (D. Sadowski, L. Crosatti).

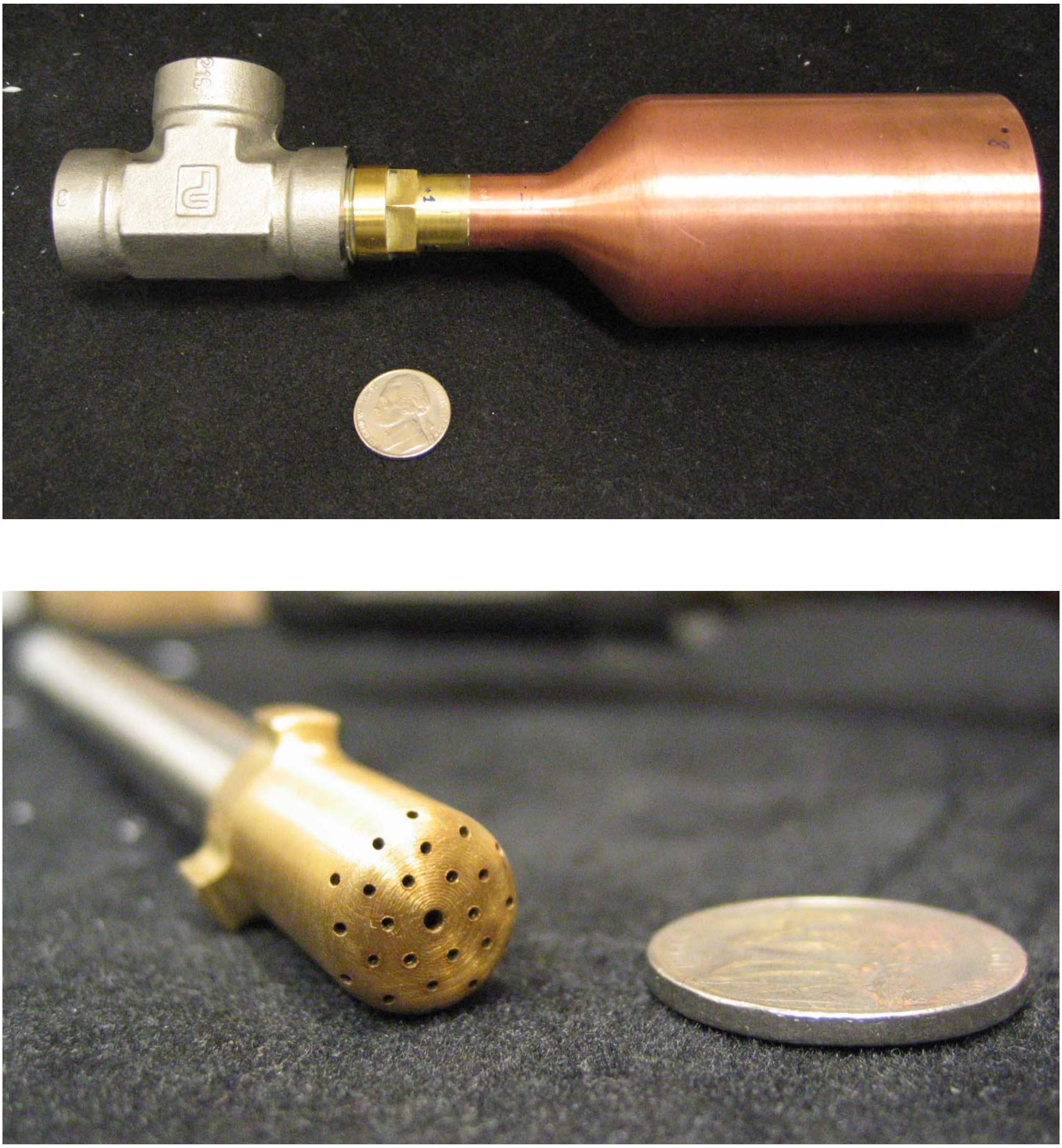

Fig. 29: Photographs of the mock-up and the cartridge (by L. Crosatti).

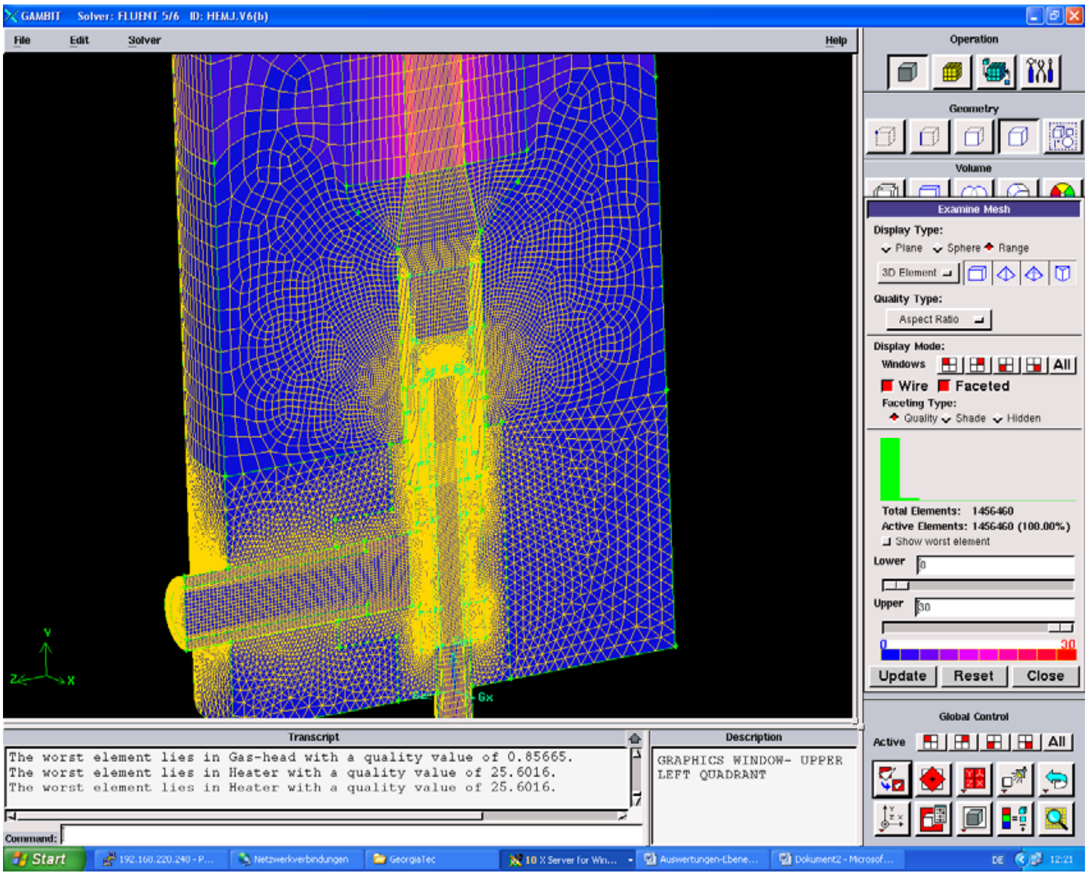

Display Type: Plane Sphere Range

3D Element

Quality Type: Aspect Ratio

Display Mode: Windows All

Wire Faceted

Faceting Type: Quality Shade Hidden

Total Elements: 1456460

Active Elements: 1456460 (100.00%)

Show worst element

Lower 0

Upper 30

Transcript

```
The worst element lies in Gas-head with a quality value of 0.85665.
The worst element lies in Heater with a quality value of 25.6016.
The worst element lies in Heater with a quality value of 25.6016.
```

Description

```
GRAPHICS WINDOW- UPPER
LEFT QUADRANT
```

Command:

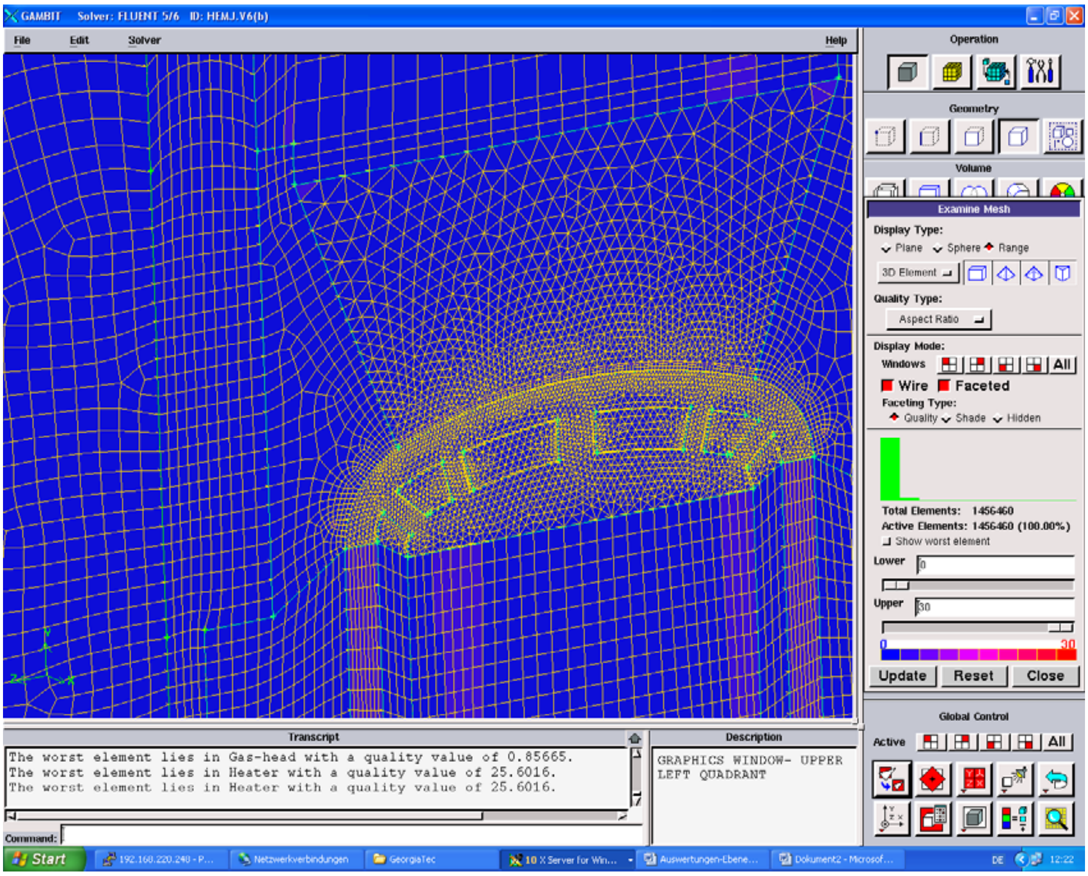

Display Type: Plane Sphere Range

3D Element

Quality Type: Aspect Ratio

Display Mode: Windows All

Wire Faceted

Faceting Type: Quality Shade Hidden

Total Elements: 1456460

Active Elements: 1456460 (100.00%)

Show worst element

Lower 0

Upper 30

Transcript

The worst element lies in Gas-head with a quality value of 0.85665.
The worst element lies in Heater with a quality value of 25.6016.
The worst element lies in Heater with a quality value of 25.6016.

Description

GRAPHICS WINDOW- UPPER
LEFT QUADRANT

Command:

Fig. 30: Mesh V6 for thermohydraulic simulations (detail near the heat transfer surface).

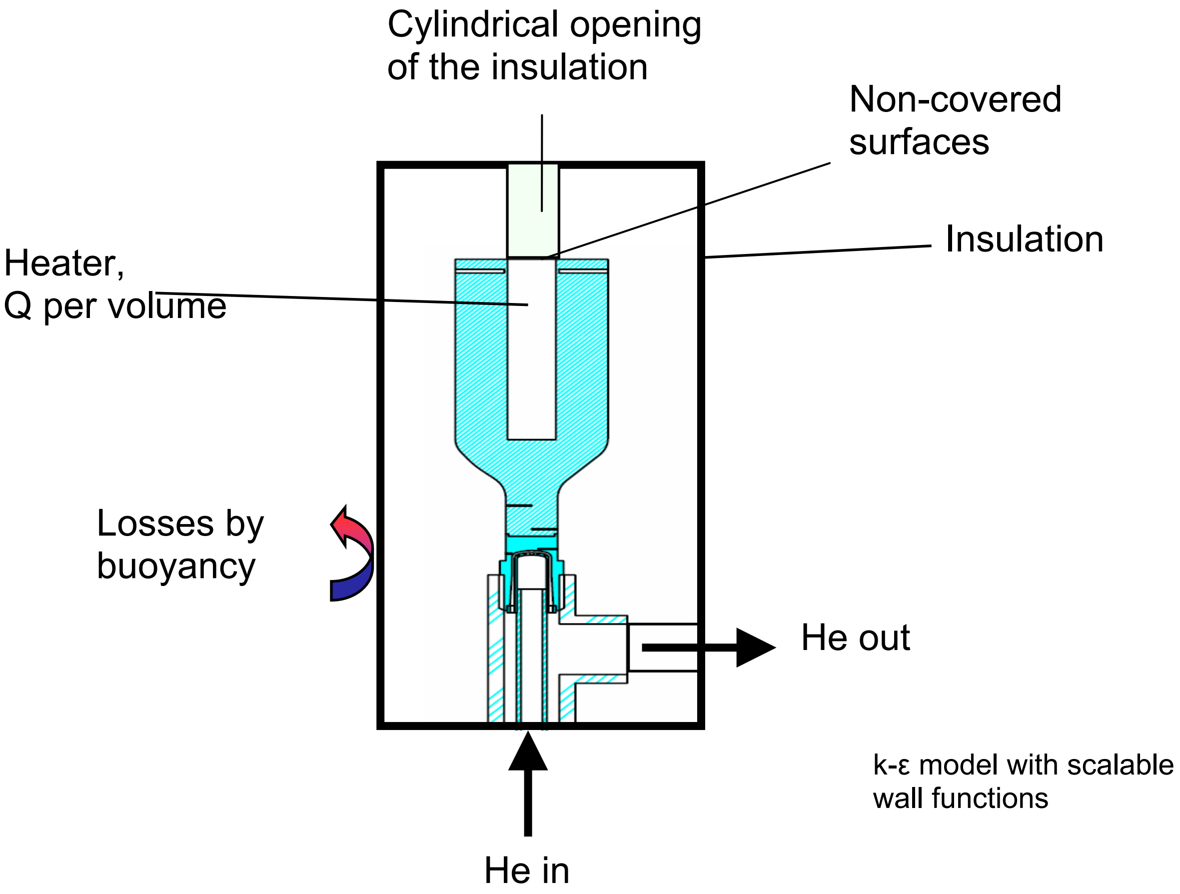

Fig. 31: Simulation model.

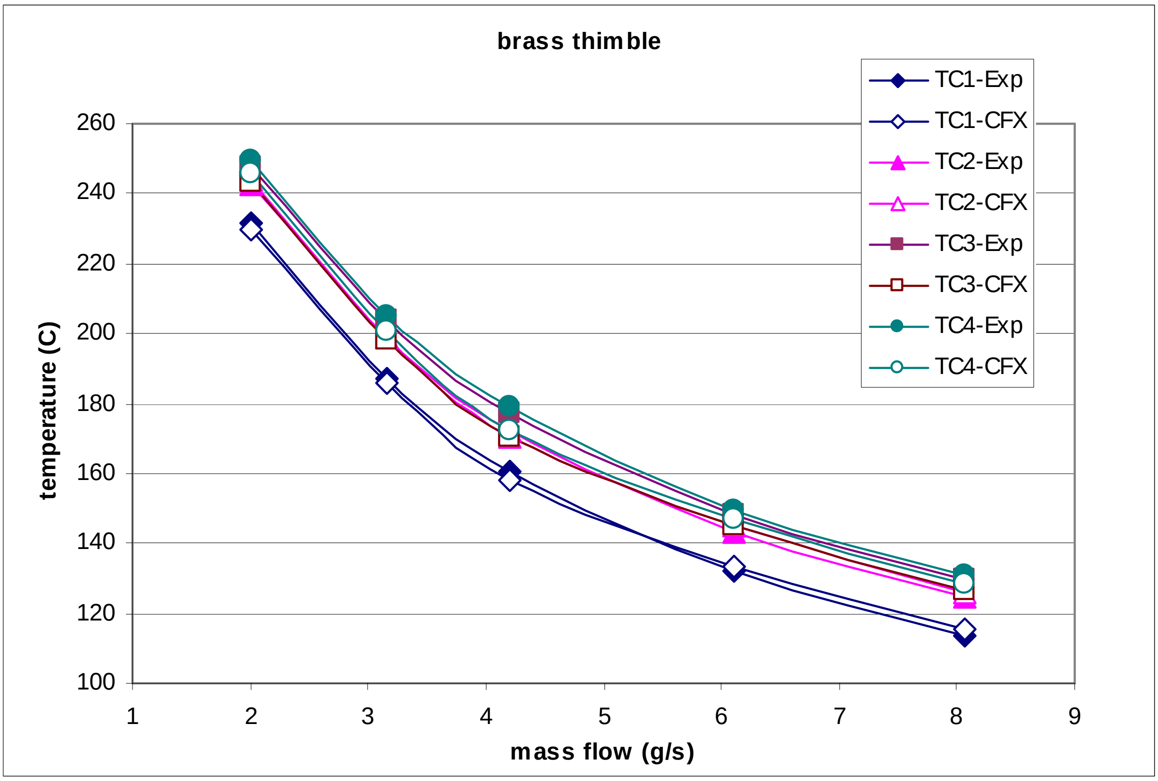

Fig. 32 a) for the brass thimble (TC1 to TC4)

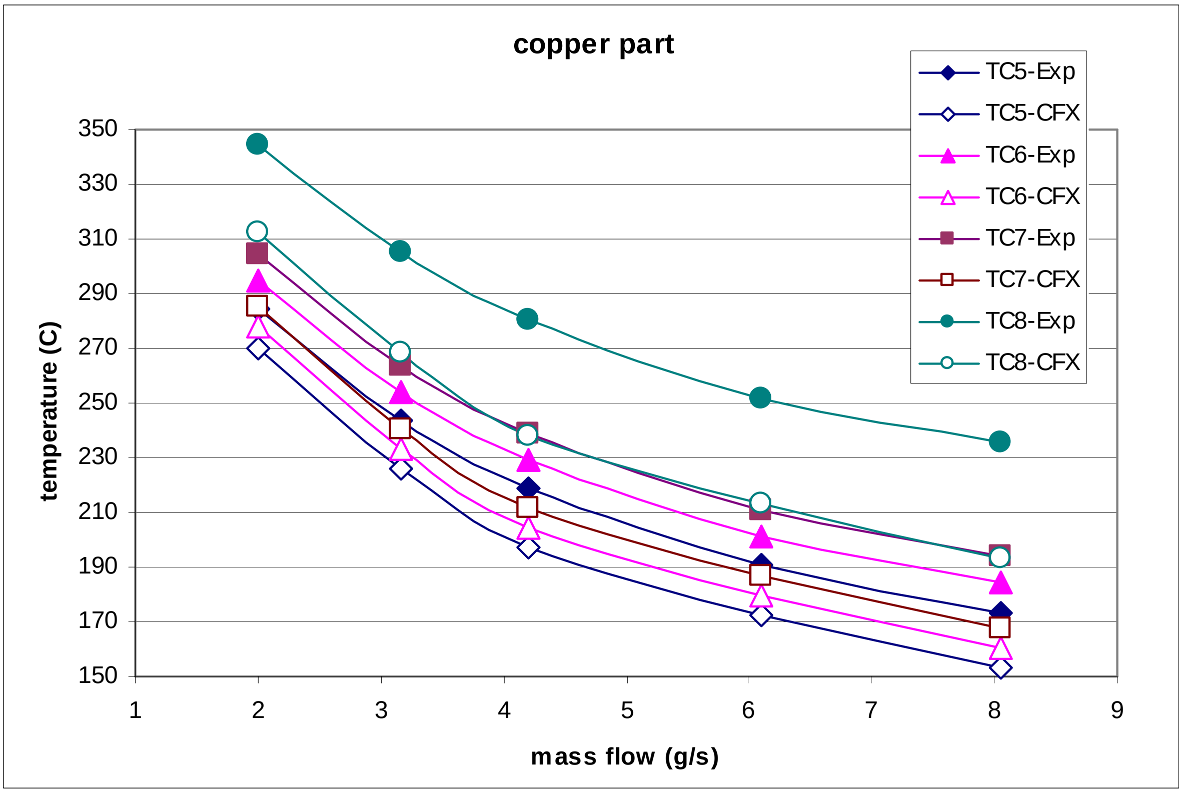

Fig. 32 b) for the copper part (TC5 to TC8)

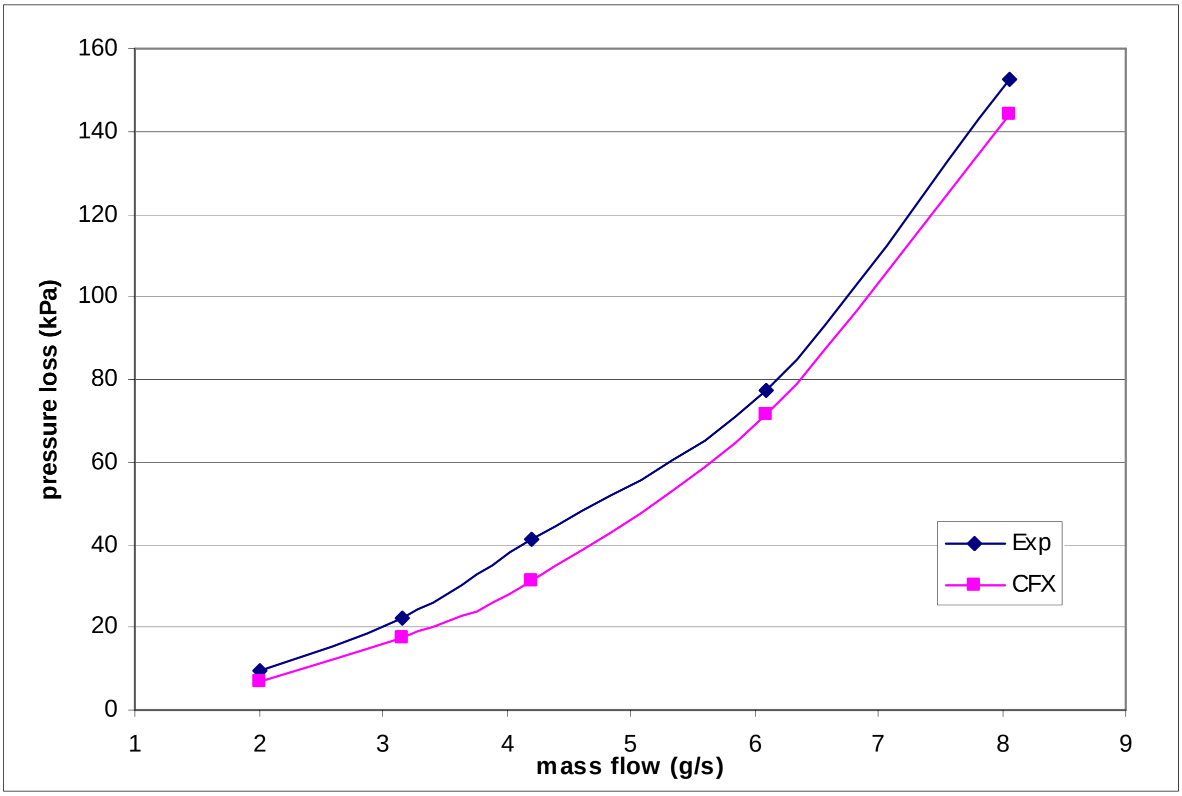

Fig. 32 c) for the pressure loss

Fig. 32: Comparison of experimental and simulated temperature and pressure loss results for the air tests.

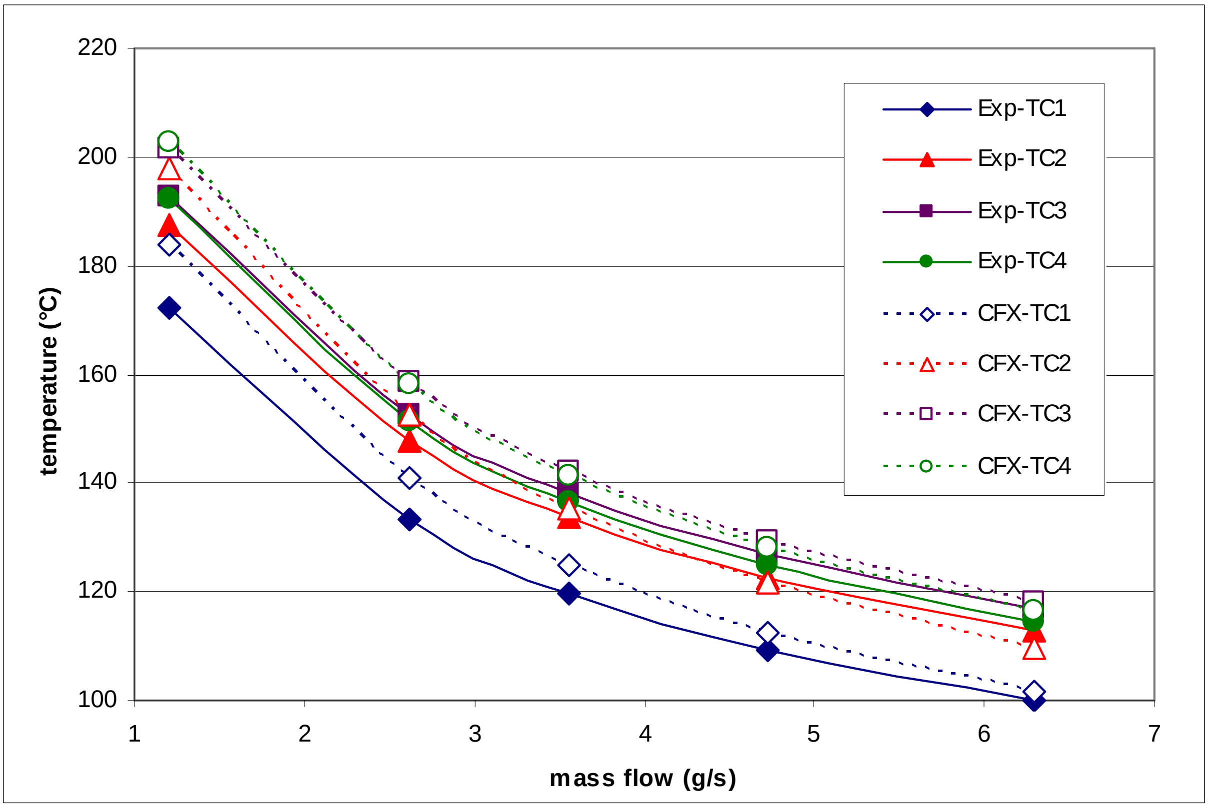

Fig. 33 a) TC1 to TC4 in brass thimble

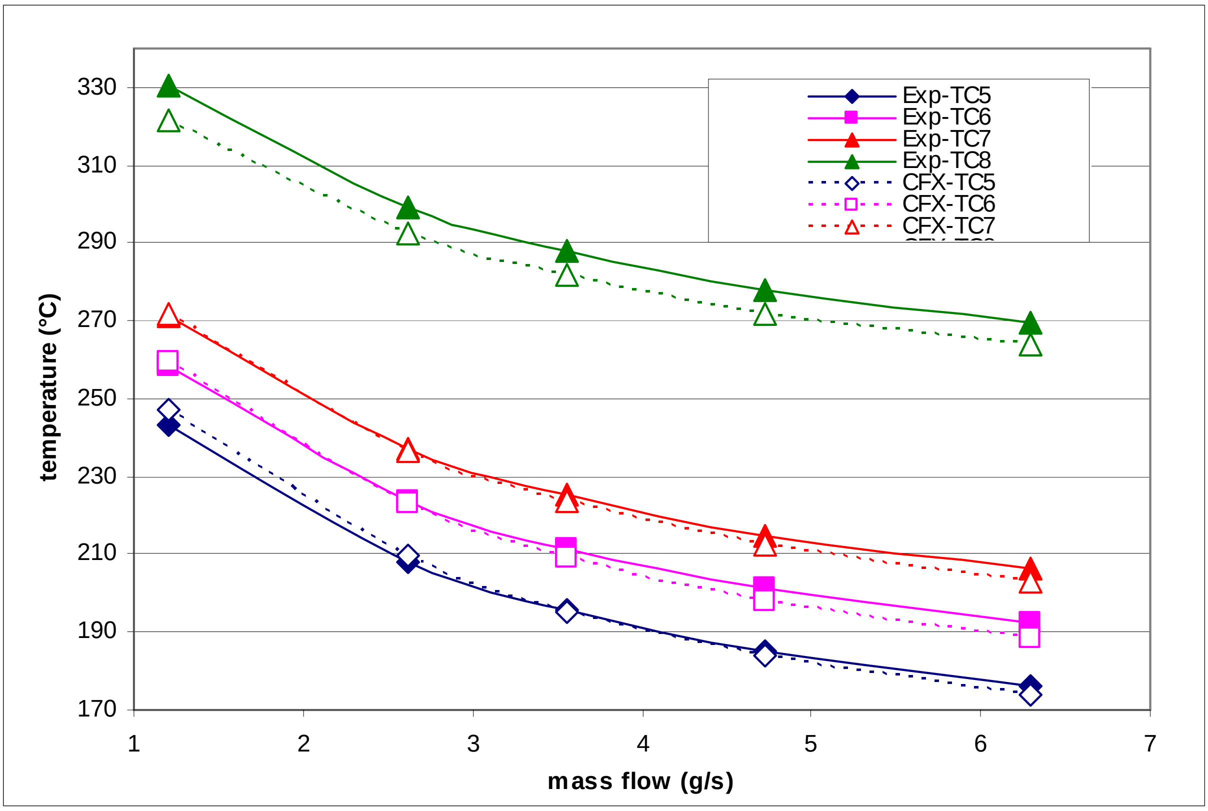

Fig. 33 b) TC 5 to TC 9 in copper part

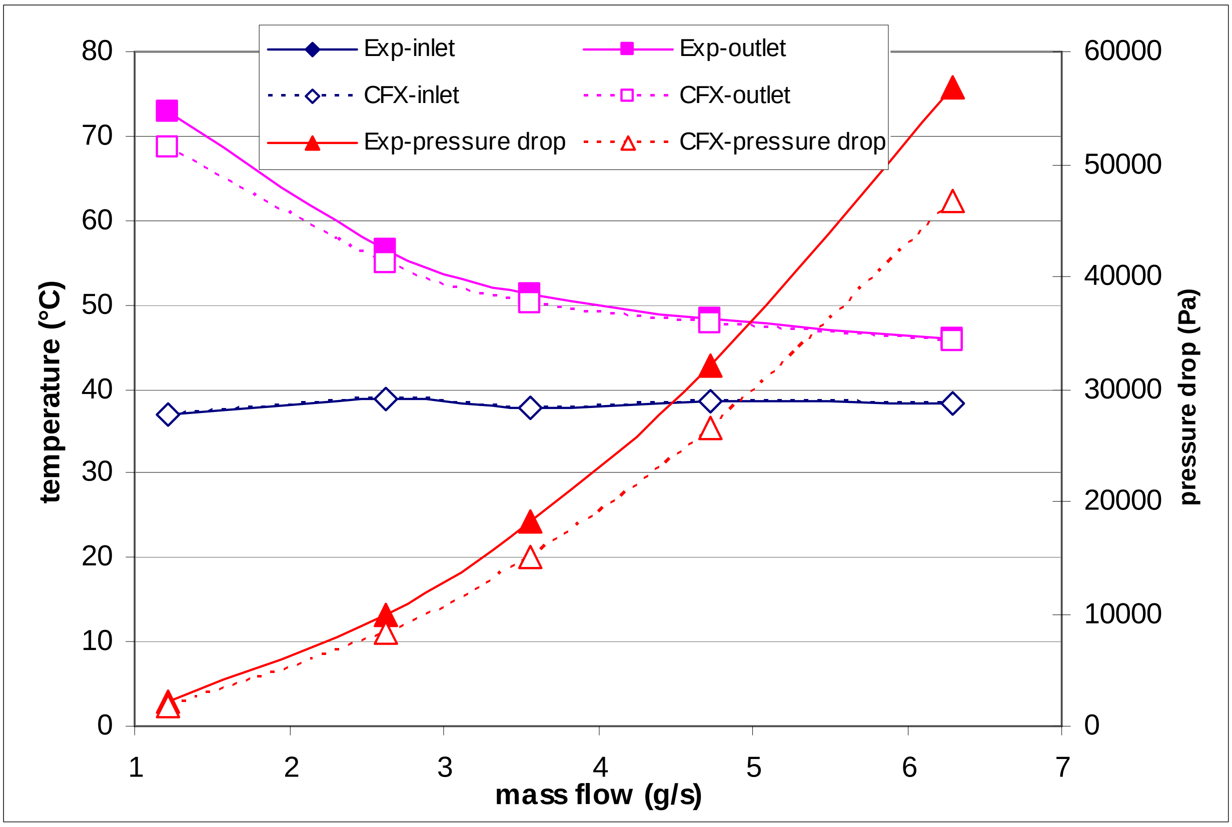

Fig. 33 c) Inlet, outlet and pressure loss.

Fig. 33: Comparison of measured and simulated temperatures and pressure losses (mesh V6mod, second test series) in the different parts of the mock-up for the case of 227 W.

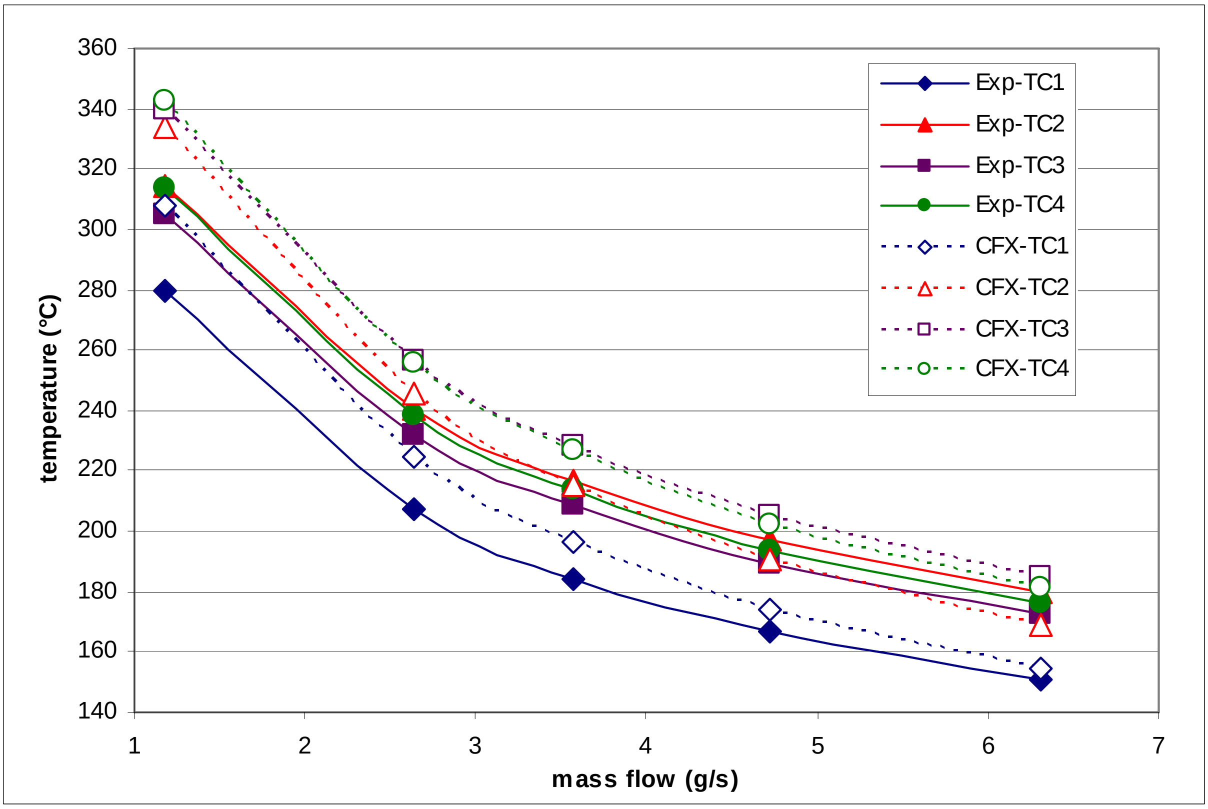

Fig. 34 a) TC 1 to TC 4

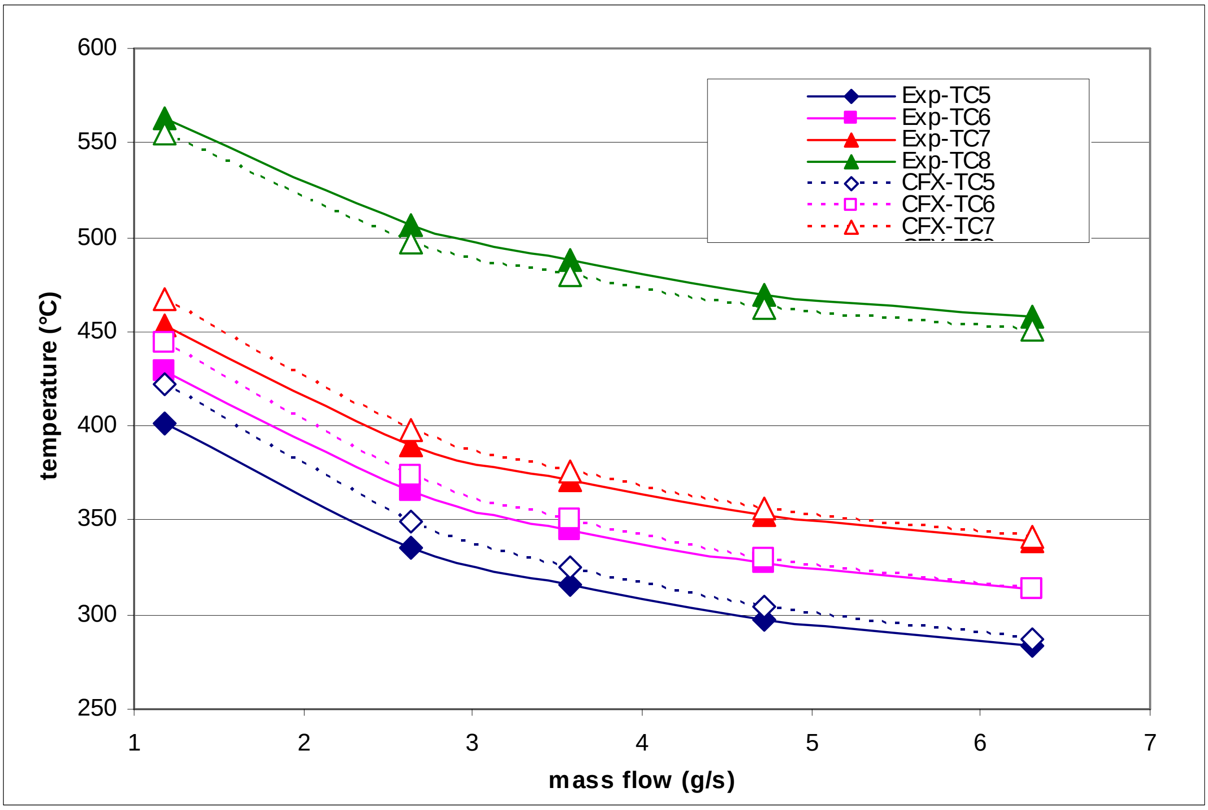

Fig. 34 b) TC 5 to TC 8

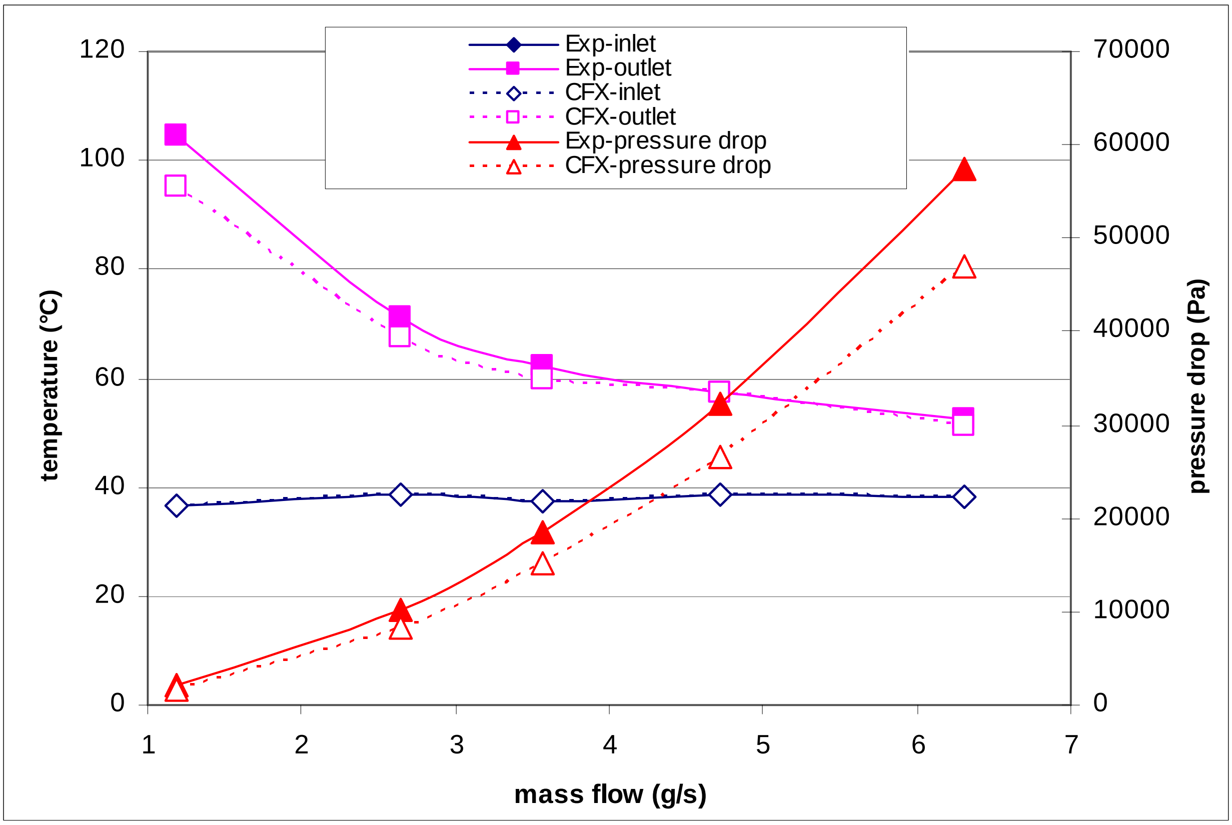

Fig. 34 c) Inlet, outlet and pressure loss

Fig. 34: Comparison of measured and simulated temperatures and pressure losses (mesh V6mod, second test series) in the different parts of the mock-up for the case of 455 W.

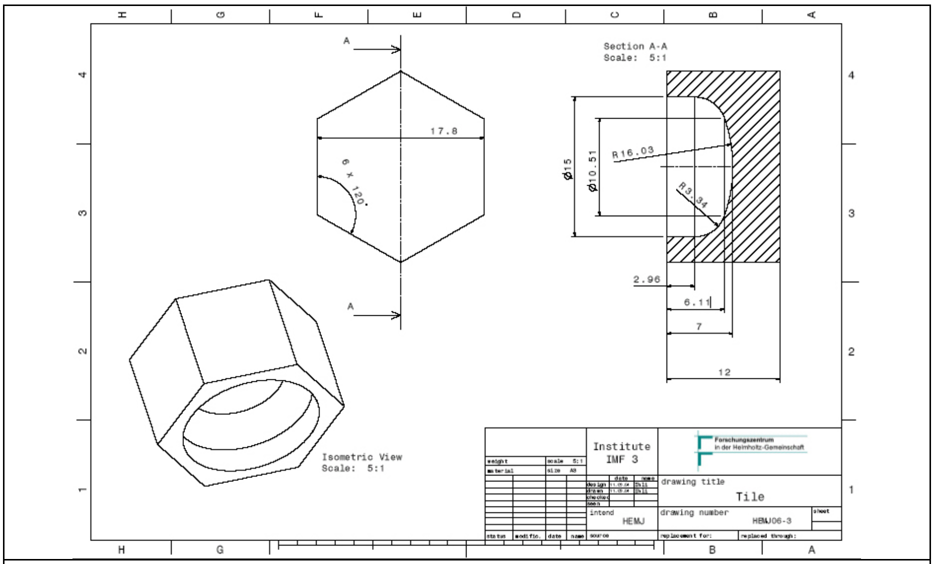

Tile

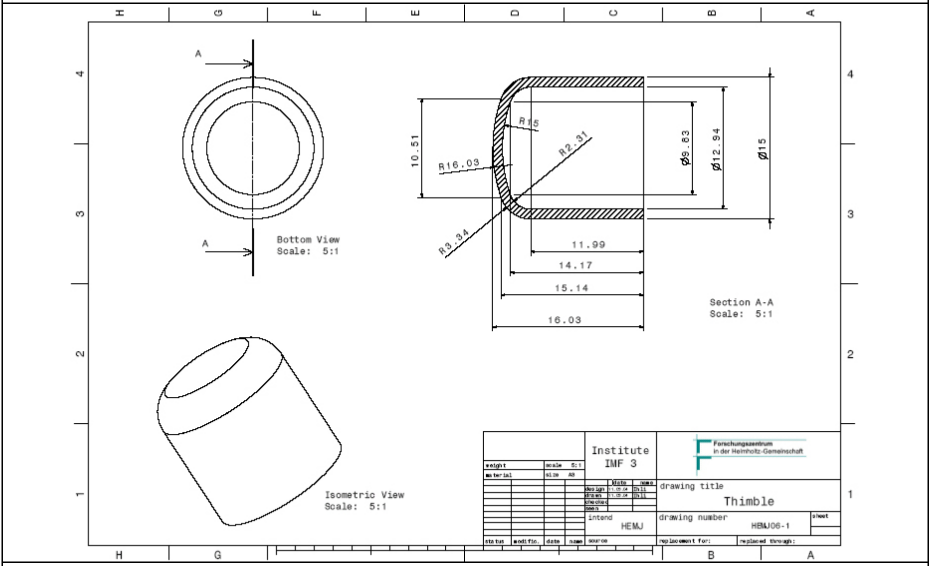

Thimble

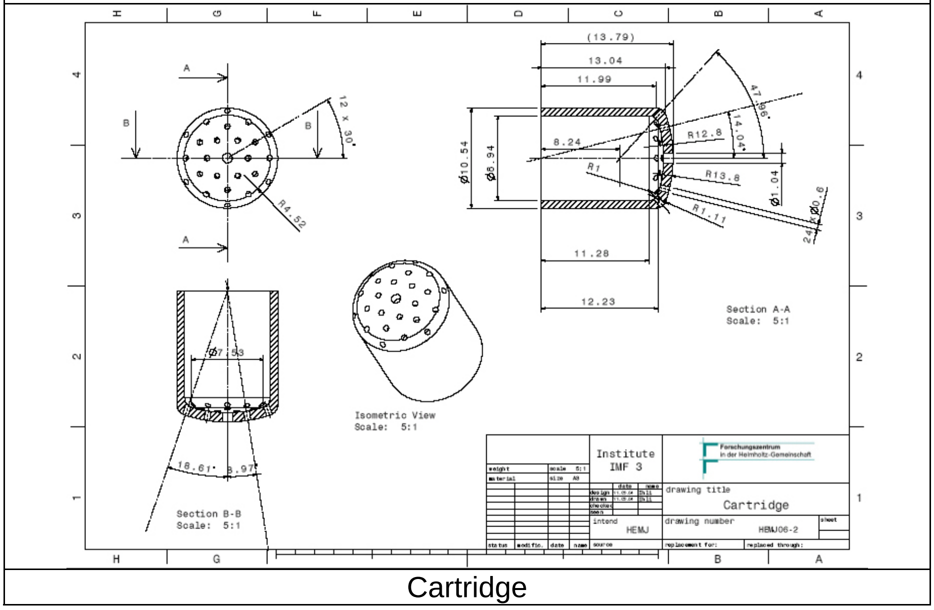

Cartridge

Fig. 35: Technical drawings of tile, thimble, and cartridge for J1a.

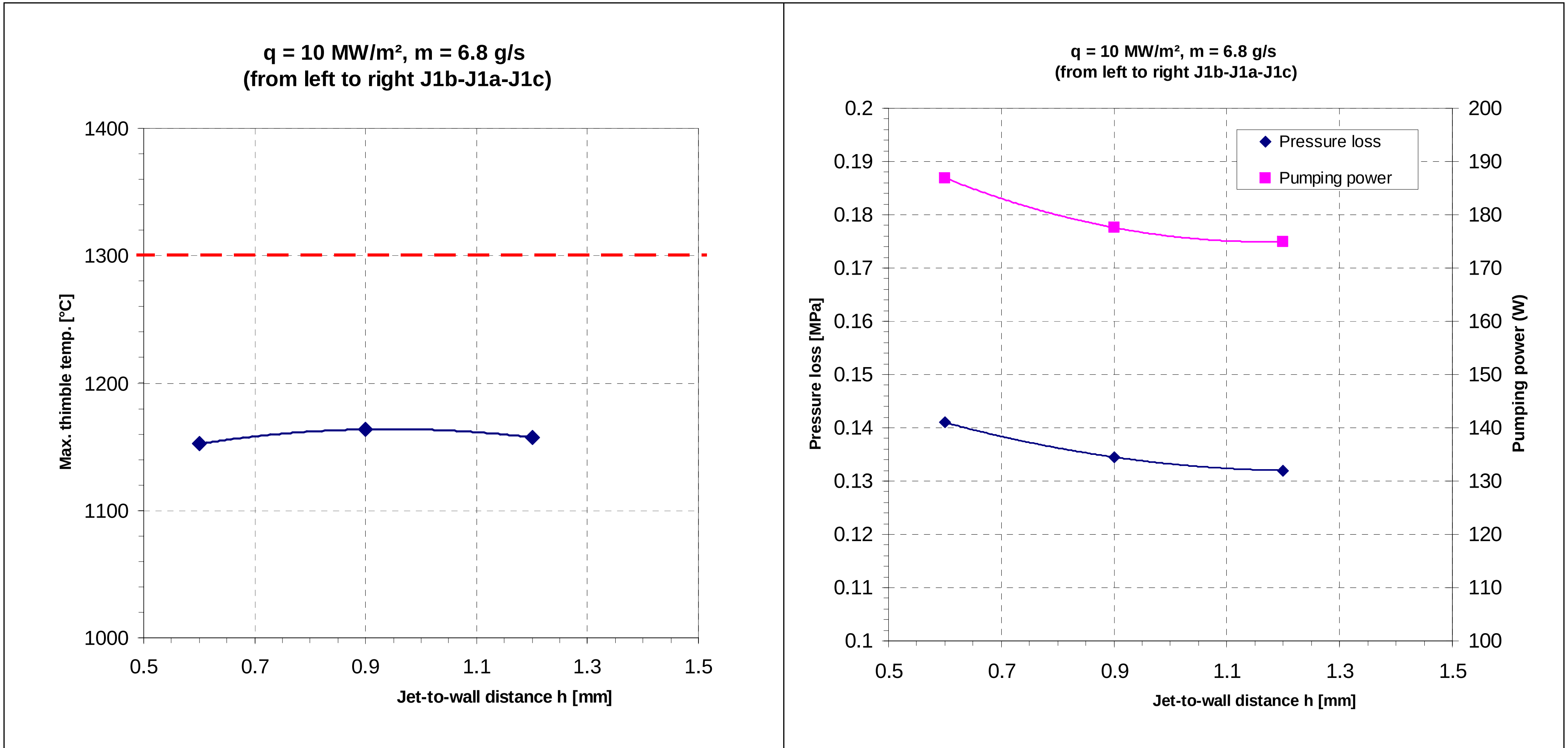

a) Thimble temperature

b) Pressure loss

Fig. 36: Results for jet-to-wall distance h.

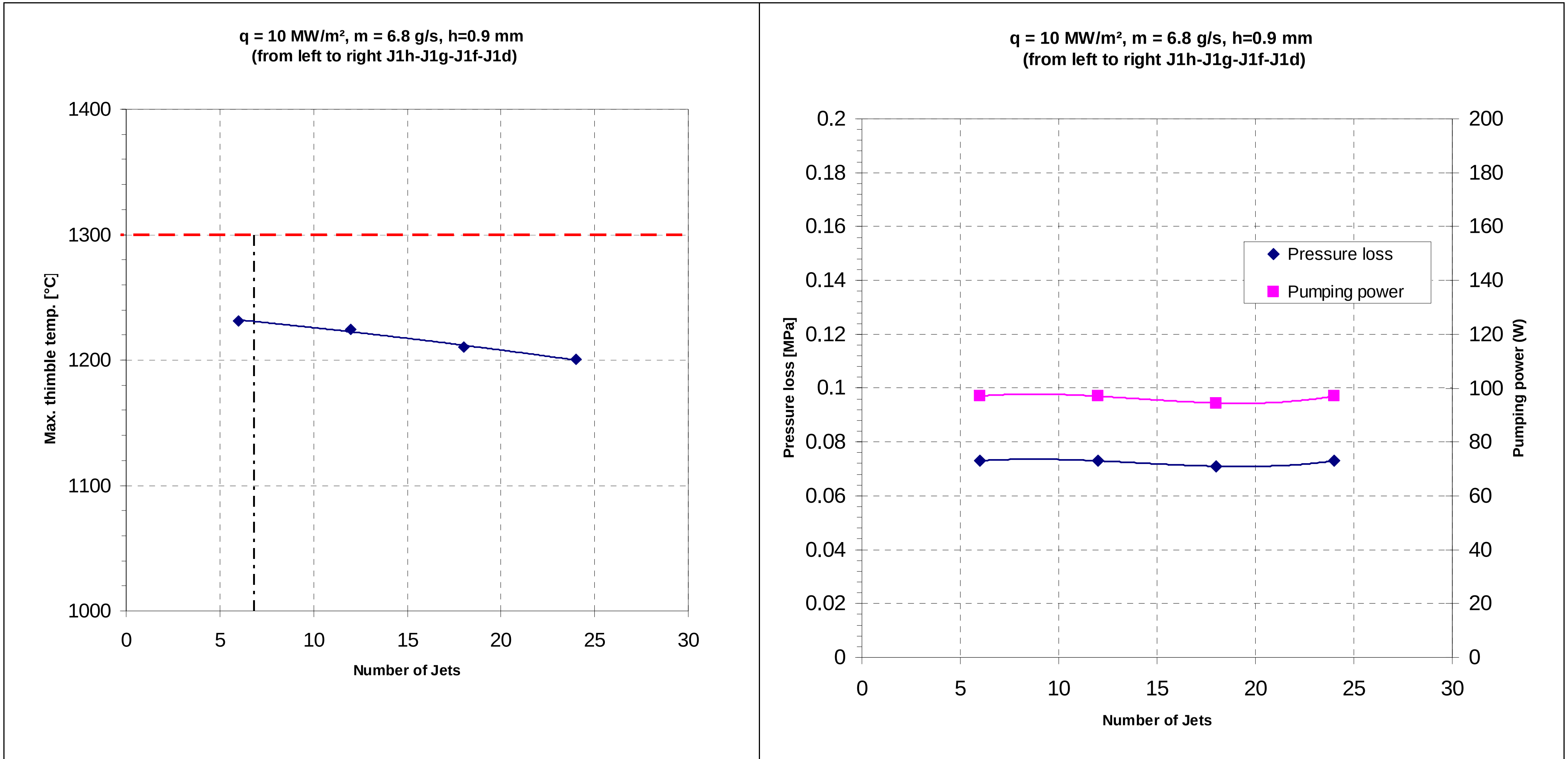

a) Thimble temperature

b) Pressure loss

Fig. 37: Results for the number of jets.

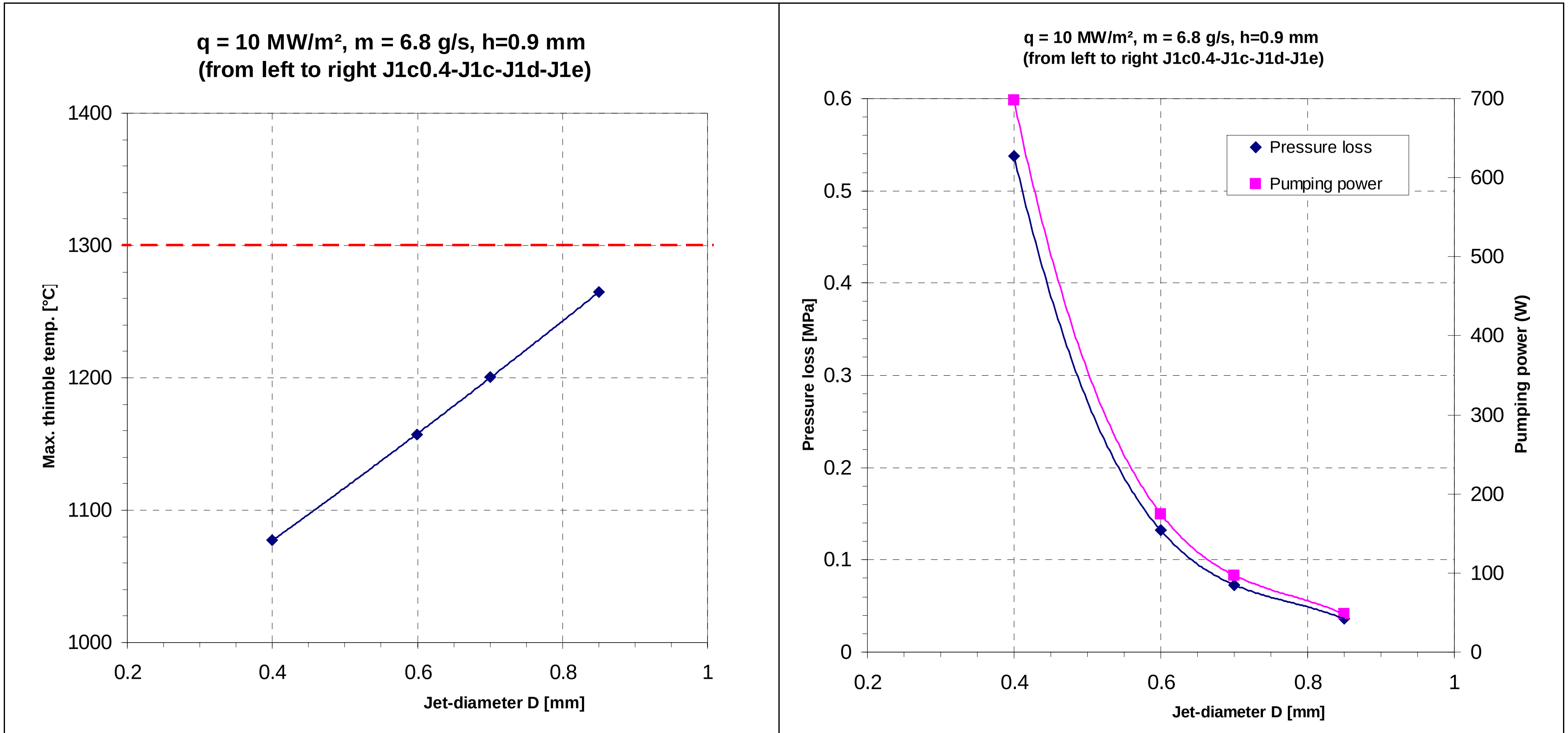

a) Thimble temperature

b) Pressure loss

Fig. 38: Results for the jet diameter D.

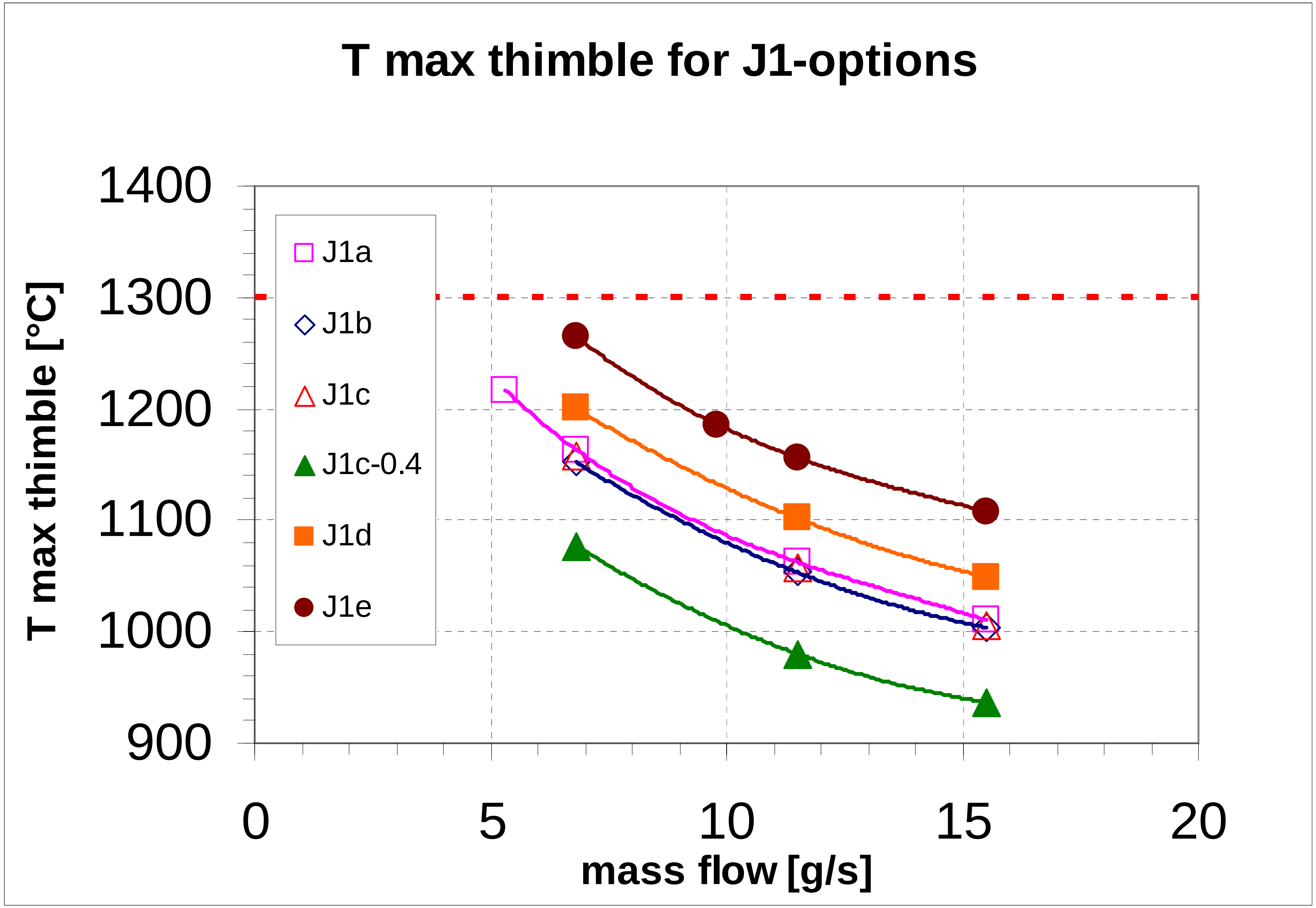

Fig. 39 a: Max. thimble temperature over mass flow for all design variants J1x.

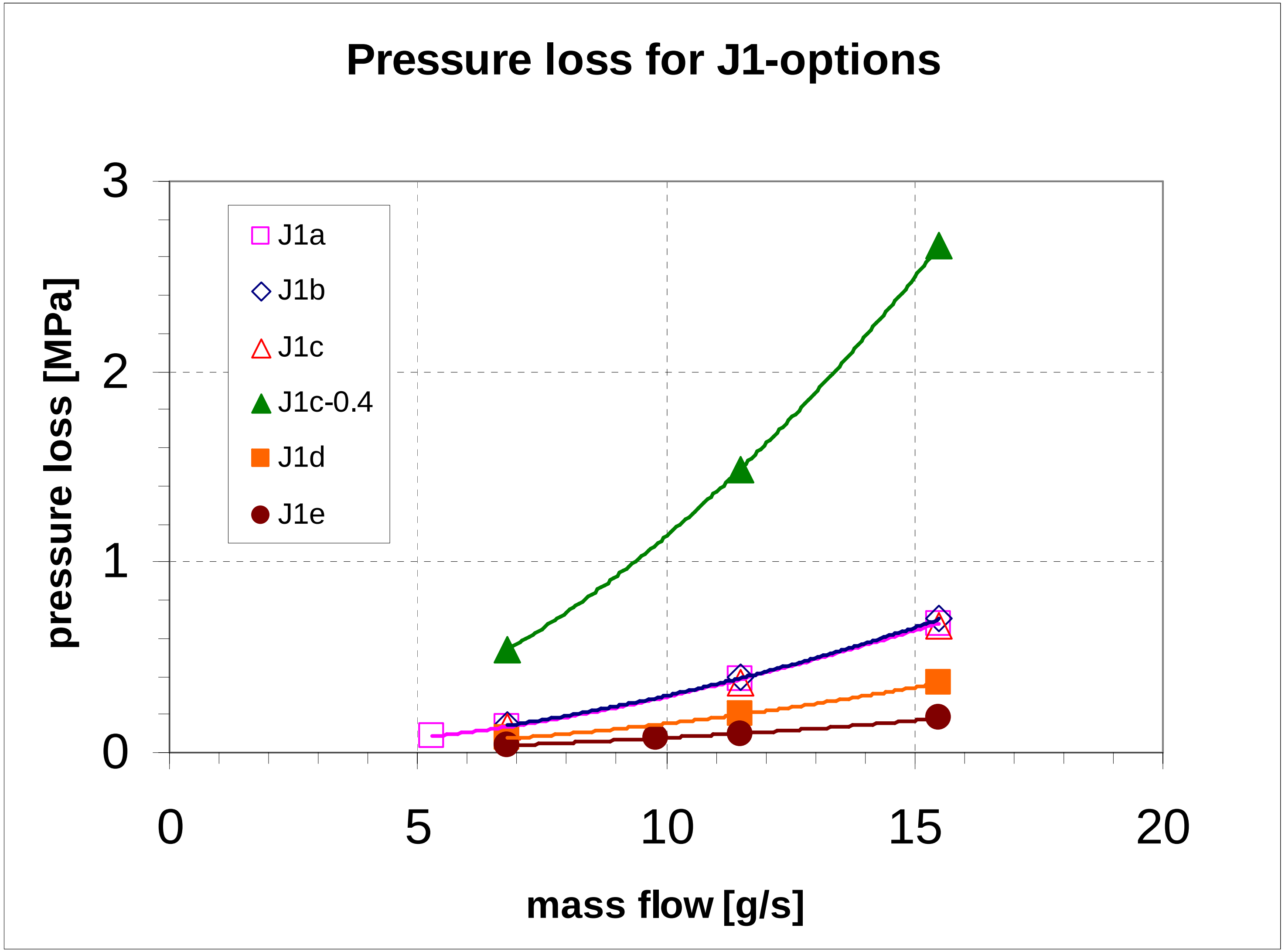

Fig. 39 b: Max. pressure loss over mass flow for all design variants J1x.